DOKUZ EYLÜL UNIVERSITY
GRADUATE SCHOOL OF NATURAL AND APPLIED SCIENCES

HYBRID NUMERICAL TECHNIQUES WITH NEW BEAM-TYPE GREEN'S FUNCTIONS FOR TWO-DIMENSIONAL ELECTROMAGNETIC SCATTERING

by
Deniz KUTLUAY

July, 2020
İZMİR

HYBRID NUMERICAL TECHNIQUES WITH NEW BEAM-TYPE GREEN'S FUNCTIONS FOR TWO-DIMENSIONAL ELECTROMAGNETIC SCATTERING

A Thesis Submitted to the
Graduate School of Natural and Applied Sciences of Dokuz Eylül University
In Partial Fulfillment of the Requirements for the Degree of Doctor of Philosophy in Electrical and Electronics Engineering Program

by
Deniz KUTLUAY

July, 2020
İZMİR

Ph.D. THESIS EXAMINATION RESULT FORM

We have read the thesis entitled "**HYBRID NUMERICAL TECHNIQUES WITH NEW BEAM-TYPE GREEN'S FUNCTIONS FOR TWO-DIMENSIONAL ELECTROMAGNETIC SCATTERING**" completed by **DENİZ KUTLUAY** under supervision of **PROF.DR. TANER OĞUZER** and we certify that in our opinion it is fully adequate, in scope and in quality, as a thesis for the degree of Doctor of Philosophy.

Prof. Dr. Taner OĞUZER

Supervisor

Prof. Dr. Yeşim ZORAL

Thesis Committee Member

Assoc. Prof. Dr. Sedef KARAKILIÇ

Thesis Committee Member

Prof. Dr. Mustafa SEÇMEN

Examining Committee Member

Assoc. Prof. Dr. Merih PALANDÖKEN

Examining Committee Member

Prof. Dr. Özgür ÖZÇELİK

Director

Graduate School of Natural and Applied Sciences

ACKNOWLEDGEMENTS

First and foremost, I would like to express my sincere thankfulness to my supervisor Prof. Dr. Taner OĞUZER, for the continuous support of my Ph.D. study and related research. He shared his valuable time every week, and his assistance has been essential for me during the research and writing of this thesis. I am grateful to him for his motivation, invaluable guidance, and extensive knowledge.

I would like to thank Prof. Dr. Yeşim ZORAL for guiding the research, sharing her valuable comments, and advising me to apply BAP Project. I would like to thank Assoc. Prof. Dr. Sedef KARAKILIÇ for supporting the research and helpful reviews. I would like to thank Prof. Dr. Mustafa SEÇMEN and Assoc. Prof. Dr. Merih PALANDÖKEN for being members of the thesis committee.

This dissertation was supported by Dokuz Eylül University, Research Project BAP (Coordinators of Scientific Research Projects) under grant number 2018.KB.FEN.006., İzmir TURKEY.

There is one person whom I wish could still be with me today. This study is dedicated to my late mother, who is an essential reason for my educational success.

Deniz KUTLUAY

HYBRID NUMERICAL TECHNIQUES WITH NEW BEAM-TYPE GREEN'S FUNCTIONS FOR TWO-DIMENSIONAL ELECTROMAGNETIC SCATTERING

ABSTRACT

In this study, an alternative approach is introduced to the numerical solution of two-dimension (2D) electromagnetic (EM) scattering problems by two hybrid numerical techniques combining with the method of moments (MoM). Two new hybrid techniques based on beam pattern function have been proved to solve the electric field integral equation (EFIE) by combining them with MoM in both polarizations.

The first proposed technique is named *MoM procedure with complex source point (CSP) type Green's function*. The conversion from an isotropic line source radiation to a directive beam radiation has been demonstrated with an expression of CSP type Green's function by using the CSP technique. In this first method, the real source position vector is replaced by a complex quantity, then Green's function generates a CSP beam. In this way, the interactions between far zone elements in the impedance matrix have become negligible, except the basis functions near to the edges of the scatterer. Consequently, the overall running time has been substantially reduced.

The second proposed method is named *MoM Procedure with modified Green's function by using a generalized pencil of beam function (GPOF) method*. In the second method, the main matrix is strongly localized, like in the first method. However, as the beam width is much narrower compared to the first method, the radiation of this Green's function produces the higher sparsity in the main matrix. In the circumstances, the memory storage and the overall running time become much smaller so that the larger sizes can be modeled with the shorter computational times.

Keywords: Electromagnetic scattering, computational electromagnetics, hybrid methods, radar cross section, complex source point, a generalized pencil of beam function.

İKİ BOYUTLU ELEKTROMANYETİK SAÇILMA İÇİN YENİ IŞIN TİPİ GREEN FONKSİYONLARI İLE HİBRİT NUMERİK TEKNİKLER

ÖZ

Bu çalışmada, momentler yöntemi (MoM) ile birleştirilen iki sayısal hibrit tekniği kullanılarak, iki boyutlu (2D) elektromanyetik saçılma problemlerinin sayısal çözümüne ilişkin alternatif bir yaklaşım sunulmuştur. Işın biçimli fonksiyon tabanlı iki yeni hibrit tekniğin MoM ile birleştirilerek, her iki polarizasyonda elektrik alan integral denklemini (EFIE) çözdüğü gösterilmiştir.

Önerilen ilk tekniğe, *kompleks kaynak noktası (CSP) tipinde Green fonksiyonu ile MoM prosedürü* denir. İzotropik bir çizgisel kaynak radyasyonundan CSP tipi Green fonksiyonu ifadesiyle yönlü bir ışına dönüşüm CSP tekniği kullanılarak gösterilmiştir. Bu ilk yöntemde, gerçel kaynaklı konum vektörü karmaşık kaynaklı bir değer ile değiştirilir, ardından Green fonksiyonu bir CSP ışını oluşturur. Bu şekilde, empedans matrisindeki uzak bölge elemanları arasındaki etkileşimler, saçıcının kenarlarına yakın temel fonksiyonlar hariç olmak üzere ihmal edilebilir hale gelmiştir. Sonuç olarak, toplam çalışma süresi önemli ölçüde azaltılmıştır.

Önerilen ikinci yönteme, *genelleştirilmiş bir ışın demeti fonksiyonu (GPOF) yöntemi kullanılarak değiştirilmiş Green fonksiyonu ile MoM prosedürü* adı verilir. İkinci yöntemde, ana matris, birinci yöntemde olduğu gibi güçlü bir şekilde lokalizedir. Bununla birlikte, ışın genişliği ilk yönteme kıyasla çok daha dar olduğundan, bu Green fonksiyonunun radyasyonu ana matriste daha yüksek bir seyreklik meydana getirir. Bu durumda bellek depolama alanı ve toplam çalışma süresi çok daha küçük hale gelir, böylece daha büyük boyutlar daha kısa hesaplama süreleriyle modellenebilir.

Anahtar kelimeler: Elektromanyetik saçılım, hesaplamalı elektromanyetik, hibrit metotlar, radar kesit alanı, kompleks kaynak noktası, genelleştirilmiş bir ışın demeti fonksiyonu.

CONTENTS

Page

LIST OF FIGURES

Page

LIST OF TABLES

Page

CHAPTER ONE
INTRODUCTION

1.1 General Information About Numerical Solutions of Electromagnetic Scattering Problems

Scattering is one of the most important problems of electromagnetics, and it is considered a free-space boundary value problem of the Helmholtz equation. Some numerical techniques have been applied for analyzing scattering in the EM problems, which depend on the geometry and frequency. The numerical modeling of the EM wave scattering is becoming increasingly more important research area due to further developments in communication systems. Historically, a numerical MoM was first developed and applied to scattering problems as a simple numerical tool (Harrington, 1968). Afterward, various other numerical techniques were improved and implemented to the modeling of scattering objects.

Some of these techniques are Physical Optics (PO), Physical Theory of Diffraction (PTD), Geometrical Theory of Diffraction (GTD), or its uniform version UTD. These techniques can be utilized in high-frequency approximations and used for applications whose wavelength is much shorter than the object. As in the Moment Method, some numerical methods such as Finite Difference Time Domain Method (FDTD) and Finite Element Methods (FEM) are also limited by computer performance, especially when the scatterer size is large comparing to the wavelength. Depending on the geometry or frequency of the problems, these methods are sometimes not suitable for producing results of accurate enough. Moreover, applying these methods may trouble the solution part in terms of the computational cost (memory and CPU time), especially in the high-frequency regime. Therefore the presentation of the hybrid techniques needs to be suggested for the problems that can not be solved by a single numerical method.

There are many studies for the hybrid formulations that combine the MoM technique with another approximation (Thiele & Mittra, 1992). MoM-GTD and MoM-UTD are ray hybrid techniques with some advantages in a wide variety of practical problems for which the appropriate diffraction coefficients are known (Thiele & Newhouse, 1975). These are referred to as field-based hybrid techniques since they utilize electric fields in their formulation. However, they are limited to the physics of the problem in which diffraction or reflection occurs. Another hybrid method, known as the MoM-PO hybrid technique, is a current-based formulation. It is an excellent procedure to handle the problem of electrically large objects (Jakobus & Landstorfer, 1995; Jakobus & Meyer, 1996). MoM-PO hybrid technique and its improved version are more elegant for practical problems than MoM-GTD and MoM-UTD. They are applicable to 2D and 3D scattering bodies that the PO-current is a linear superposition of basis functions. It has also been developed as an iterative form and implemented to large-scale structures by avoiding calculating the PO contribution in matrix form (Liu & Wang, 2012). The PO contribution to the MoM impedance matrix was calculated by completing an iterative way to enhance the conventional MoM-PO method.

1.2 Hybrid Methods For Fast Solution

MoM has been combined iteratively with a solver called the Fast Multi Pole (FMP) technique, and it is frequently applied to many complicated scattering objects (Coifman et al., 1993). A fast algorithm based on the grouping of the basis functions in a particular order has been utilized to compute the interactions of the far zone elements in this FMP-MoM technique. In (Belenguer et al., 2005), the remarkable result was achieved for the operation count and memory storage, such as O($N^{1.5}$), while it is O(N^2) in the conventional MoM.

Different methods can be adapted together as hybrid techniques in the numerical solution of EM scattering. The impedance matrix localization (IML) technique has been introduced (Canning, 1990) for this purpose, which uses a directional basis and testing functions to localize them by producing a directivity. This modification transforms the original dense matrix into a sparse form by selecting individual basis and testing functions. In this way, some elements have limited interactions, and the other matrix elements may be approximated by zero. After this localization, the memory requirements and CPU computation times are reduced. However, it should be careful when selecting basis and testing functions due to numerical stability such as condition number of the main matrix. Although sparse matrix form can be obtained using some functions, matrix condition number can be higher than the original form. Then, using these functions leads the system to the ill-conditioned situation and incorrect results. Briefly, selecting the testing and basis functions has a critical role in the solution part of this technique. The number of the total required elements in the main matrix is reduced to 100xN by the IML technique. Furthermore, using the IML technique with the FMP method has demonstrated a favorable advantage in the iterative solution of MoM equations (Han et al., 1998). However, IML transformation works only for 2D geometries, and it appears not to eligible for analyzing 3D scattering problems.

Since the special basis functions in (Canning, 1990) can not effectively express a rapid phase variation, the locality has been proposed by introducing different local-domain basis functions in the high-frequency analysis (Shijo et al., 2005; Ando et al., 2011). The 2D strip and corner reflector geometries illuminated by electric line current have been viewed using these new local-domain basis functions. Using novel local-domain basis functions causes the reduction of mutual coupling between the elements in the impedance matrix. The off-diagonal elements become small and negligible by introducing the Fresnel zone number, and the impedance matrix reduces to the sparse band matrix. Consequently, they reduced the maximum number of the unknown from $O(N^2)$ to $O(N)$ for these geometries. In this PO-MoM hybrid method, the Fresnel zone number is utilized for the switching criteria between the PO and the MoM. For specific positions of source and observer, it is defined as a relation with the mutual coupling between two elements. It states the degree of sparsity of the impedance matrix.

By using some expansions, the fields can be expanded to terms to take some advantages in the solution of EM radiation problems. Gaussian beams are one of the suitable solution examples for these expansions in which the fields can be considered as a sum of Gaussian functions. An expansion procedure for EM wave has been expressed in terms of Gaussian beams and studied to find out current radiation patterns by adopting the Gabor series (Chabory & Bolioli, 2006; Melamed, 2009). However, Gaussian beams satisfy Maxwell's equations only in the paraxial region.

The Complex Source Point (CSP) concept has been presented as a new approach for generation Gaussian beams (Felsen, 1976). The CSP technique has provided simplicity into the modeling of the scattering problems. It can be easily combined with other methods, and CSP beams satisfy Maxwell's equations everywhere in space. Each CSP beam in the expansion can be thought of as a narrow beam, so its radiation is considered in this restricted region. Consequently, the fields are localized due to the CSP beams since they have some particular propagation directions. This approach seems very useful because only beams propagating through the observation directions contribute to the radiated field. However, it has some difficulties, such as the determination of coefficients in the expansion, and they need to be validated for some EM scattering conditions. In (Suedan & Jull, 1991) and (Oguzer et al., 1995), the CSP beam-like incident field has been employed in modeling a 2-D parabolic reflector antenna with a combination of the Physical Optics and Riemann-Hilbert Problem methods, respectively. A similar method has been used in the modeling of 2-D dielectric lenses (Boriskin & Nosich, 2002; Boriskin et al., 2009) and layered dielectric slab scattering (Tsitsas et al., 2014). In (Bulygin et al., 2013), the 3-D beam feeding a PEC paraboloid antenna has been taken as a Complex Huygens Source.

Combining the CSP approach with MoM has also been realized as a hybrid method of fictitious currents. The real and CSP dipoles are both located inside the object's boundary, and their fields on the surface of the object are tested (Erez & Leviatan, 1994). Nevertheless, this creates a small matrix with a high condition number. Alternatively, it has been used as another expansion for fields on the scatterer boundary, which is a series of beams generated by complex multipoles (Boag & Mittra, 1994a). They can be linked to simulate scattering, which also results in a small matrix, but in this case, it has a more stable form. The scattered field is described in terms of a series of beams by realizing an analytic continuation of the multipole fields to complex source coordinates. They utilized the Gabor series properties to develop the locations of multipole sources, and they exhibited that the method is valid for analyzing 3D scattering problems with no edges (Boag & Mittra, 1994b). They have introduced the relation between these multipole source expansion and Gabor expansion. They also demonstrated that the condition number is acceptable, while the sparsity of the main matrix turns into a sparse banded form. This new method has proved the advantages of combining the IML and multiple multipole (MML) methods. It has been analyzed for 2D and 3D arbitrarily shaped large smooth bodies. In the presence of edges, the scattering from a 2D closed conducting body has been examined using a combination of the multipole beam method with the MoM procedure (Boag et al., 1994). The number of unknowns has been reduced, but the selection of multipole source points is crucial.

In a different hybrid method (Tap, 2007; Tap et al., 2011, 2014), the standard MoM has been combined with the CSP expansion technique to simulate scattering from the electrically large objects. The first stage in this method is that the radiation of the basis functions is expanded into a series of CSP beams defined on a sphere surrounding them. As shown in Figure 1.1, only a small portion of the beams radiating from the source must be taken into consideration for the determination of the scattered field at the observation point P. The rest of the beams do not contribute significantly, and they can be neglected in the computation. At the second stage, the basis functions are sort out for grouping with the appropriate group size; then, calculations are done according to group separations. The near field interactions in the same groups are computed with multiple integrals as in the standard MoM procedure. However, for any pair of well-separated groups, the interactions can be performed using the analytical representation of the related beams. Therefore, the impedance matrix can be computed in this way; furthermore, after the treatment of a particular factorization procedure, the main operator matrix converts to a sparse form. Consequently, the matrix-vector multiplication in iterative MoM becomes more efficient, so the memory and the operation count can be reduced to O($N^{1.5}$) compared to O(N^2) of conventional MoM methods. This conversion allows efficient modeling of 3D scattering from electrically large complicated objects, and it can also be applied to 2D geometry with the named memory and operation count.

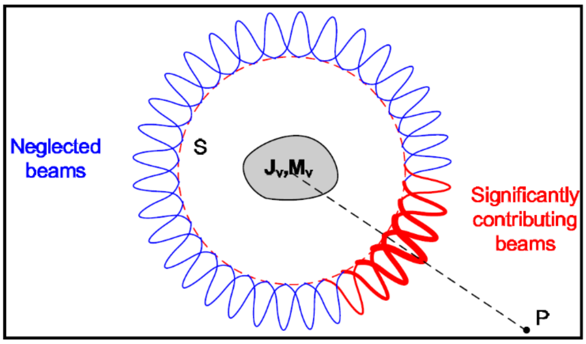

Figure 1.1 Only a small portion of the beams remain significant at P (Tap, 2007)

1.3 The Presentation of Two New Hybrid Techniques

1.3.1 MoM Procedure with CSP Type Green's Function

In this thesis, the first hybrid technique presented as a beam type localization is defined as *the MoM Procedure with CSP Type Green's Function*. Instead of using the CSP expansion of a source field, a modified Green's function, which exploits the CSP technique, is combined with MoM. By adding the imaginary part to the source coordinate, the radiation of the isotropic cylindrical wave from a conventional line current source can be turned into a unidirectional CSP beam field. In this technique, the source position of the Green's function is converted to a complex number, which can be used to adjust the beam direction and beamwidth. Then, this CSP type Green's function can be used in the radiation integral and the integral equation obtained from the boundary condition (BC). This conversion shapes the radiation of the basis function into a unidirectional beam-like form with the beam aperture on the surface of the scatterer, directed outward from the object. Under these circumstances, most interactions between the elements on the scatterer surface become negligible due to the nature of the beam; thus, they can be neglected. Only small regions near the edges should be left intact to save the edge effects appearing in line with the wave physics of the problem.

Then, the impedance matrix of MoM can be generated as a sparse form. This procedure is in agreement with all conditions of the EM uniqueness theorem.

Therefore, it is anticipated that the correct radiated field is produced in the near and far zones, even though the radiation integral and the surface current density seem to counter-intuitive. The proposed technique is an attractive alternative for 2D scattering problems, especially for electrically large geometries.

This procedure has been briefly described in (Kutluay & Oğuzer, 2017) for a single flat PEC strip in the E-polarisation case; afterward, a more detailed demonstration has been presented for electrically large PEC strip and 2D closed-contour PEC objects in both polarizations (Kutluay & Oğuzer, 2019). The square and triangle cylinder geometries with a large size have been introduced with an outstanding gain in solution time and very small REs such as less than %0.1 compared to the MoM. In this thesis, structures with a considerable large size for square and triangle cylinder geometries have been explored by using the first new hybrid technique. Since the memory and the operation count are reduced to about O(300xN) for polygonal cross-section cylinders compared to O(N^2) in conventional MoM, exceptional time gains have been obtained for both polarizations such as over 30 times less compared to the MoM solution.

Additional to 2D closed-contour PEC objects, it has been performed for open body structure like a corner reflector geometry that is widely used in the scattering problems, and it has been developed over the years (Rudge & Adatia, 1978; Menzel et al., 2002; Rahmat-Samii & Haupt, 2015). In some particular reflector angles at which the unidirectional CSP beam fields of Green's function do not affect each other, favorable results have been achieved. Nonetheless, in the opposite case, the interactions of CSP beam fields must be taken into account in the solution part. The analysis of this problem has been left for further study in the future with the field interactions by using some iterative techniques.

This approach of computing the main matrix of MoM can be applied to the 3D configurations in a simple form, like a square plate, cube, where the complex exponential nature of the 3D Green's function provides a similar property. 3D Green's function decays quickly to a very small number at a certain distance from CSP location. However, in the 3D case, the number of basis functions near the edges would be larger than in the 2D case. It can be expected an increase in memory storage and overall computation time compared to the 2D case, but this requires further investigation.

Although the condition number of the main impedance matrix is at a high level around 10^6, outcomes in comparison with MoM are in excellent agreement with each other by using optimum iterative sparse solvers in MATLAB. Nevertheless, in this direction, the second hybrid technique is presented with a lower condition number.

1.3.2 MoM Procedure with Modified Green's Function by Using Generalized Pencil of Function Method

For a newly modified Green's function, the GPOF method is combined with MoM as a second hybrid technique in this thesis. A surface field distribution with finite width is introduced to the new formulation, and it is used in the definition of a new Green's function. For obtaining this field distribution, a pulse function is used in convolution operation that is convoluted with itself. At the end of the first convolution process, the triangular function obtained is convoluted with itself in the second process. Resultant of this stage, a smooth signal is achieved by utilizing the convolution property of Fourier Transform. This spectral domain function attained is expressed in a finite series of exponents by using the GPOF method. The coefficients in this series are found by employing the GPOF technique. Eventually, this function is associated with the Hankel function linked by Sommerfeld identity and obtained a new Green's function. This modified Green's function has a beam aperture on the surface, and its beam width can be reduced to a few basis function levels. This technique can also be considered a beam-type localization, and this kind of localized Green's function can again be used in the procedure defined as in (Kutluay & Oğuzer, 2019). This more localized Green's function is obtained by using the GPOF method and combined with MoM. Also, it satisfies all the uniqueness conditions, so it is an approximation of a unique field distribution. This modification of Green's function yields more sparsity in the main matrix comparing with the previous method. The memory storage and the overall running times become smaller so that the larger sizes can be modeled with the shorter computational times. This implementation has been performed for EM plane wave scattering from the electrically large PEC strip (Oğuzer & Kutluay, 2019).

The proposed technique is another attractive solution for 2D scattering problems. In contrast to the previous method, this proposed localized Green's function provides us with a reasonable condition number around 10^4 that makes the approach a little more attractive. Since a narrower beam field is acquired comparing the previous technique, basis function levels have much less wideness. Hence, interactions in the far zone elements with these basis functions are decreased significantly. This decrease presents a chance to analyze larger geometries relatively comparing to the previous method. However, the proposed technique has been performed for 2D electrically large PEC objects with the same size in the previous method to comprehend the difference. The memory storage has been discovered about O(50N) for 2D PEC polygon cross-section cylinder geometries in both polarizations. Therefore, extraordinary time gains have been obtained, such as over 200 times less compared to the MoM solution. Consequently, the second proposed technique is an effective alternative approach for 2D objects.

Similar to the previous method, it can be applied to the simpler 3D configurations in the future study since the modification is implemented in Green's Function and does not depend on spatial parameters.

1.4 Materials and Methods

The software code and scrip files have been composed in MATLAB ver.2019(b), which our department supplied. The simulations have been computed using available laptop PC with the Intel i7 processor of the 7th generation and 32 GB RAM working on the Windows 10 platform.

In the first step, the standard MoM procedure with the Galerkin method has been employed for the problems. In MoM solutions, problems for all geometries have been solved by Galerkin MoM using pulse-type basis functions in E-pol, and triangular type basis functions in H-pol. Then, the presented approaches have been applied for the problems to compare with the MoM.

CHAPTER TWO
METHOD OF MOMENTS

MoM is a well-known and valid numerical solution method in EM scattering problems. R. F. Harrington was the first to use the method of moments in electromagnetics (Harrington, 1968). MoM is a discretization method and usually applied to integral equations in EM problems. EM radiation, scattering, and wave propagation problems can be analyzed with modest computing memory. It solves the integral form of Maxwell's equations while FEM or FDTD method is used for their differential forms. Let us consider the inhomogeneous equation:

$$L\{f\} = g \tag{2.1}$$

where L is a linear operator, and it may be in differential, integral, or integro-differential form, g is known (source or excitation), and f is the unknown function to be determined (fields or response). The deterministic term of the f function means that the solution is unique, and there is only one f that is associated with a given g. The functional equation is reduced to a suitable matrix equation by using basic mathematical techniques. Then, the solution is found by matrix inversion, and the equation of physical problem is solved.

Three steps are the core of the method of moments. The first step is meshing the structure and choosing the intervals over the unknown function f. Second step is to expand the unknown function f into basis functions. The last step has involved the observation and described dot-multiplying both sides of the equation by a weighting function (or test function). A suitable inner product that is symmetric has to be required for the problem to identify the operator L, its domain, e.g., Ω; the functions f on which it operates, and its range; the functions g resulting from the operation.

$$\langle g_1, g_2 \rangle = \int_{r\in\Omega} g_1(r) g_2(r) d\Omega \tag{2.2}$$

2.1 Procedure of MoM

Consider a domain Ω: $x \in [a,b]$ and a linear integral operator L, and an example of equation (2.1):

$$\int_a^b f(x')K(x,x')dx' = g(x) \tag{2.3}$$

Unknown and known functions must be in the domain of the operator and are both defined on the domain Ω. At the first step, for meshing the structure, let us explain the maximum step number as N. At the second step, the unknown function f is expanded into a series with a summation of known functions multiplied by unknown constants.

$$f(x) = \sum_{n=1}^{N} \alpha_n f_n(x) \tag{2.4}$$

where α_n are constants, the set of f_n is called basis functions, or expansion functions, and they must be linearly independent. They should also be selected to satisfy the boundary and edge conditions of the problem to make convergence more relaxed. For an exact solution, it is obvious that the summation should be taken to infinite but has to be finite in practice. Since L is a linear operator and can be interchanged with the summation, equation (2.1) becomes

$$\sum_{n=1}^{N} \alpha_n L\{f_n(x)\} \cong g(x) \tag{2.5}$$

At the last step, a set of weighting functions, or testing functions are defined in the range of L as $\{w_1, w_2, \ldots w_N\}$. To find α_n, Equation (2.5) for both sides are tested with the weighting functions. For only one step testing procedure, each inner product gives one equation in N unknowns:

$$\left\langle w_1, \sum_{n=1}^{N} \alpha_n L\{f_n\} \right\rangle = \langle w_1, g \rangle \tag{2.6}$$

Thanks to symmetric inner product property, the summation of constants can be moved outside of the inner product.

$$\sum_{n=1}^{N} \alpha_n \langle w_1, L\{f_n\} \rangle = \langle w_1, g \rangle \tag{2.7}$$

N testing functions are used to fix the unknown number to the equation number, and it is obtained the final matrix equation with N equations in N unknowns:

$$
\begin{bmatrix}
\langle w_1, L\{f_1\}\rangle & \langle w_1, L\{f_2\}\rangle & \cdots & \cdots & \langle w_1, L\{f_N\}\rangle \\
\langle w_2, L\{f_1\}\rangle & \langle w_2, L\{f_2\}\rangle & & & \vdots \\
\vdots & & \ddots & & \\
\vdots & & & \ddots & \vdots \\
\langle w_N, L\{f_1\}\rangle & & & & \langle w_N, L\{f_N\}\rangle
\end{bmatrix}
\begin{bmatrix}
\alpha_1 \\ \alpha_2 \\ \vdots \\ \vdots \\ \alpha_N
\end{bmatrix}
=
\begin{bmatrix}
\langle w_1, g\rangle \\ \langle w_2, g\rangle \\ \vdots \\ \vdots \\ \langle w_N, g\rangle
\end{bmatrix}
\qquad (2.8)
$$

Finally, a matrix equation is obtained, which approximates the given problem. The system can now be written in matrix form as:

$$[Z_{mn}][\alpha_n] = [g_m] \qquad m=1,2,\ldots.N \qquad (2.9)$$

Z_{mn} is called the main impedance matrix or main matrix, and g_m is called excitation vector relating to the source known. The indice *m* corresponds to an observation point, unprimed coordinates, while the indice *n* corresponds to a source point, primed coordinates. The physical meaning of indices is that the element (m,n) represents the effect of cell *n* on cell *m,* and the element (m,m) represents the self-term. If the matrix Z_{mn} is not singular, the unknowns α_n are simply given by:

$$[\alpha_n] = [Z_{mn}]^{-1}[g_m] \qquad (2.10)$$

and the original function *f* can be reproduced with the known constants α_n using the equation (2.4).

In MoM simulation of EM scattering problems, the unknowns of the problem are the currents or fields on the surface of a structure. Surface or volume currents of the scatterer are the unknown physical currents and must be discretized in terms of elementary currents. Such elementary currents are described as basis functions with initially unknown amplitudes. These amplitudes are the unknown constants α_n, and the currents are unknown function *f(x)* in (2.4). Through the MoM solution, these unknown amplitudes are found and shaped the currents. Once the total currents are known, the fields can be calculated everywhere in the structure.

In the solution part, the matrix inversion methods are solved based on numerical techniques. Therefore, convergence problems need to be reviewed when selecting the basis and testing functions. In this stage, choosing the basis functions is more connected to the convergence of MoM than choosing the testing functions.

2.2 Choice of Basis Functions

There are essentially two families of basis functions:

2.2.1 Entire Domain Basis Functions

In this case, mesh operation is not performed on the geometry. Each of $f_n(x)$ is defined and non-zero over the entire domain. Fourier expansion or a modal expansion such as Maclaurin, Chebyshev, Legendre polynomials are used to define these types of functions. Although yielding a good convergence of the method, it is not practical to define modes if the geometry is not regular. When the problem domain is irregular, then the determination of these basis functions is not an easy way in practice.

2.2.2 Sub-domain Basis Functions

In this case, mesh operation is performed on the geometry, and the problem domain is subdivided into smaller segments. Each of $f_n(x)$ is defined over the n-th subdomain and zero outside that domain. Mostly used sub-domain basis functions are pulse functions, triangular functions, sinusoidal functions, quadratic interpolation functions, trigonometric interpolation functions, etc. These functions are more flexible in adaption for arbitrary geometries. However, it needs to be aware of satisfying the edge condition (EC) by sub-domain bases. They also have an advantage in reducing the time for numerical implementation since the integration domains are smaller in sub-domain bases.

2.3 Choice of Weighting Functions

The most method types in choosing the testing functions are point matching method, method of collocation by subdomains, Galerkin's method, the method of least squares, and generalized weighting method.

2.3.1 Point Matching

In this choice, weighting functions are Dirac delta functions in the domain Ω;

$$w_m = \delta(x - x_m) \tag{2.11}$$

This method is straightforward to implement and simplifies the computations, but it may not yield an optimal convergence.

2.3.2 Method of Collocation by Subdomains

In this choice, weighting functions are selected as pulse functions.

$$w_m = \begin{Bmatrix} 1, & x \in \Omega_m \\ 0, & elsewhere \end{Bmatrix} \tag{2.12}$$

2.3.3 Galerkin's Method

In this case, weighting functions are chosen as the same as the basis functions.

$$w_m = f_m \tag{2.13}$$

2.3.4 Method of Least Squares

Weighting functions are a complex conjugate of the basis functions in the operator.

$$w_m = L\{\bar{f}_m\} \tag{2.14}$$

2.3.5 Generalized Weighting Method

If weighting functions are different from the ones defined above, it is called the generalized weighting method. In most of the applications, the Point Matching Method and Galerkin's Method are frequently used.

2.4 Developments in MoM Technique

Including iterative and non-iterative forms, there have been many studies for developing of application areas of MoM. The domain decomposition (DD) method is one of the most important procedures for this purpose. DD algorithms enable to split of the original problem into a number of smaller ones so that they can be analyzed independently. Then, they are reviewed together by applying integral BCs. By this means, the computational cost for a PC can be exceptionally reduced during the solution process.

A type of DD method has been revealed (Rao et al., 1982), and it relies on the substitution of special functions in a subdomain. These are called Rao–Wilton–Glisson basis functions, and a set of their linear combinations are implemented in that subdomain. Crucial to the formulation is the development of this set of unique subdomain basis functions. The procedure is applicable to both open and closed bodies in arbitrarily shaped objects and practiced to a flat square plate, a bent square plate, a circular disk, and a sphere.

As mentioned in the previous chapter, a fast algorithm has been developed as an FMP-MoM technique for surface-scattering problems (Coifman et al., 1993). Because the FMP accelerates the computation of the matrix-vector product, it reduces the computational complexity to O($N^{1.5}$) (Belenguer et al., 2005). Besides, in its improved version, the Multi-Level FMP has been used for solving electromagnetic wave scattering problems by using some iterative techniques (Rui et al., 2008). The computational complexity of the matrix-vector product operation was reduced to O(Nlog$N$), instead of O(N^3) obtained by using direct methods.

Conjugate gradient method (CGM) and fast Fourier transform (FFT) technique have been combined with MoM, and used for reducing storage and CPU time in the solution of EM scattering for three-dimensional (3D) dielectric bodies (Zhu et al., 2000). Radar cross-section (RCS) results are verified for dielectric and lossy dielectric scatters by comparing analytical methods. MOM-CGM-FFT mixed technique has proved rapid convergence and low run times on spheres with a range of permittivities and diameters up to 2λ.

Iterative solutions by using particular algorithms have been used to handle a dense main matrix based on the MoM. Forward-backward iterative algorithm has been presented for solving the 3D electric field integral equation (Brennan et al., 2004). Besides iterative forms, an iteration-free MoM approach has been presented for solving large multiscale EM scattering problems (Lucente et al., 2008). In this approach, special functions named characteristic basis functions are defined on macro domain blocks. Using these basis functions leads to a significant size reduction in the MoM matrix, and enables to handle the reduced matrix directly, without the need to iterate.

A higher-order DD method based on a hybridization of the FEM and MoM has been proposed for 3D modeling of scatterers (Ilic & Notaros, 2009). In the new FEM-MoM-DD technique, multiple FEM domains have been employed based on the surface equivalence theorem. It has been acquired a strong reduction in memory requirements and computational time compared to higher-order MoM solutions.

The physical optics driven method of moments (PDM) is another iterative DD method and proposed in (Tasic & Kolundzija, 2011). In each iteration, new macro-basis functions are created for each subdomain by the correctional PO currents based on the previous iteration. The weighting coefficients of all these functions are found from the PDM matrix equation. Hence, the original MoM equation is minimized, and the storage is proportional to $O(N^{1.5})$. The PDM provides a good accuracy of the RCS results in a few iterations; however, it is only applicable to closed perfect electric conductor (PEC) objects.

MoM weighted DD method has been proved in the improvement of MoM technique (Tasic & Kolundzija, 2018). It offers a solution for time-harmonic scattering from large objects by utilizing surface integral equations. This novel approach emphasizes fast convergence, and it provides to find the solution of electrically large scatterers simply and effectively.

CHAPTER THREE
LOCALIZATION PROCEDURE BY USING BEAM TYPE GREEN'S FUNCTION IN THE ELECTROMAGNETIC SCATTERING

3.1 Scattering Phenomena

Whenever an EM wave encounters an obstacle, EM interactions occur, such as reflection and various other diffraction mechanisms. If an incident wave illuminates an object, incident radiation interacts with this object, called the scatterer. In the absence of any scatterers, the incident field ($\vec{E}^{inc}, \vec{H}^{inc}$) is represented by the free-space radiation of the sources. However, in the presence of scatterers, the total field must be represented as a sum of the incident field and the scattered field ($\vec{E}^{sc}, \vec{H}^{sc}$) as following

$$\vec{E}^{total} = \vec{E}^{inc} + \vec{E}^{sc} \tag{3.1a}$$

$$\vec{H}^{total} = \vec{H}^{inc} + \vec{H}^{sc} \tag{3.1b}$$

Physically the meaning of scattering is that molecules, atoms, electrons, photons, and other particles are re-radiated the energy due to particle-particle collisions between them after absorption of the energy. This radiation can appear in different directions with different intensity.

The BCs on the fields over the surface of the structure dictate that surface currents flow. These currents are responsible for the generation of re-radiation, a scattered EM wave from the perfectly electric conductor (PEC), as shown in Figure 3.1.

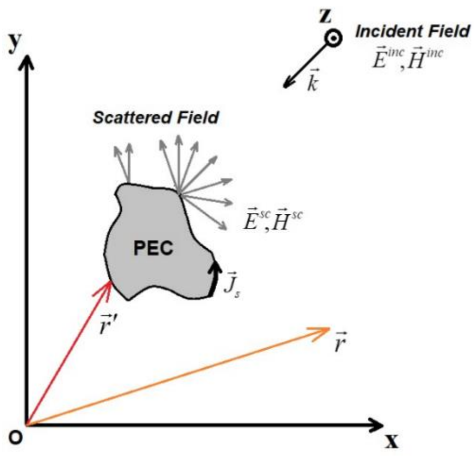

Figure 3.1 Scattering for 2D arbitrary geometry

The scattering of radio waves is particularly needful in radar systems. RCS usually represents EM scattering by a scatterer. It is an essential parameter in scattering and defined as a measure of power scattered from the incident wave. In practical terms, RCS is a property of the target's reflectivity, which means how detectable by radar. It depends on the size and geometric shape of the scattering body, frequency and polarization of the wave, and the observation angle. RCS (σ) of a target in 2D scattering is described as follows:

$$\sigma_{2D} = \lim_{r\to\infty}\left[2\pi r \frac{\left|E^{sc}\right|^2}{\left|E^{inc}\right|^2}\right] \tag{3.2}$$

where r is the distance of observation point from the origin, the RCS formula for H-field is in identical form. In the EM scattering problem, if the incident field is known, scattered and total fields can be found using various techniques, as mentioned in Chapter 1. Before the solution step, it must be determined that the corresponding fields are unique field distributions under the uniqueness theorem, which will be examined next part.

3.2 Uniqueness of Solution for Electromagnetic Scattering Problems

In the solution of the EM scattering problems, proving of some conditions is a necessity for a novel method to be valid. The idea of the uniqueness theorem is that the problem always has a unique solution that satisfies uniqueness conditions of scattering. First of these conditions of uniqueness is that the field satisfies of Helmholtz Equation. Additional conditions such as radiation condition, EC and BC must be verified for this new method to be confirmed (Hayashi, 1996).

3.2.1 Helmholtz Equation

We consider the solution of the wave equation in the absence of external charge or current. For the geometry of Figure 3.1, the wave equation for the field in 2D is derived from Maxwell’s Equations for a uniform isotropic linear and unbounded medium as follow:

$$\nabla^2 \vec{E}_z(\vec{r},t) - \frac{1}{c^2}\frac{\partial^2}{\partial t^2}\vec{E}_z(\vec{r},t) = 0 \tag{3.3}$$

where $\vec{r}$ is a position vector as shown in Figure 3.1, t is time variable, c is the speed of light in a medium with permeability μ and permittivity ε, and ∇^2 is the Laplace operator. The wave equation for H-field is in the identical form $\vec{H}_z$.

If we are only interested in the form of EM waves at a particular frequency, the EM wave equation for E-field reduces to the Helmholtz Equation

$$\nabla^2\vec{E}_z(\vec{r}) + k^2\vec{E}_z(\vec{r}) = 0 \tag{3.4}$$

where k is the wavenumber and the same equation is in the identical form for H-field.

The Helmholtz Equation represents a time-independent form of the wave equation and derived from Maxwell's Equations. If an EM wave satisfies Helmholtz Equation, it means that it also satisfies Maxwell's Equation.

3.2.2 Radiation Condition

The radiation condition must be imposed on the behavior of the field by discriminating outgoing and incoming waves at infinity so that the solution of a field equation is unique. Sommerfeld's radiation condition is introduced to verify the condition that no source exists at infinity. In this way, the scattered fields $\vec{E}^s$ and $\vec{H}^s$ must satisfy the following Sommerfeld radiation condition:

$$\lim_{r\to\infty}\sqrt{r}\left(\frac{\partial\vec{E}^s}{\partial r} + jk\vec{E}^s\right) = 0 \tag{3.5a}$$

$$\lim_{r\to\infty}\sqrt{r}\left(\frac{\partial\vec{H}^s}{\partial r} + jk\vec{H}^s\right) = 0 \tag{3.5b}$$

3.2.3 Boundary Condition

BCs are derived from deviations of the fields from one medium to another across the discontinuous boundaries and relating them to the distributions of charge and current. If the boundary surface is a perfect electric conductor (PEC), the main BCs are

$$\vec{E}_t = 0 \tag{3.6a}$$

$$\vec{H}_t = \vec{J}_s \tag{3.6b}$$

where $\vec{J}_s$ is a surface electric current density, while the subscript *t* indicates tangential components. That means that the tangential components of magnetic fields are discontinuous with the surface current density, while the tangential components of electric fields are continuous on the boundary. These are to be implemented for EM scattering problems that have a PEC surface.

3.2.4 Edge Condition

In a 2D case, if the boundary has sharp edges on the cross-section of the scatterer geometry, then the ECs are necessary to be satisfied. EC is an assumption for the uniqueness of a solution, depending on finite energy around an edge. In other words, EC states that the EM energy density must be integrable over any finite volume on edge. This domain can also contain singularities of the EM field. Mathematically, we can declare that this condition is equivalent to finite energy for equations as follows:

$$\int_v |E_u|^2 dv \qquad \text{and} \qquad \int_v |H_u|^2 dv \tag{3.7}$$

where *u* denotes any component of either field, and *v* is any finite volume around the edges. This condition means that the stored energy in any finite volume of space is finite.

3.3 Integral Equation Method

The incident field that impinges on the surface *S* of the scatterer body induces an electric current density $\vec{J}_s$ on it. This current density causes a radiation that is referred to as the scattered field. If $\vec{J}_s$ is known, the scattered field can be found. Here, the scattered field is presented for the PEC structure in Figure 3.1 using the Integral Equation Method. In general, there are two forms of integral equations for EM scattering, which are the electric field integral equation (EFIE) and the magnetic field integral equation (MFIE). Each integral equations is a formulation based on the BC of tangential parts of the fields. As declared in part 3.2.3, the BC on a PEC surface of the scattering object is that the total tangential electric field is to be zero.

$$\vec{E}_t^{\,total}(r_s) = \vec{E}_t^{\,inc}(r_s) + \vec{E}_t^{\,sc}(r_s) = 0 \tag{3.8}$$

where r_s is the distance from the origin to any point on the surface of the scatterer body. The scattered field can be expressed in terms of the vector potential

$$\vec{E}^{sc}(\vec{r}) = -j\omega\vec{A}(\vec{r}) - j\frac{1}{\omega\mu\varepsilon}\nabla(\nabla\cdot\vec{A}(\vec{r})) \tag{3.9}$$

where ω is the angular frequency of the wave. The vector potential is formed by using Hankel function

$$\vec{A}(\vec{r}) = -\frac{j\mu}{4}\int_{C_t}\vec{J}_s(\vec{r}')H_0^{(2)}(k|\vec{r}-\vec{r}'|)d\ell' \tag{3.10}$$

where $H_0^{(2)}$ is the Hankel function of zero-order and second kind, C_t is the counter-clockwise path of the cross-sectional contour in Figure 3.1 and $d\ell'$ is the infinitesimal path length on the PEC cylinder. Then, the scattered field is written as below

$$\vec{E}^{sc}(\vec{r}) = -\frac{k\eta}{4}\int_{Ct}\vec{J}_s(\vec{r}')H_0^{(2)}(k|\vec{r}-\vec{r}'|)d\ell' - \frac{\eta}{4k}\nabla\int_{Ct}\nabla'\cdot\vec{J}_s(\vec{r}')H_0^{(2)}(k|\vec{r}-\vec{r}'|)d\ell' \tag{3.11}$$

where η is the intrinsic impedance. When the source is located at the arbitrary position r', and 2D Green's function is denoted in terms of Hankel function as below:

$$G(\vec{r}-\vec{r}') = -\frac{j}{4}H_0^{(2)}(k|\vec{r}-\vec{r}'|) \tag{3.12}$$

Substituting Green's function and using the BC equation (3.6a) into the scattered formula, then it forms:

$$\vec{E}^{inc}(\vec{r}=\vec{r}_s) = jk\eta\int_{Ct}\vec{J}_s(\vec{r}')G(\vec{r}_s-\vec{r}')d\ell' + j\frac{\eta}{k}\nabla\int_{Ct}\nabla'\cdot\vec{J}_s(\vec{r}')G(\vec{r}_s-\vec{r}')d\ell' \tag{3.13}$$

where ∇ and ∇' are the gradients concerning the observation (unprimed) and source (primed) coordinates, respectively. Since the left-hand side is stated in terms of the known incident electric field, it is referred to as the EFIE. It can be used to find out the current density $\vec{J}_s(\vec{r}')$ on the scatterer surface. Once $\vec{J}_s$ is determined, the scattered field is found.

Alternatively, the magnetic field integral equation MFIE can be derived for the solution of the problem by using the tangential components of the magnetic field. As stated in part 3.2.3, one of the BCs on the PEC surface of the scattering object relates to the total electric current density induced on the surface. However, with some variations for Green's function in this thesis, electric current density function obtained by using hybrid techniques is not a realistic function, and it is non-physical. Thus, MFIE can not be employed in the solution for hybrid techniques presented in this thesis. Also, in the solution of the MFIE by the MoM, singularities arise and should be handled by some techniques (Hodges & Rahmat-Samii, 1997; Gürel & Ergül, 2005). It should be noted that the MFIE is valid only for closed surfaces, while EFIE can be used for both closed and open bodies. By taking the combination of these two Integral Equations, Combined Field Integral Equation (CFIE) can also be obtained. Closed structures should be modeled with CFIE due to its problem of the resonant frequency. In this thesis, EFIE was formulated for all structures and utilized without considering the resonant frequency that is only active in a very narrow frequency region.

3.4 The New Localization by Using Beam Type Green's Function

We intend to propose a new hybrid method that is integrated with MoM. As explained in Chapter 2, the scatterer surface is discretized through the MoM solution, and some coordinate points are constituted on the surface at the end of the meshing process. Since the surface current is a combination of the basis functions after the discretization, these points are referred to as source points for the surface current. The radiation of these source points is found by using free-space Green's function, and it has an omnidirectional field property, as shown in Figure 3.2. Therefore, the radiation obtained from one of these sources almost covers all testing functions in the geometry. In Chapter 2, if the main impedance matrix Z_{mn} is elaborated, a source point indicated n interacts with all testing points indicated m in the testing procedure of MoM, and it operates for all n and m indices. These interactions end up with many non-zero elements in the impedance matrix and put it into a dense form. It would be required a countless number of unknowns to find out the current density, especially in large geometries. That means excessive memory storage and CPU time in the solution. Hence, the MoM is a valid method with a modest CPU solution time. For the larger dimensions than a particular size of the scatterer, the MoM would not be a possible solution due to the insufficient number of memory storage.

However, instead of an omnidirectional wave, the radiation of a source point can be found mathematically as a directed wave, like a beam pattern radiating through a narrow region, as shown in Figure 3.2. If the source point is converted to a beam type model by using an analytical way, its radiation can be restricted to interact with the fewer testing points. As shown in Figure 3.2, by implementing beam-type Green's function, the radiation of the source points in the non-near edge region becomes a beam nature with the beam aperture on the scatterer surface. Thus, there would be a limitation in the interaction between testing functions and the radiation field of the basis functions, which is the effect of cell *n* on cell *m* in the main matrix. Therefore, only the near-field interactions are possible. Decreasing these interactions leads the main impedance matrix to a sparse form and reduces memory requirement, as explained in the next part. It can be seen that limited interactions are related to the size of the beamwidth, which is γ in Figure 3.2. This procedure can be named localization of the source since the radiation of the source is only responsible for a restricted region. The meaning of the localization is that the number of observation points affected by a source point becomes confined. Then, the radiation of the source point is almost localized on the scatterer surface, and it is performed by the new Green's function after the localization procedure. A particular localized Green's function can be used to generate a field only if it satisfies all uniqueness conditions expressed in the previous section. After the numerical solution part, instead of the real surface current, a pseudo-current function is obtained by utilizing the non-realistic modified Green's function.

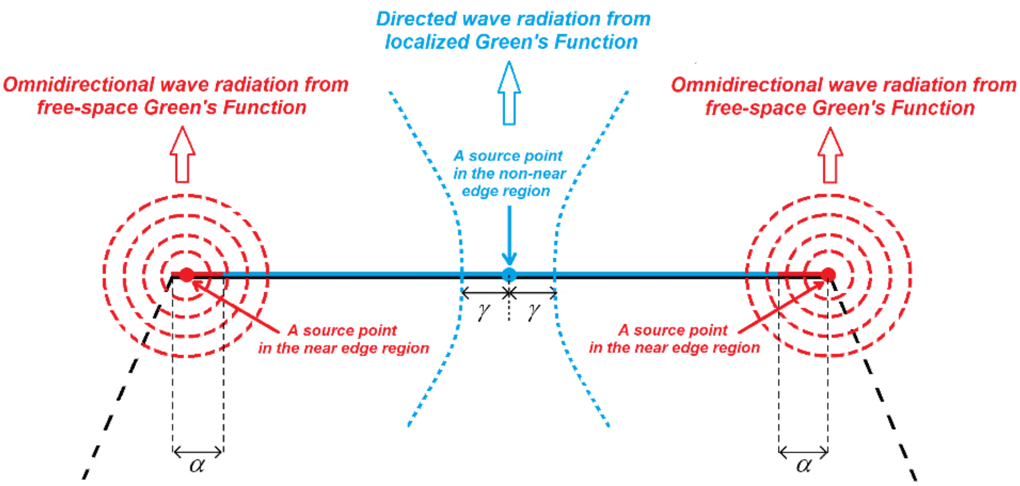

Figure 3.2 Sources and radiations for N-sided a convex polygon cross-sectional cylinder

After verifying the Helmholtz Equation and Radiation Condition for the new Green's function, the third definement BC should be applied. Equation (3.13) is a valid statement performed by the BC for the PEC structure. If the localized Green's function is used in (3.13) instead of free-space Green's function, only one condition remains needed to be satisfied, which is the EC. Therefore, a few basis functions near the edges are set free, and they radiate by the free-space Green's function. Thus, it should be considered that they make their interactions with all other testing functions, and these interactions can be computed by using the standard MoM procedure. Consequently, the localization procedure can be employed for the source points in the region of the structure, which is not near the edges.

In conclusion, the localized Green's function, which satisfies Helmholtz Equation and Radiation Condition, can be utilized for PEC structure by implementing the EC and BC. It should be noted that the beamwidth of the localized Green's Function must be bounded. It must be smaller than the width of the near edge regions. Otherwise, the radiation of the beams can affect the edge points, which causes the EC to be a failure. In addition to this, the beam size of the localized Green's function can be narrow as less as possible.

Figure 3.3 indicates the source points in the near edge regions with red zones, which are used in the standard MoM procedure. On the one hand, free-space Green's Function is employed with a regular basis and testing functions based on MoM for these source point radiations. On the other hand, localized Green's Function based on beam pattern is utilized for the source point radiations at the blue zones indicating the non-near edge regions. The far element interactions for the basis and testing functions can be neglected due to the nature of the beams locating at the non-near edge regions. Therefore, the main impedance matrix turns to be a sparse form. This type of impedance matrix localization provides to analyze larger geometries by using highly efficient sparse matrix solution methods. Hence, very large geometries in 2D can be modeled by this procedure.

On an electrically large scatterer, there may be a vast region on its surface that is not near the edges. In filling the impedance matrix for the sources in that region, only the near field interactions can be considered that they are on the same edge with the source. Consequently, any source radiation of the localized Green's function does not interact with the testing points on the other faces. So there is no need for a special algorithm like in FMP or in the CSP expansion-based MoM. Then all interactions should be considered only for a few basis functions near to the edges. Also, one can say that the number of testing functions for these interactions is limited by N. Consequently, for 2D problems, the memory storage and the operation count are almost proportional to N, i.e., O(N).

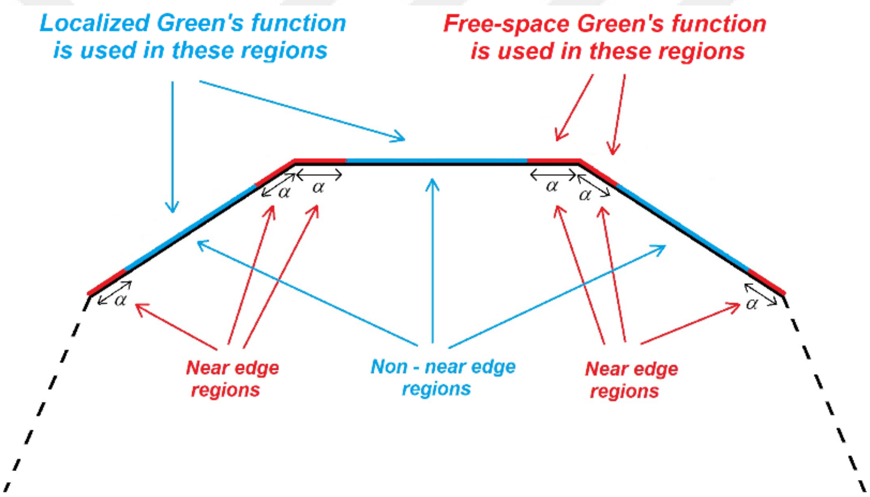

Figure 3.3 N-sided a convex polygon cross-sectional cylinder

Figure 3.3 can be taken into consideration for a strip geometry by designating a single facet in the contour. Moreover, the configuration is also related to open body structures and can be adapted to make a localization for these structures.

It should again be noted that the field obtained from the localized Green's function must be satisfied with all uniqueness conditions of the scattering problems. Under the circumstances, this procedure has two main advantages. Firstly, solution time can be lowered significantly versus standard MoM in large geometries. Secondly, it offers to analyze the problems of very large geometries that can not be solved with standard MoM or any technique due to the memory requirements. In this thesis, the beam type radiation is implemented by presenting the two new hybrid techniques, as mentioned in part 1.3. The definitions of the beam type Green's function are also detailed in Chapter 4 and Chapter 5.

3.5 Reducing Memory Requirement and Sparsity of the Main Matrix

Two parameters could affect the memory requirement in the procedure. One is the length of the near edge regions, which is indicated α, as shown in Figure 3.2 and Figure 3.3. This length identifies the unknown numbers concerning the edge points. The total number of discretization N is equal to follow:

$$N = L/\Delta \tag{3.14}$$

where L is the total length of the cross-sectional area and Δ is the step interval on the cross-sectional contour. The parameters α, L, and Δ are in terms of λ.

In the standard MoM, as Green's Function is a type of an omnidirectional wave, a source point would interact all testing points within discretization in the region. Hence, a source point in the near edge region has a great number of interactions with the testing points as many as N. Consequently, the total number of interactions from a near edge region is

$$(\alpha / \Delta) \cdot N \tag{3.15}$$

The other one is the width of the localized Green's function, and it indicates the unknown numbers relating to the non-near edge points. After the formulation process, a beam pattern is utilized in the non-near edge regions; the radiation is qualified to a specific area for a source point in this region during the testing procedure. If the localized Green's function has a beam waist γ, as shown in Figure 3.2, for a single source point in the non-near edge region, the interaction points on the testings would be $2\gamma/\Delta$. It should be noted that the beam type radiation of this source point interacts with the testing points only on the same facet because the beam radiates outward from the facet. Thereby, the memory storage elements for a PC or the total interaction number of the main matrix elements are calculated as follows:

$$\left(\frac{\alpha}{\Delta}N_e\right)\cdot N+\left(N-\frac{\alpha}{\Delta}N_e\right)\cdot\frac{2\gamma}{\Delta} \;\approx\; N\cdot\left(\frac{2\gamma}{\Delta}+\frac{\alpha}{\Delta}N_e\right) \tag{3.16}$$

where N_e is the number of near-edge parts on the cross-sectional contour, for example, it is equal to two, for the strip geometry. In the left-hand part of the equation above, the first term denotes the number of elements from the near-edge regions, and the second term denotes the number of elements from the non-near edge regions. Although the memory requirement in the usual MoM is O(N^2), there is a reduction substantially in the proposed method.

Let us consider a strip with a length of 10λ, length of the near edge regions α = 1λ, and the localized Green's function has a beam waist γ = 1λ. If the interval Δ is set to λ/10, then the total number of discretization becomes N = 100 from (3.14). The memory storage elements for a PC is found:

$$N\cdot\left(\frac{2\cdot 1\lambda}{0.1\lambda}+\frac{1\lambda}{0.1\lambda}\cdot 2\right)=40N \tag{3.17}$$

while it is 100N for the MoM. If we evaluate the situation for a square cross-section cylinder with the same parameters, the number of near-edge parts on the cross-sectional contour will be N_e = 8, and the result is:

$$N\cdot\left(\frac{2\cdot 1\lambda}{0.1\lambda}+\frac{1\lambda}{0.1\lambda}\cdot 8\right)=100N \tag{3.18}$$

while it is 400N for the MoM. Although it seems like there was no significant difference, the substantial advantage would arise in the number of memory storage elements for larger geometries because the total number of discretization N reaches a very high level, as the structure size is getting larger.

CHAPTER FOUR

MAIN MATRIX LOCALIZATION FOR 2D SCATTERING BY USING CSP TYPE GREEN'S FUNCTION

4.1 CSP Vector Expression and Beam Generation

The first step in the derivation of the localized Green's Function is to obtain a directional CSP beam. For the localization of source radiation in the non-near edge region, omnidirectional radiation is converted to a directive beam by using the CSP method. The real position vector r' at the source coordinate is replaced by a complex quantity to express a CSP vector (Felsen, 1976):

$$\vec{r}' \rightarrow \vec{r}'_{csp} = \vec{r}' - j\vec{b} \tag{4.1a}$$

$$\vec{b} = \hat{b}b \tag{4.1b}$$

where j is an imaginary unit, b is defined as the beam aperture and a positive real number, while the unit vector $\hat{b}$ defines the direction of the beam. Figure 4.1 gives the line source geometry and CSP model in the same figure. The $\vec{r}'$ gives the location of the source in real space. It is considering a beam that radiates from the real point r' in any direction with the angle θ_{csp}. If $\vec{r}'$ is converted to $\vec{r}'_{csp}$ and used in the Green's function; then, the omnidirectional cylindrical wave becomes a directional beam field.

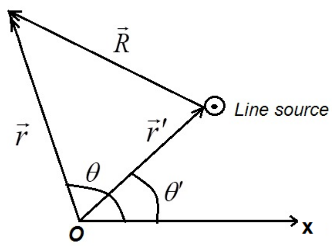

(a)

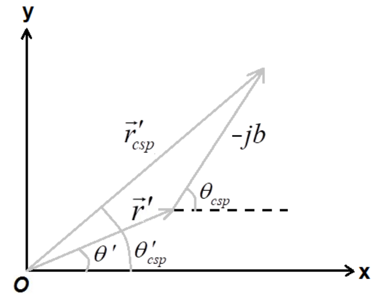

(b)

Figure 4.1 (a) Line source geometry (b) Complex source point model geometry

In the presence of a line source at $(\vec{r}', \theta')$, its z-directed field is isotropic at any observation points $(\vec{r}, \theta)$. The scalar 2D free-space Green's function is defined by the wave equation

$$(\nabla^2 + k^2)\, G(\vec{r}, \vec{r}') = -\delta(\vec{r}, \vec{r}') \tag{4.2}$$

where δ is a Dirac-delta function, and its solution is well-known, as shown below:

$$G(\vec{r},\vec{r}') = -\frac{j}{4} H_0^{(2)}(kR) \tag{4.3}$$

where R is the distance from the source to the observation point:

$$R = \sqrt{r^2 + r'^2 - 2rr'\cos(\theta - \theta')} \tag{4.4}$$

In the far field ($r \gg r'$), $R \cong r - r'\cos(\theta - \theta')$ is applied in the phase term and $R \cong r$ in the amplitude term. Then, the large asymptotic argument of Hankel function is utilized as below:

$$\lim_{R\to\infty} H_0^{(2)}(kR) = \sqrt{\frac{2j}{\pi kr}} e^{-jkR} \qquad kR \gg 1 \tag{4.5}$$

$$G(\vec{r},\vec{r}') = C\frac{e^{-jkr} e^{jkr'(\cos(\theta-\theta'))}}{\sqrt{kr}} \qquad 0 < \theta' < \pi \tag{4.6}$$

where C is a complex constant. In the light of equation (4.1), we define vectors in polar coordinates:

$$\vec{r}' = (r', \theta') \tag{4.7a}$$
$$\vec{r}'_{csp} = (r'_{csp}, \theta'_{csp}) \tag{4.7b}$$
$$\vec{b} = (b, \theta_{csp}) \tag{4.7c}$$

where $\vec{r}'$ is a real source position, $\vec{r}'_{csp}$ is a complex source position and $\vec{b}$ is a complex beam vector. All angles are measured from the x-axis. The values of $\vec{r}'_{csp}$ and θ'_{csp} are:

$$r'_{csp} = \sqrt{r'^2 + 2jr'b\cos(\theta_{csp} - \theta') - b^2} \qquad \mathrm{Re}(r'_{csp}) > 0 \tag{4.8}$$

$$\theta'_{csp} = \cos^{-1}\left(\frac{r'\cos(\theta') + jb\cos(\theta_{csp})}{r'_{csp}}\right) \tag{4.9}$$

where b > 0 and $0 \le \theta_{csp} \le 2\pi$. In equation (4.6) of Green's Function, replacing real source position $\vec{r}' = (r', \theta')$ by complex source position $\vec{r}'_{csp} = (r'_{csp}, \theta'_{csp})$, gives CSP type Green's Function as:

$$G_{csp}(\vec{r},\vec{r}'_{csp}) = C\frac{e^{-jkr} e^{jkr'_{csp}(\cos(\theta-\theta'_{csp}))}}{\sqrt{kr}} \qquad r \gg |\vec{r}'_{csp}| \tag{4.10}$$

From Figure 4.1b:

$$r'_{csp}\cos(\theta'_{csp}) = r'\cos(\theta') - jb\cos(\theta_{csp}) \tag{4.11a}$$
$$r'_{csp}\sin(\theta'_{csp}) = r'\sin(\theta') - jb\sin(\theta_{csp}) \tag{4.11b}$$

Using these equations to solve the equality (4.12a) and we obtain (4.12b) :

$$r'_{csp}\cos(\theta-\theta'_{csp}) = r'_{csp}\cos(\theta)\cos(\theta'_{csp}) + r'_{csp}\sin(\theta)\sin(\theta'_{csp}) \tag{4.12a}$$

$$r'_{csp}\cos(\theta-\theta'_{csp}) = r'\cos(\theta-\theta') + jb\cos(\theta-\theta_{csp}) \tag{4.12b}$$

Substituting 4.12(b) into the CSP type Green's Function with complex source position

$$G_{csp}(\vec{r},\vec{r}'_{csp}) = C\frac{e^{-jkr}e^{jkr'(\cos(\theta-\theta'))}}{\sqrt{kr}}\cdot e^{kb(\cos(\theta-\theta_{csp})} = G(\vec{r},\vec{r}')\cdot e^{kb(\cos(\theta-\theta_{csp})} \tag{4.13}$$

It is found that equation (4.13) represents an omnidirectional cylindrical wave, which is the free-space Green's function, modulated by a beam pattern $e^{kb(\cos(\theta-\theta_{csp})}$. This pattern has its maximum in the direction $\theta=\theta_{csp}$ and minimum in the direction $\theta=\theta_{csp}+\pi$. The radiation field of a complex line source locating at the complex position $\vec{r}'_{csp}$ with amplitude C is given by:

$$G_{csp}(\vec{r},\vec{r}'_{csp}) = CH_0^{(2)}(kR_{csp}) = CH_0^{(2)}(k|\vec{r}-\vec{r}'_{csp}|) \tag{4.14}$$

where R_{csp} is the distance between the observation point and the CSP. Consequently, to obtain the radiation field of a source point locating at the complex position, we replaced $\vec{r}'\to\vec{r}'_{csp}$ in the free-space Green's function.

Consider a strip lying on the x-z plane, to review the CSP beam pattern function used in this thesis, it is assigned the beam parameter $\theta_{csp}=90^o$ normal to the strip surface to specify the beam direction. If a real source point is considered on the x-plane, then the real source position $\vec{r}'$, the observation point vector $\vec{r}$, and the CSP vector $\vec{b}$ are defined as below:

$$\vec{r}' = x'\hat{x} \tag{4.15}$$

$$\vec{r} = x\hat{x} + y\hat{y} \tag{4.16}$$

$$\vec{b} = b\hat{y} \tag{4.17}$$

The real source point vector $\vec{r}'$ is converted to CSP vector by using $\vec{r}'_{csp} = \vec{r}' - j\vec{b}$ and it yields:

$$\vec{r}'_{csp} = x'\hat{x} - jb\hat{y} \tag{4.18}$$

Then the distance vector of the observation point from the CSP is given as below:

$$R_{csp} = |\vec{r}-\vec{r}'_{csp}| = \sqrt{(x-x')^2+(y+jb)^2} \tag{4.19}$$

and CSP type Green's Function is written as:

$$G_{csp}(\vec{r},\vec{r}'_{csp}) = CH_0^{(2)}(k\sqrt{(x-x')^2+(y+jb)^2}) \tag{4.20}$$

Then, we need to find out the behavior of CSP type Green's function in the regions far from the CSP. This characteristic is an essential criterion since it states the effectivity of the localization process for CSP type Green's function. By selecting different b values, and the source point on the x-plane $(x'=0, y=0)$, then the normalized intensity of CSP type Green's function $G_{csp}(\vec{r}',\vec{r}'_{csp})$ versus x/λ is plotted in Figure 4.2. Here, the complex line beam field $|G_{csp}|$ is normalized to the maximum value of radiation.

It is clearly seen that the normalized beam field suddenly drops to minimal values if $|x|>b$, as shown in Figure 4.2. These minimal values can be approximated by zero for CSP type Green's function. Therefore, there would be almost no field value in the region $G_{csp}(x<-1\lambda, y=0)$ and $G_{csp}(x>1\lambda, y=0)$, when b = 1λ. In other words, if the basis function is on the (x=0, y=0) point, it will be interacting with testing functions only for a particular distance, which is ±b away from the x=0 point. This limitation of the interactions provides a strong localization of the main matrix so that many of its elements are very close to zero and can safely be neglected. This localization converts the main matrix into a sparse one, which is an attractive achievement since there are specific algorithms to solve the sparse matrices more efficiently compared to the full matrices. As known, typically in MoM, the total unknowns are large quantity numbers that restrict its application to the analysis of electrically large geometries. It should be noted that there is a singularity based on the Hankel function at the points of ±1λ when b = 1λ, and ±2λ when b = 2λ in Figure 4.2. These singularities should be taken into account and extracted from the process during the solution part.

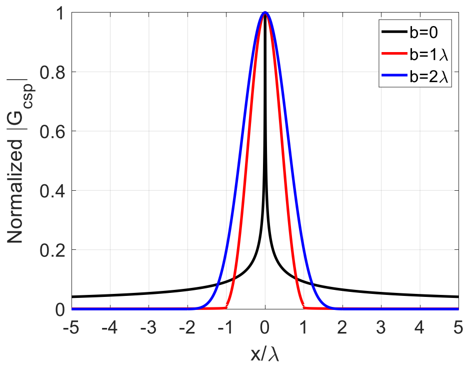

Figure 4.2 Normalized beam field $|G_{csp}|$ versus x/λ

Isotropic cylindrical waves due to the line source and CSP beam fields are illustrated in Figure 4.3. The differences in the radiation are visible clearly.

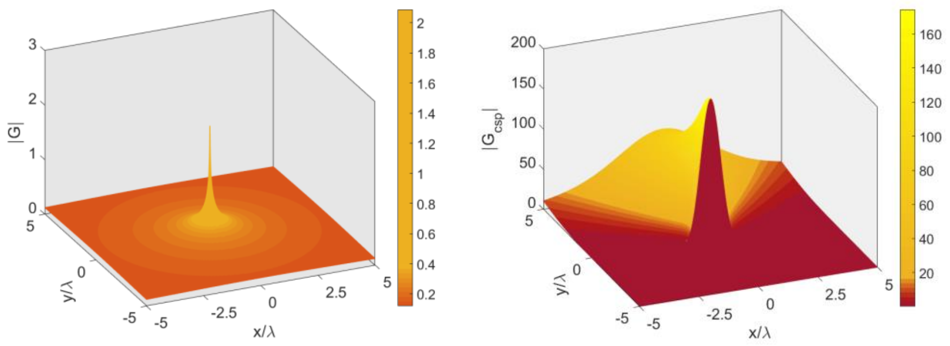

(a) (b)

Figure 4.3 Normalized beam field radiation at x=0, y=0, versus x/λ and y/λ (a) Omnidirectional cylindrical wave radiation (b) CSP type beam wave radiation for b = 1λ

The necessary examination of the CSP beam field is that it satisfies all uniqueness conditions pointed out in section 3.2:

1- Helmholtz equation: Modified Green's function with the CSP method satisfies the Helmholtz equation. Since it is described in terms of the free-space Green's function with a complex source location, the field of a CSP is an exact solution of the wave equation everywhere in space except in its singularities.

2- Radiation condition: Modified Green's function satisfies radiation condition because it is modulated wave by a beam pattern $e^{kb(\cos(\theta-\theta_{csp})}$, which does not include spatial parameter r.

3- Boundary condition: These conditions are imposed during the solution procedure to obtain the scattering fields.

4- Edge condition: A region at near edges must be set free depending on beam parameter b to satisfy this condition. At near edges, free-space Green's function is used so that the energy must be finite. If the beam field is examined in Figure 4.3b, it can be seen that the beam radiation tends to extend to infinity at just the point in the middle of it. Therefore, b is taken as *zero*, and modified Green's function can not be used for the near-edge regions.

Hence, an arbitrary EM field that arises from a real source point can be converted to a CSP beam pattern function, which serves as a useful tool to find the radiation of the basis function. In the next part, CSP type beam field radiation will be implemented as a hybrid method, and it is combined with MoM. Firstly, finite width PEC strip geometry illuminating by a plane wave will be examined to verify the presented method for both polarizations. Strip geometry is a practical case and considerable for many applications. Beam parameters, like beam aperture and direction of the beam, will be investigated in detail. In light of this information, the more complex structure, that is, closed PEC cylindrical geometry, will be studied for the presented method for both polarizations.

4.2 2D Scattering From A Large PEC Strip

4.2.1 MoM Procedure with CSP Type Green's Function

4.2.1.1 E-polarization

The problem geometry is a flat PEC strip, as shown in Figure 4.4, with a strip length L, and it is illuminated by an EM plane wave. For the E-polarization case in MoM, we assumed the pulse type basis and testing functions. The current density has only z components because of the polarization of the incident plane wave. Moreover, due to the geometry, there is no variation in the current density along the z-axis, and it can be thought as a combination of the line sources. For a strip geometry lying on the xz-plane, the second term vanishes in (3.13), and it becomes as below:

$$E_z^{inc} = jk\eta \int_0^L J_z(x') G(\vec{x} - \vec{x}') dx' \qquad (4.21)$$

$G(\vec{x} - \vec{x}')$ is the 2D free-space Green's function for the geometry of Figure 4.4 and is defined in parallel to the equation (3.12).

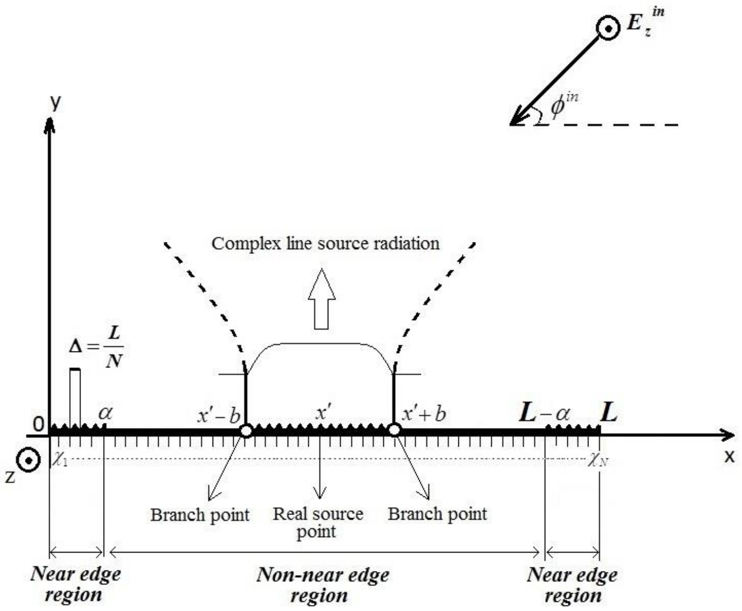

Figure 4.4 Cross-section geometry of the finite width flat PEC strip illuminated by a plane wave

For the non-near edge region, the beam-type radiation is needed to be derived, and its idea was explained before. A beam is launching from the x-axis to the upward y-direction, as in Figure 4.4. To obtain a directional CSP beam for the strip geometry, we again use the same method in parallel to the equation (4.1a):

$$\vec{x}' \rightarrow \vec{x}'_{csp} = \vec{x}' - j\vec{b} \tag{4.22}$$

If $\vec{x}'$ is converted to $\vec{x}'_{csp}$, then the omnidirectional wave becomes a beam field. To realize this conversion in the equation (4.21), the coordinate of the real line source is replaced with the complex position in the Green's function of EFIE:

$$E_z^{inc} = jk\eta \int_0^L J_z^{csp}(\vec{x}') G_{csp}(\vec{x} - \vec{x}', b(\vec{x}')) d\vec{x}' \tag{4.23}$$

Here $J_z^{csp}(\vec{x}')$ is the unknown current density function different from the physical current on the strip and G_{csp} is the CSP type Green's function in parallel to (4.20), and it is given as:

$$G_{csp}(\vec{x} - \vec{x}', b(\vec{x}')) = \frac{-j}{4} H_0^{(2)}\left(k\sqrt{(x - x')^2 - b(x')^2}\right) \tag{4.24}$$

Here, $b(x')$ is the beam parameter, which depends on the source position:

$$b(x') = \begin{cases} 0, & near\ edges \\ b, & non-near\ edges \end{cases} \tag{4.25}$$

It was observed that the beam type radiation of the complex line source, that is $|G_{csp}|$, becomes very small if $|x|>b$ as shown in Figure 4.2. Therefore, there will be almost no interaction between the source and observation elements on the strip if they are far enough from each other. This provides a strong localization of the main matrix so that many of its elements are approximated to zero. The CSP beam-like field is visible in Figure 4.3b.

As a first step, the geometry is discretized for MoM procedure, as described in Chapter 2. The discretization points, as shown in Figure 4.4, are described as below:

$$\chi_n = (n-1)\Delta + \Delta \qquad n = 0,1,2,\ldots..N \tag{4.26}$$

At the second step, the unknown current density is expanded into a series with basis functions multiplied by unknown constants as MoM procedure:

$$J_z^{csp}(x') \cong \sum_{n=1}^{N} a_n p_n(x') \tag{4.27}$$

where a_n*'s* are the unknown coefficients to be determined, $p_n(x')$ is a pulse function represented as basis functions and defined as:

$$p_n(x') = \begin{cases} 1, & \chi'_{n-1} \le x' \le \chi'_n \\ 0, & elsewhere \end{cases} \tag{4.28}$$

These chosen basis functions are defined only in a particular domain, so they allow to reduce the integral limits over the strip length L. Substituting the current density expansion into (4.23), it becomes:

$$E_z^{in} = jk\eta \sum_{n=1}^{N} a_n \int_{x_n-\Delta/2}^{x_n+\Delta/2} p_n(x') G_{csp}(\vec{x}-\vec{x}', b(\vec{x}'))dx'dx \tag{4.29}$$

where Δ is the discretization length of the strip surface, and it is selected by following the rule-of-the-thumb discretization criteria as λ/10. However, it can be further increased for better solutions. The definitions of x_n's are the middle points of the basis and testing functions. The incident field is assumed as the electrically polarized EM plane wave $E_z^{in} = e^{jk(x\cos\phi^{in} + y\sin\phi^{in})}$. However, the equation (4.29) presents N unknowns for one observation point, and it is not a solution for the coefficients a_n*'s*. As stated in Chapter 2, it needs to be tested with testing functions. So it is multiplied for both sides by a set of functions $p_m(x)$ to obtain N equations for N unknowns:

$$\int_{x_m-\Delta/2}^{x_m+\Delta/2} p_m(x)E_z^{in}(x)dx = jk\eta\sum_{n=1}^{N} a_n \int_{x_m-\Delta/2}^{x_m+\Delta/2} p_m(x) \int_{x_n-\Delta/2}^{x_n+\Delta/2} p_n(x')G_{csp}(x-x',b_n)dx'dx \tag{4.30}$$

m=1,2,….N

This procedure is defined as the Galerkin procedure, and $p_m(x)$ is a pulse function. Here, b_n is the complex beam parameter depending on the source indices, i.e., the location of the basis function. It takes zero in the near edge regions, $b_n = 0$, and a real constant value in the non-near edge region $b_n = b$, on the strip.

Equation (4.30) is an algebraic matrix equation for the given problem in parallel to (2.9), and the coefficients a_n's are found by applying the matrix inversion methods. In this form, the main matrix and excitation vector can be written as follows:

$$Z_{mn} = \frac{k\eta}{4} \int_{x_m-\Delta/2}^{x_m+\Delta/2} p_m(x) \int_{x_n-\Delta/2}^{x_n+\Delta/2} p_n(x')H_0^{(2)}(k\sqrt{(x-x')^2 - b_n^{\,2}}\,dx'dx \tag{4.31}$$

$$g_m = \int_{x_m-\Delta/2}^{x_m+\Delta/2} p_m(x)e^{jkx\cos\phi^{in}}dx \tag{4.32}$$

m=1,2,….N

Equations (4.31) and (4.32) are matrices for *the MoM Procedure with CSP Type Green's Function* solution of the 2D strip geometry to determine the current density over the coefficients a_n. After the determination of the coefficients, by using them, one can define far zone fields as well as the near fields in the proposed method. It should be noted that they are MoM solution of the 2D strip geometry if $b_n = 0$ for all n values. Therefore, they are also used for near-edge regions in the proposed method by assigning $b_n = 0$. For reducing computational time, by the change of variable x-x'=u, the main matrix is now obtained as follows:

$$Z_{mn} = \frac{k\eta}{4} \int_{-\infty}^{+\infty} H_0^{(2)}(k\sqrt{u^2 - b_n^{\,2}}) \left[\int_{-\infty}^{+\infty} p_n(x')p_m(x'+u)dx' \right] du \tag{4.33}$$

The integral within the bracket is a convolution integral, and the convolution of two pulse functions is a triangle function with 2Δ width. Consequently, the double integral in the main matrix can be reduced to a single integral form for computational cost as below:

$$Z_{mn} = \frac{k\eta}{4}\left[\int_{v_{mn}-\Delta}^{v_{mn}} H_0^{(2)}(k\sqrt{u^2 - b_n^{\,2}})(u - v_{mn} + \Delta)du + \int_{v_{mn}}^{v_{mn}+\Delta} H_0^{(2)}(k\sqrt{u^2 - b_n^{\,2}})(-u + v_{mn} + \Delta)du \right] \tag{4.34}$$

where $v_{mn}= x_m$-x_n. The first integral indicates the lower triangle function, and the second one indicates the upper triangle function.

In the MoM solution procedure, the Toeplitz type matrix structure appears in this type of flat geometry. Toeplitz matrix has a hierarchy of shift-invariant, and a particular symmetrical case is produced for interactions of the elements in the main matrix. In other words, the radiation is the same for different indexes with the same distance between the source location and the testing location. For example, if n=1 and m=10 in the main matrix Z_{mn}, the interaction is the same as in the case of n=2 and m=11. Thus, one row in the main matrix is only needed to be calculated, then Z_{mn} is created from this row utilizing Toeplitz property. However, the Toeplitz symmetry is disappeared and can not be utilized in the proposed method. Despite this deficiency compared to the MoM, there has been huge time gain in the solution for very large flat strip geometry in the proposed method.

In Green's functions, the Hankel function, which consists of two Bessel functions, has a singularity when it goes zero. Therefore, low arguments of Bessel functions are required to extract the singularity, and the Hankel function becomes as follows with asymptotic methods:

$$\underset{u\to 0}{H_0^{(2)}}(k|u|) = 1 - \frac{2j}{\pi}\ln\left(\frac{\xi u}{2}\right) \tag{4.35}$$

where ξ is the Euler's constant and equals to 1.781. The singularity extraction procedure was also performed at the branch points of the complex line source located at $x = x'+b$ and $x = x'-b$ in Figure 4.4, where b is a selectable beamwidth parameter. This extraction is implemented to MoM and the proposed method when the Hankel function tends to zero. Also, the extraction has a factor for the accuracy of the obtained solution.

4.2.1.2 H-polarization

In Figure 4.4, the incident field for the H-polarization is assumed as a plane wave $H_z^{in} = e^{jk(x\cos\phi^{in} + y\sin\phi^{in})}$, instead of E_z^{in}. Triangle functions are chosen as basis functions because the BCs must be satisfied on the edges; that is, the current needs to be zero on the edges. They are defined as:

$$t_n(x') = \begin{cases} (x' - \chi'_n)/\Delta + 1, & \chi'_n - \Delta \le x' \le \chi'_n \\ -(x' - \chi'_n)/\Delta + 1, & \chi'_n < x' \le \chi'_n + \Delta \\ 0, & elsewhere \end{cases} \tag{4.36}$$

In this case, the total number of discretization is chosen N-1 to ensure the current is zero on the edges. The current density function is again expanded with the unknown coefficients, a_n's, n = 1,2…N-1.

Because of the polarization of the incident plane wave, the electric field consists of x and y components obviously, and the current density has only x components on the strip. Therefore, the second term does not vanish in (3.13). For the non-near edge region, the same procedure as in the E-pol case, the conversion is implemented to the real source coordinate to obtain a directional CSP beam. Then, CSP type Green's function is derived and implemented in the EFIE so that it becomes a beam-type radiation. The next step is to apply the Galerkin method with triangular basis functions $t_m(x)$ to generate the following matrix equation:

$$\begin{aligned} \int_{\chi_m-\Delta}^{\chi_m+\Delta} t_m(x) E_x{}^{in}(x)dx = jk\eta \sum_{n=1}^{N-1} a_n \int_{\chi_m-\Delta}^{\chi_m+\Delta} t_m(x) \int_{\chi_n-\Delta}^{\chi_n+\Delta} t_n(x') G_{csp}(x-x', b_n) dx'dx \\ - \frac{j\eta}{k} \sum_{n=1}^{N-1} a_n \int_{\chi_m-\Delta}^{\chi_m+\Delta} \frac{\partial t_m(x)}{\partial x} \int_{\chi_n-\Delta}^{\chi_n+\Delta} \frac{\partial t_n(x')}{\partial x'} G_{csp}(x-x', b_n) dx'dx \end{aligned} \tag{4.37}$$

m=1,2,….N

where $E_x^{in} = \eta \sin\phi^{in} e^{jkx\cos\phi^{in}}$ clearly. Integration by parts was used to obtain the second term of RHS in (4.37). A similar process in the E-pol case, double integrals are reduced to single forms by the change of variables x-x'=u for computational cost and (4.37) becomes as follows:

$$\sin\phi^{in}\int_{\chi_m-\Delta}^{\chi_m+\Delta} t_m(x)e^{jkx\cos\phi^{in}}dx = \frac{k}{4}\sum_{n=1}^{N-1}a_n\int_{v-2\Delta}^{v+2\Delta} H_0^{(2)}(k\sqrt{u^2-b_n^2})z(u)du$$
$$-\frac{1}{4k}\sum_{n=1}^{N-1}a_n\int_{v-2\Delta}^{v+2\Delta} H_0^{(2)}(k\sqrt{u^2-b_n^2})\left[\frac{d^2z(u)}{du^2}\right]du \tag{4.38}$$

where *z(u)* is a convolution function of two triangular functions, which is defined as $z(u)=t_m(u)*t_n(-u)$, and it is described as below:

$$z(u)=\left\{\begin{array}{ll} 1/6\left(\frac{u^3}{\Delta^2}+\frac{6u^2}{\Delta}+12u+8\Delta\right) & -2\Delta\le u<-\Delta \\ 1/6\left(\frac{-3u^3}{\Delta^2}-\frac{6u^2}{\Delta}+4\Delta\right) & -\Delta\le u<0 \\ 1/6\left(\frac{3u^3}{\Delta^2}-\frac{6u^2}{\Delta}+4\Delta\right) & 0\le u<\Delta \\ 1/6\left(\frac{-u^3}{\Delta^2}+\frac{6u^2}{\Delta}-12u+8\Delta\right) & \Delta\le u<2\Delta \end{array}\right\} \tag{4.39}$$

Finally, the main matrix is obtained as follows:

$$Z_{mn}=\frac{k}{4}\int_{v-2\Delta}^{v+2\Delta} H_0^{(2)}(k\sqrt{u^2-b_n^2})z(u)du-\frac{1}{4k}\int_{v-2\Delta}^{v+2\Delta} H_0^{(2)}(k\sqrt{u^2-b_n^2})\left[\frac{d^2z(u)}{du^2}\right]du \tag{4.40}$$

In (4.38), LHS denotes the excitation vector, and it has an integrable solution. Performing this integration yields:

$$g_m=-2\sin\phi^{in}e^{jkx_m\cos\phi^{in}}\left[\frac{\cos(k\Delta\cos\phi^{in})-1}{k^2\Delta\cos^2\phi^{in}}\right] \tag{4.41}$$

Equation (4.40) and (4.41) are matrices for *the MoM Procedure with CSP Type Green's Function* solution of the 2D strip geometry to find the current density for the H-pol case. Like in the E-pol case, they are used for the non-near edge region. Again, it should be noted that they are MoM solution of the 2D strip geometry if $b_n = 0$ for all n values. Therefore, they are also used for near-edge regions in the proposed method by selecting $b_n = 0$.

4.2.2 Determination of the Radiation Characteristics

After the numerical solution of the coefficients *a_n's*, the current density function can be found by using these coefficients. Then the scattering field can be achieved both at the far-field and near-field regions.

4.2.2.1 Far-Field Radiation

The large argument form of Hankel function is needed to obtain the scattered field in the far zone. The far-field approximations for the strip, which are $R \cong r - \vec{r}' \cdot \hat{r}$ in phase term and $R \cong r$ in amplitude term, are used to determine of the far-field radiation. It is used the Hankel function with the large argument in (4.5):

$$\lim_{R \to \infty} H_0^{(2)}(kR) = \sqrt{\frac{2j}{\pi kr}} e^{-jkr} e^{jkx' \cos\phi} \tag{4.42}$$

where ϕ is the angle between the observation point and x-axis. The scattered field in the far zone for E-pol case is written by using this large argument of Hankel function:

$$\begin{aligned} E_z^{sc} &= -\frac{k\eta}{4} \int_L J_z(x') H_0^{(2)}(kR) dx' \\ &= -\sqrt{\frac{2j}{\pi kr}} \cdot e^{-jkr} \underbrace{\left(k\eta / 4\right) \sum_{n=1}^{N} a_n \int_{x_n - \Delta/2}^{x_n + \Delta/2} e^{jkx' \cos\phi} dx'}_{\psi^1(\phi)} \end{aligned} \tag{4.43}$$

where $\psi^1(\phi)$ is the scattering pattern for *the MoM* solution in E-pol case.

After the numerical solution of the matrix equation (4.30), the current density is obtained, which is not the real current density of the original problem. However, the convolution of this current with G_{csp} can then produce the actual scattered pattern. Radiation from the localized Green's function with that pseudo-current function offers a true scattered field under the uniqueness theorem. The far-field approximations for the proposed method are $R_{csp} = r - \vec{r}'_{csp} \cdot \hat{r}$ in phase term and $R_{csp} = r$ in amplitude term. They are substituted in the large argument of the Hankel function using (4.18):

$$\lim_{R_{csp} \to \infty} H_0^{(2)}(kR_{csp}) = \sqrt{\frac{2j}{\pi kr}} e^{-jk(r - x' \cos\phi + jb \sin\phi)} \tag{4.44}$$

Then, the far zone electric field scattered from the strip can be written as:

$$\begin{aligned} E_z^{sc} &= -\frac{k\eta}{4} \int_L J_z(x') H_0^{(2)}(kR_{csp}) dx' \\ &= -\sqrt{\frac{2j}{\pi kr}} \cdot e^{-jkr} \underbrace{\left(k\eta / 4\right) \sum_{n=1}^{N} a_n e^{kb_n \sin\phi} \int_{x_n - \Delta/2}^{x_n + \Delta/2} e^{jkx' \cos\phi} dx'}_{\psi^2(\phi)} \end{aligned} \tag{4.45}$$

where $\psi^2(\phi)$ is the scattering pattern for *the MoM procedure with CSP type Green's function* solution in E-pol case. The bistatic RCS can be given as:

$$\sigma = 2\pi r \frac{\left|E_z^{sc}\right|^2}{\left|E_z^{in}\right|^2} = \frac{4}{k}\left|\psi^u(\phi)\right|^2 \tag{4.46}$$

where $u=1,2$ indicating scattering pattern for the MoM and proposed method in E-pol.

For H-pol case, the scattered field can be represented as vector potential, using (3.10), it forms as below:

$$H_z^{sc} = \frac{1}{\mu}\nabla\times\vec{A}(r) = -\frac{j}{4}(\nabla\times\hat{x})\int_L J_x(x')H_0^{(2)}(kR)dx' \tag{4.47}$$

As mentioned before, the current density has only x components on the strip in the H-pol case. Using the vector identity below, curl operation is reduced to the equation as follows:

$$\begin{aligned}\nabla\times\left(\vec{J}_x(x')H_0^{(2)}(x,y)\right) &= \nabla H_0^{(2)}(x,y)\times\vec{J}_x(x') + H_0^{(2)}(x,y)\left(\nabla\times\vec{J}_x(x')\right)\\ &= \nabla H_0^{(2)}(x,y)\times\vec{J}_x(x')\end{aligned} \tag{4.48}$$

here the second term in the equation goes zero because the current density has only source notation. After the curl operation with the vector identity, the derivation of y component only remains in the equation:

$$\begin{aligned}H_z^{sc} &= -\frac{j}{4}\int_L\left[\frac{\partial\left(H_0^{(2)}(x,y)\right)}{\partial x}(\hat{x}\times\hat{x})\vec{J}_x(x') + \frac{\partial\left(H_0^{(2)}(x,y)\right)}{\partial y}(\hat{y}\times\hat{x})\vec{J}_x(x')\right]dx'\\ &= \frac{j}{4}\int_L\vec{J}_x(x')\frac{\partial}{\partial y}\left(H_0^{(2)}(kR)\right)dx'\end{aligned} \tag{4.49}$$

The derivation of the Hankel function in the large argument form can be written as:

$$\frac{\partial}{\partial y}\left(\sqrt{\frac{2j}{\pi kr}}e^{-jkr}\right) = \sqrt{\frac{2j}{\pi k}}\frac{\sin\phi}{r^{3/2}}e^{-jkr} - \sqrt{\frac{2j}{\pi kr}}jk\sin\phi\cdot e^{-jkr} \tag{4.50}$$

The first term for far-field observation is too small comparing the second one, so it is not considered into the calculation and ignored. Then, the scattering field in the far zone for H-pol case is written as follows:

$$H_z^{sc} = -\sqrt{\frac{2j}{\pi kr}}e^{-jkr}\underbrace{(k/4)\sin\phi\sum_{n=1}^{N-1}a_n\int_{\chi_n-\Delta}^{\chi_n+\Delta}t_n(x')e^{jkx'\cos\phi}dx'}_{\psi^3(\phi)} \tag{4.51}$$

where $\psi^3(\phi)$ is the scattering pattern for *the MoM* solution in H-pol case.

Similarly, after the numerical solution of the H-polarization matrix equation for the proposed method and by using the large argument of the Hankel function (equation (4.44)), the far zone scattered magnetic field can be written as:

$$H_z^{sc} = -\sqrt{\frac{2j}{\pi kr}} e^{-jkr} \underbrace{(k/4)\sin\phi \sum_{n=1}^{N-1} a_n e^{kb_n \sin\phi} \int_{\chi_n-\Delta}^{\chi_n+\Delta} t_n(x') e^{jkx'\cos\phi} dx'}_{\psi^4(\phi)} \tag{4.52}$$

where $\psi^4(\phi)$ is the scattering pattern for *the MoM procedure with CSP type Green's function* solution in H-pol case. In the last two equations, the integral has an analytical solution, and reduces the computational cost for PC, it is found to be:

$$\int_{\chi_n-\Delta}^{\chi_n+\Delta} t_n(x') e^{jkx'\cos\phi} dx' = -2\frac{e^{jkx_n\cos\phi}}{\Delta k^2 \cos^2\phi}\left(\cos(\Delta k\cos\phi) - 1\right) \tag{4.53}$$

The bistatic RCS is given by:

$$\sigma = 2\pi r \frac{\left|H_z^{sc}\right|^2}{\left|H_z^{in}\right|^2} = \frac{4}{k}\left|\psi^p(\phi)\right|^2 \tag{4.54}$$

where *p=3,4* indicating scattering pattern for MoM and proposed method in H-pol.

4.2.2.2 Near-Field Radiation

Because the observation point is near the strip surface, the large argument form of the Hankel function is not needed to find the scattered field in the near zone. The following equation is used to compute the near-field scattering for E-pol case:

$$\begin{aligned} E_z^{sc} &= -\frac{k\eta}{4}\int_L J_z(x') H_0^{(2)}(kR) dx' \\ &= -\frac{k\eta}{4}\sum_{n=1}^{N} a_n \int_{x_n-\Delta/2}^{x_n+\Delta/2} H_0^{(2)}(k\sqrt{(x-x')^2 + (y)^2}) dx' \end{aligned} \tag{4.55}$$

where $x = r\cos\phi$ and $y = r\sin\phi$ in order to define the near field distance.

For the proposed method, simply interchanging $R \to R_{csp}$ in the Hankel function and near-field scattering is derived for E-pol case as below:

$$\begin{aligned} E_z^{sc} &= -\frac{k\eta}{4}\int_L J_z(x') H_0^{(2)}(kR_{csp}) dx' \\ &= -\frac{k\eta}{4}\sum_{n=1}^{N} a_n \int_{x_n-\Delta/2}^{x_n+\Delta/2} H_0^{(2)}(k\sqrt{(x-x')^2 + (y+jb)^2}) dx' \end{aligned} \tag{4.56}$$

For H-pol case, to find the derivation of y component in (4.49), the derivation of the Hankel function is needed to use:

$$\frac{\partial}{\partial R}\left(H_0^{(2)}(kR)\right)=-kH_1^{(2)}(kR) \tag{4.57}$$

Then, it is derived for y component by using the chain rule of derivation:

$$\frac{\partial}{\partial y}\left(H_0^{(2)}(kR)\right)=\frac{\partial}{\partial R}\left(H_0^{(2)}(kR)\right)\cdot\frac{\partial R}{\partial y}=\frac{-k}{R}(y-y')H_1^{(2)}(kR) \tag{4.58}$$

Since $y'=0$ on the strip, equation (4.49) is described for near-field radiation by substituting the derivation of the Hankel function as follows:

$$H_z^{sc}=-\frac{jkr\sin\phi}{4}\sum_{n=1}^{N-1}a_n\int_{\chi_n-\Delta}^{\chi_n+\Delta}H_1^{(2)}(kR)\frac{t_n(x')}{R}dx' \tag{4.59}$$

For the proposed method, similarly in E-pol case, $R\to R_{csp}$ is substituted in the Hankel function and the derivation is now obtained:

$$\frac{\partial}{\partial y}\left(H_0^{(2)}(kR_{csp})\right)=\frac{\partial}{\partial R_{csp}}\left(H_0^{(2)}(kR_{csp})\right)\cdot\frac{\partial R_{csp}}{\partial y}=\frac{-k}{R_{csp}}(y+jb)H_1^{(2)}(kR_{csp}) \tag{4.60}$$

Then, near-field scattering is found for H-pol case as below:

$$H_z^{sc}=\left(\frac{-jkr\sin\phi+kb}{4}\right)\sum_{n=1}^{N-1}a_n\int_{\chi_n-\Delta}^{\chi_n+\Delta}H_1^{(2)}(kR_{csp})\frac{t_n(x')}{R_{csp}}dx' \tag{4.61}$$

4.2.3 Main Concept of the Method and Determination of the Parameters 'b' and 'α'

This key point of the hybrid method presented has been elaborated, as explained in (Kutluay & Oğuzer, 2019):

The CSP field is a beam in free space, and it is the exact solution of the Helmholtz Equation, additionally satisfying the radiation condition. The BC on the PEC strip was used in the formulation of the problem. In the vicinity of the edge, the free-space Green's function was adjusted by setting the parameter *b* as zero to keep the EC intact. The distance parameter α is as large as possible to prevent the radiation of the surface current on the edges.

The rough view of the main matrix filled with numbers is a pattern in Figure 4.5a and Figure 4.5b for L = 10λ. The standard MoM in the E-pol case produces a dense matrix (see Figure 4.5a), but as shown in Figure 4.5b, with our technique, the main impedance matrix is converted to a sparse form indicated by white parts in the mapping as almost zero magnitudes.

In the H-pol case, two integrals of the main matrix were studied standing in the right-hand part of equation (4.37). The main impedance matrix is converted to a sparse form just like in E-pol, and the patterns of the main matrix elements are shown in Figure 4.5c and Figure 4.5d. Due to these remarkable features, the proposed hybrid technique provides an important advantage in computer storage and calculation time.

CSP Green's function (G_{csp}) tends to zero in the region of $|x| \geq 1$, as shown in Figure 4.2. The function has a numerical value only in the region of $|x| < 1$; however, it is almost zero if $|x| \geq 1$. Therefore, it should be selected b ≥ 1, and it is expected that "α" should be equal or greater than "b" so that the near edge region is not illuminated by complex source radiation of the basis functions on the strip surface. Due to this selection, the edges do not enter the beam apertures on the scatterer surface, and the EC is unaltered and preserved.

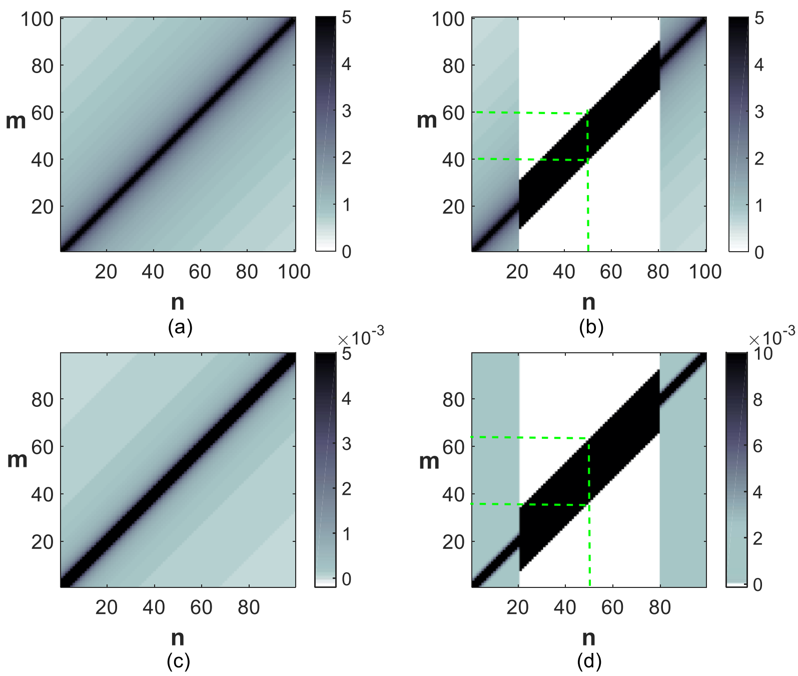

Figure 4.5 The magnitude level of the impedance matrix elements for L = 10λ, Δ = 0.1λ (a) standard MoM and (b) the proposed method for E-pol with α = 2λ and b = 1λ, (c) standard MoM, and (d) the proposed method for H-pol with α = 2λ and b = 1.3λ (Green dashed lines marked for explanation)

Then, the main matrix elements are used to find the radiated electric field as an explanation of the interactions. For n = 1, the matrix column Z_{m1} is linked to the interval between "m" and "1". This interval does not depend on the location of the basis function because the Toeplitz matrix has a hierarchy of shift-invariant. Here, what is important is the difference between "m" and "1", which describes the distance between the source location and the testing location. This column matrix indicating the radiated electric field, presents a reduction with the distance away from the source. Therefore, the basis function (as indicated, n = 1) can be selected for any source location in the non-near edge region where $b \neq 0$. The goal is to observe the behavior of the complex source beam radiation in the non-near edge region. Hence, called Z_{ms}, where "s" is a static index (basis function index only for CSP in the non-near-edge region) indicating the CSP location, and "m" is a non-static index number (testing function index) that indicates the location of testing function; it varies from 1 to N in E-pol and N-1 in H-pol. For any CSP in the non-near edge region, it means whatever "s" is assigned, the behavior of the CSP beam radiation is identical for any specific "b". Accordingly, the index "s" is assigned to any CSP location, and the matrix Z_{ms} degraded to $Q_{|m-s|}$ in order to observe just one CSP. In brief, $Q_{|m-s|}$ is the testing vector of any CSP in the non-near edge region, that is, it is a column matrix of Z_{ms} corresponding to any number of "s". For instance, in Figure 4.5b and Figure 4.5d, since $\alpha = 2\lambda$, "s" index varies from 20 to 80 for the case of the total number of unknown N = 100 and $\Delta = 0.1\lambda$. In this case, the main matrix is not a good sparse matrix; the parameters α, b, L have been specified so that the figure is easily visible, and the band structure shows non-zero matrix elements. $Q_{|m-s|}$ column matrices shape the band structure in that region, for example, in Figure 4.5b, if the "s" or "n" index is 50, since $b = 1\lambda$, the "m" index takes any value from 40 to 60, and these values indicate two identical column vectors. Each side is symmetrical and has a pattern like G_{csp} in terms of magnitude (see Figure 4.2). In this column matrix, the maximum value for each side is at m = 50, and minimum values are at m = 40 and m = 60 for this example. For the sake of simplicity, we viewed one side $|Q_{|m-s|}|$ as shown in Figure 4.6. As stated above, $Q_{|m-s|}$ column matrices are identical for any index number of "s" in the band structure, so $|Q_{|m-s|}|$ was investigated independently from the "s" index.

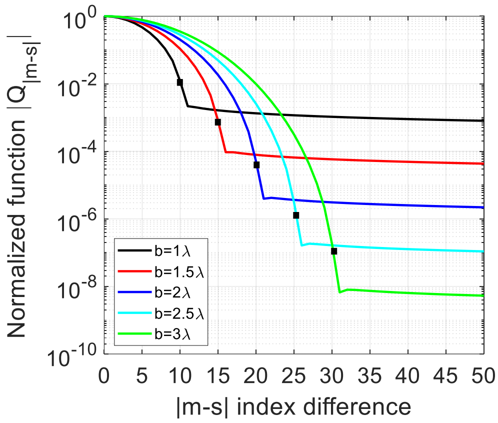

(a)

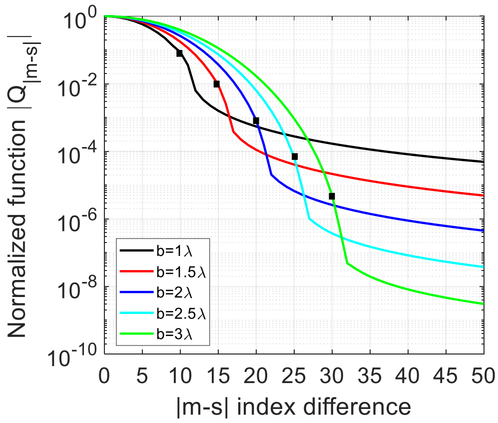

(b)

Figure 4.6 Normalised function $|Q_{|m-s|}|$ versus $x/\lambda\Delta$ at $x' = 0$ (a) E-polarisation, (b) H-polarisation

We implemented the approximation $Z_{ms} = 0$ for the regions where "|*m-s*|" distance is greater than "*b*" as shown in Figure 4.5b and Figure 4.5d. Therefore, analyzing the normalized function $|Q_{|m-s|}|$ versus the "|*m-s*|" index difference is a worthy intention. The parts where "|*m-s*|" distance is greater than "*b*" provide an insight into the approximation. These concepts depending on Z_{mn} can be applied to the other 2D geometries such as PEC cylinders in section 4.3 for the determination of α and b.

Resulting $|Q_{|m-s|}|$ varies depending on the polarisation, as shown for E-pol and H-pol in Figure 4.6a and Figure 4.6b. A descending pattern of $|Q_{|m-s|}|$ in H-pol was observed more widely compared to the E-pol. Also, the decrease of $|Q_{|m-s|}|$ is smaller in H-pol than in E-pol for any value of "*b*". Thus, selecting larger "*b*" in H-pol is a necessity so that the approximated parts are closer to zero.

Typically, $b = 1\lambda$ can be assigned for both polarisations whose relative errors are less than one percent, as shown in the numerical results. However, for more accurate results, $b > 1\lambda$ can be assigned. There is a little trade-off, because the selection of "*b*" affects the computing and filling the main matrix, hence the computational time. Taking a larger value of "*b*" means decreasing the sparsity of the main matrix. Experiments show that $|Q_{|m-s|}|$ at "|m-s|" should be less than 10^{-3}, corresponding to $b = 1.5\lambda$ and $b = 2\lambda$ for E-pol and H-pol, respectively.

It is not important to select “α” in the scale of larger values than “b”, and $\alpha \geq b$ can be assigned. Nonetheless, larger “α” values ensure the correction in the minor lobes, especially in the angles close to 0^o and 180^o in RCS. These corrections are not significant compared to the main lobe since they are negative in the dB scale of RCS. In the light of the findings described above, at the normal incidence, b = 1.5λ and α = 2.5λ were assigned in E-pol, b = 2λ and α = 3λ in H-pol, to properly represent the method. At the inclined incidence, since the edges are less effected by the radiation of CSP and the edges are more critical, the near edge regions must be wider. Namely, “α” is assigned larger values, for example, b = 1.5λ and α = 4λ were assigned for E-pol, b = 2λ, and α = 4λ for H-pol at the inclined incidence, $\phi^{in} = 30^o$. Taking a larger value of α extends the near edge regions so that the method is more dominant at the grazing incidence illumination.

4.2.4 Numerical Results

It has been computed some numerical data to verify the working performance of the presented approach for PEC strip geometry in both polarisations. The proposed procedure has been followed, as introduced in Section 4.2.1, to achieve numerical results.

The current density functions have been obtained by using optimum iterative sparse solvers in MATLAB. In Figure 7, the real surface current density and the current density function obtained from the proposed procedure (b=1λ) are shown on the same plot for both polarisations. As expected, the edge effects look similar to the free-space Green’s function case because we set it free in the regions near the edges. In other words, it is implemented the free-space Green’s function for the radiation from the basis functions near the edges. The near edge behavior of the surface current distribution is similar to the original solution of the problem. Also, in the middle region, the radiation of the basis functions with the modified Green’s function does not affect the edge points, and so EC is not effected.

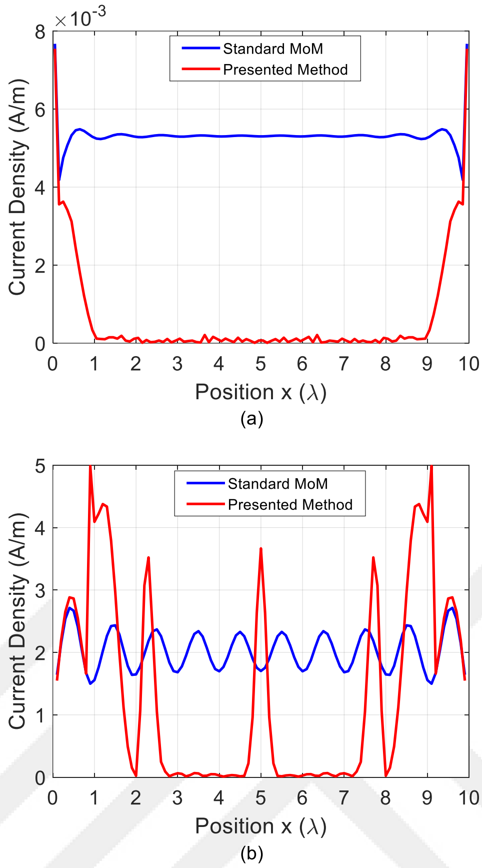

Figure 4.7 The blue line is the real current density obtained from the standard MoM, the red line is the pseudo-current function from the proposed method for the PEC 2-D strip of width L = 10λ and $\phi^{in} = 90^o$, and b=1λ (a) E-pol and (b) H-pol

We also computed the relative error (RE) of RCS computations, defined as:

$$\bar{\varepsilon} = \sqrt{\sum_{n=1}^{N} \left| e^{mom} - e^{csp} \right|^2} \cdot \left(\sqrt{\sum_{n=1}^{N} \left| e^{mom} \right|^2} \right)^{-1} \tag{4.62}$$

Here, e^{mom} is the solution obtained using the standard MoM, and e^{csp} is the solution obtained by the proposed method. In the above equation, the total discretization number is changed to N-1 for H-pol cases.

In Figure 4.8, the bistatic RCS is demonstrated for both polarisations and $L = 50\lambda$ strip width. Although the strip width is large, the RCS obtained is very similar to the standard MoM, with a RE of 0.18% for E-pol case and 0.09% for H-pol. Even though the condition number of the main sparse matrix for $L = 50\lambda$ is approximately 10^6, the RE is low. This low error tolerance is obtained by using the iterative algorithms for sparse matrix equation solvers in MATLAB. A slight deviation occurs in the directions parallel to the strip, but these regions are trivial compared to the scale of dB magnitudes.

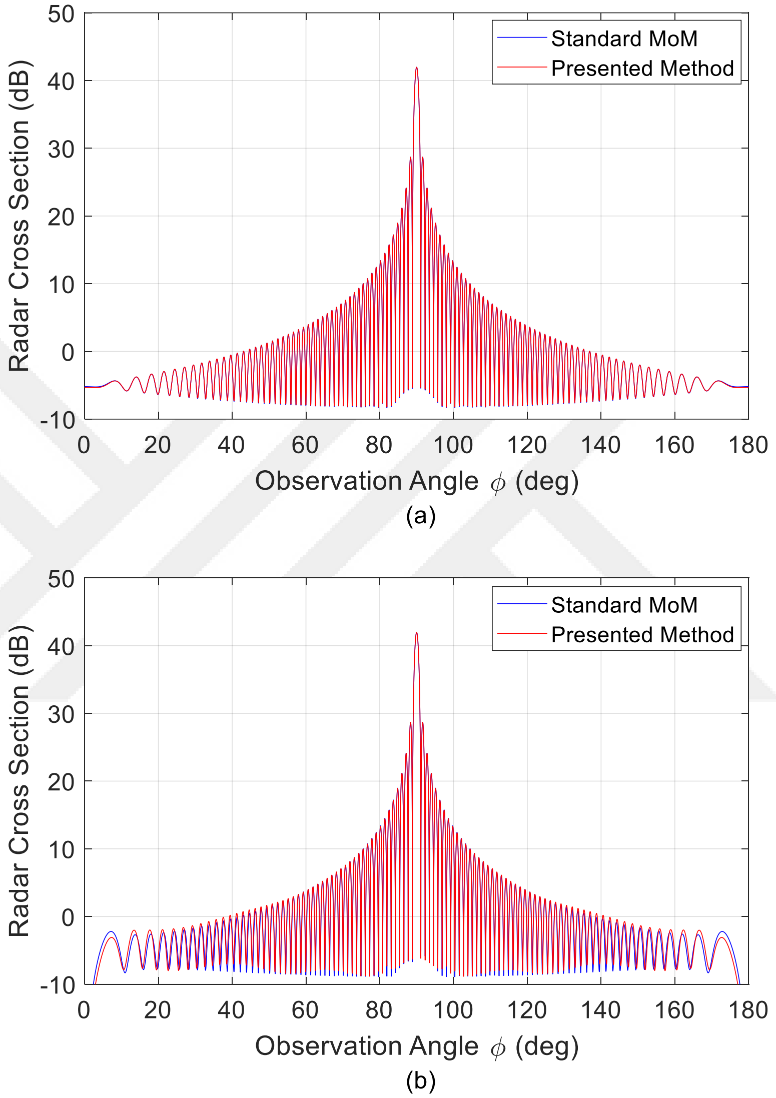

Figure 4.8 RCS pattern comparison between standard MoM and the proposed method for L = 50λ and ϕ^{in} = 90°, (a) E-pol: b = 1.5λ, α = 2.5λ and RE = 0.18% and (b) H-pol: b = 2λ, α = 3λ and RE = 0.09%

After verification for the normal incidence, the scattering was examined near the grazing incidence angle ϕ^{in} = 30°, which produced good results as shown in Figure 4.9. Here, larger values of α have been chosen for the near grazing incidence for more accurate results at the observation angles close to 0° and 180° in the RCS analysis.

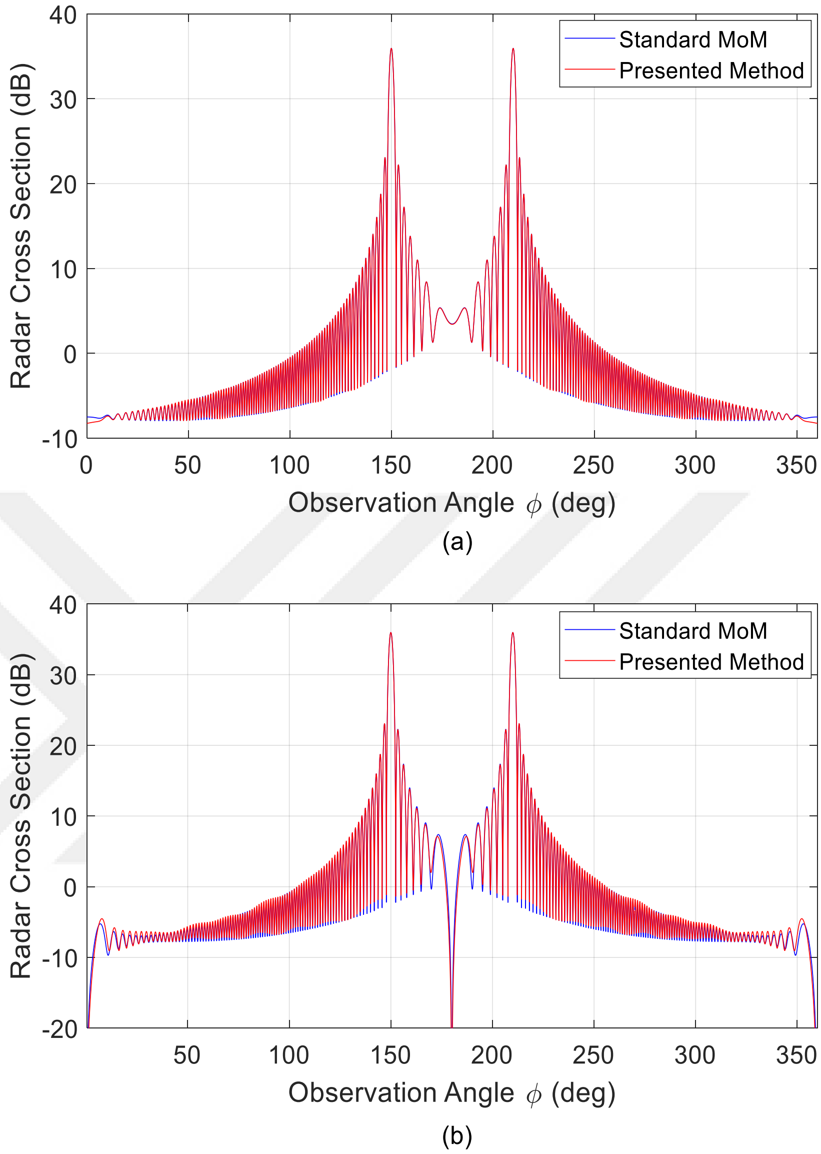

Figure 4.9 RCS pattern comparison for the inclined incidence between the standard MoM and the proposed method for L = 50λ (a) E-pol: ϕ^{in} = 30º, b = 1.5λ, α = 4λ and RE = 0.08% and (b) H-pol: ϕ^{in} = 30º, b = 2λ, α = 4λ and RE = 0.15%

The RCS data was also computed for the near-zone region of flat strip by putting (4.55), (4.56) into (3.2) for E-pol, and (4.59), (4.61) into the its identical form for H-pol. Comparing the standard MoM procedure with CSP type Green's function method for L = 20λ and ϕ^{in} = 90º is shown in Figure 4.10. By taking r = 15λ to get closer to the boundaries, the RCS function near the strip is plotted and compared with the standard MoM. As expected, the results are in agreement with the standard MoM. It is considered all conditions of the EM formulation; as a result, the computed field values are correct, even when close to the strip.

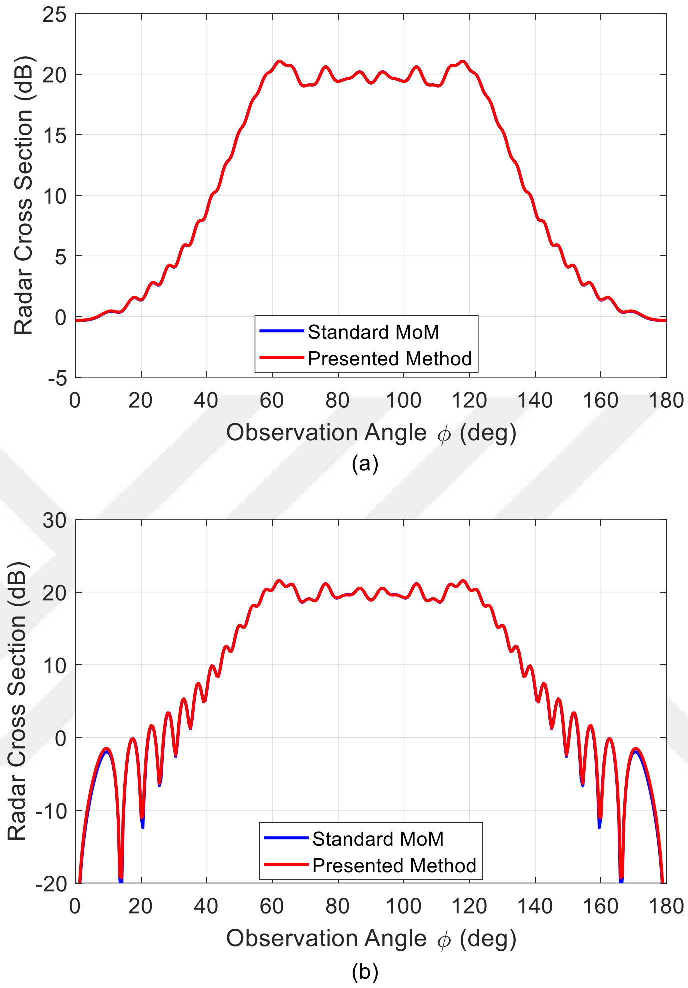

Figure 4.10 Near-field RCS pattern comparison between the standard MoM and the proposed method for L = 20λ and ϕ^{in} = 90º (a) E-pol: r = 15λ, RE = 0.2%, b = 1.5λ and α = 2.5λ and (b) H-pol: r = 15λ, RE = 0.39%, b =2λ and α=3λ

Finally, the RE plots are demonstrated in Figure 4.11 for the strip geometry to analyze the choice of the parameters α and b. The strip width has been fixed as L = 50λ for both polarisations, and the REs in RCS for the incidence angles 90º and 30º have been investigated. If the EC is fulfilled by setting the parameter α, in other words, $\alpha \geq b$, the RE reduces. The RE plots support the choice of α and b, as explained in section 4.2.3.

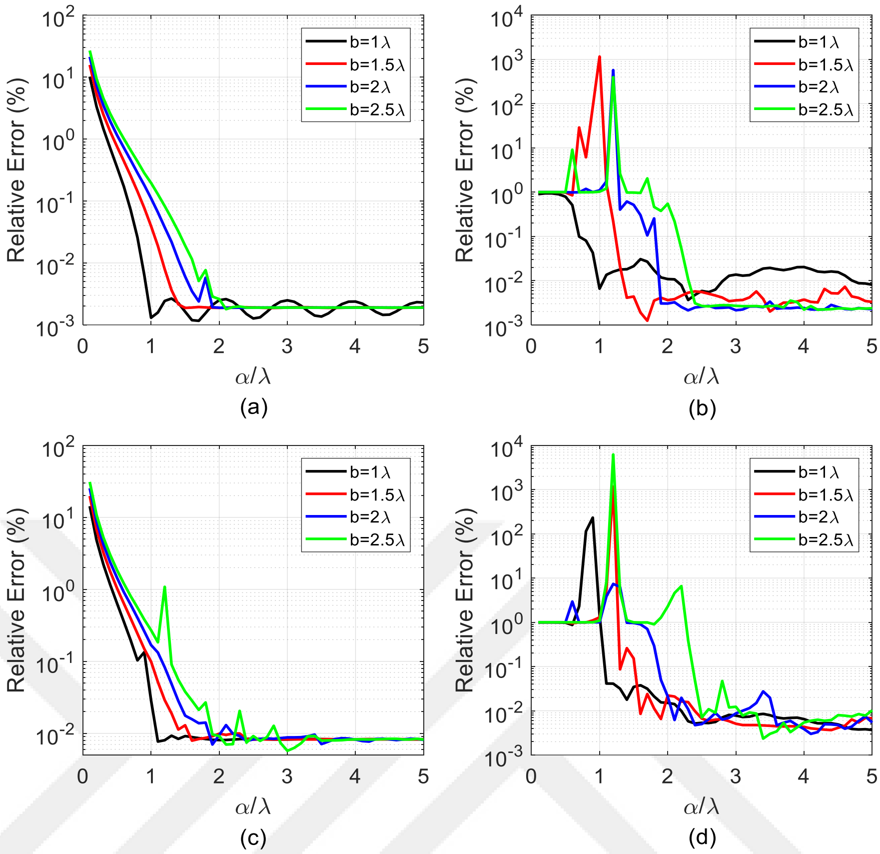

Figure 4.11 RE plots for the strip geometry L = 50λ (a) E-pol $\phi^{in} = 90^o$, (b) E-pol $\phi^{in} = 30^o$, (c) H-pol $\phi^{in} = 90^o$ and (d) H-pol $\phi^{in} = 30^o$

It is also pointed out the memory storage requirements for all strip sizes in Table 4.1 and Table 4.2 if the λ/10 discretization criterion follows it. It should be noted that there has not been a noticeable difference in accuracy for the results if the discretization criteria are set to smaller ones. In Table 4.1, it is chosen b = 1.5λ, α = 2.5λ for all strip lengths for E-pol, and b = 2λ, α = 3λ for H-pol in Table 4.2. Memory storage is an important parameter to verify the efficiency of the proposed method. Required memory storage of the computer is defined by the number of elements of the main impedance matrix. The number of the main matrix elements has been calculated using (3.16), in which the beam waist γ of the localized Green's Function is substituted by the coefficient b for the proposed method.

Another main criterion is related to the overall running times. Table 4.1 and Table 4.2 also show the overall CPU time during the analysis to obtain the current density functions for the MoM and for proposed method. RCS evaluation time is excluded from the overall CPU time. As mentioned before, the Toeplitz type matrix structure appears in the 2D strip problems and reduces filling elements of the main matrix. Therefore, for the MoM and presented method, the Toeplitz property improves the overall running times in the strip geometry solution. REs have been computed 0.18% in the E-pol and 0.89% in the H-pol for all the strip size up to 3000λ. Although the memory usage for the available desktop computer is limited to solve the problem by the standard MoM for 3000λ strip size, the presented method is eligible to analyze for the strip size of 50000λ with remarkable solution time.

Figure 4.12 shows the overall running CPU times of the computation with the MoM and presented method according to the total number of unknown N. Due to the sparse form of the main matrix, the overall CPU time reduces drastically, especially for large strip widths. If the strip size is L = 500λ, N becomes 5000 if we follow the λ/10 discretization criterion. Then in the standard MoM, the main impedance matrix size becomes 5000 x 5000. Alternatively, the main matrix size obtained in the proposed method is approximately 80 x 5000 for α = 2.5λ and b = 1.5λ in E-pol and the normal incidence angle. The matrix size in H-pol for the normal incidence angle is 100 x 5000 for α = 3λ and b = 2λ. Briefly, it has been a substantial gain in memory storage and operation count for both polarizations. The memory requirement in the usual MoM is O(N^2), while it is about O(80 x N) for E-pol and O(100 x N) for H-pol in the proposed method for the single PEC strip geometry. If the size of the problem increases, then the required memory storage sharply increases when using the MoM. Significant improvements can be obtained in the light of this, especially for very large problem dimensions. Figure 4.12 shows the time difference between polarizations for the presented method in consequence of the different parameters “α” and “b”.

Table 4.1 CPU time and memory storage comparison for PEC strip geometry (E-Pol)

Strip Length (λ)	**Incident angle (degree)**	**Solution Time For E-pol (seconds)**		**Memory Storage**		***Relative Error (%)***
		MoM	***Presented method***	***MoM (N x N)***	***Presented method (80N)***	
L=500	90	4	1	$25{\cdot}10^6$	$0.4{\cdot}10^6$	0.18
L=1000	90	25	2	$100{\cdot}10^6$	$0.8{\cdot}10^6$	0.18
L=2000	90	182	3	$400{\cdot}10^6$	$1.6{\cdot}10^6$	0.18
L=3000	90	661	5	$900{\cdot}10^6$	$2.4{\cdot}10^6$	0.18
L=5000	90	-	9	$2.5{\cdot}10^9$	$4{\cdot}10^6$	-
L=10000	90	-	18	$1{\cdot}10^{10}$	$8{\cdot}10^6$	-
L=50000	90	-	92	$2.5{\cdot}10^{11}$	$40{\cdot}10^6$	-

Table 4.2 CPU time and memory storage comparison for PEC strip geometry (H-Pol)

Strip Length (λ)	**Incident angle (degree)**	**Solution Time For H-pol (seconds)**		**Memory Storage**		***Relative Error (%)***
		MoM	***Presented method***	***MoM (N x N)***	***Presented method (100N)***	
L=500	90	4	1	$25{\cdot}10^6$	$0.5{\cdot}10^6$	0.89
L=1000	90	24	2	$100{\cdot}10^6$	$1{\cdot}10^6$	0.89
L=2000	90	181	4	$400{\cdot}10^6$	$2{\cdot}10^6$	0.89
L=3000	90	638	6	$900{\cdot}10^6$	$3{\cdot}10^6$	0.89
L=5000	90	-	10	$2.5{\cdot}10^9$	$5{\cdot}10^6$	-
L=10000	90	-	21	$1{\cdot}10^{10}$	$10{\cdot}10^6$	-
L=50000	90	-	113	$2.5{\cdot}10^{11}$	$50{\cdot}10^6$	-

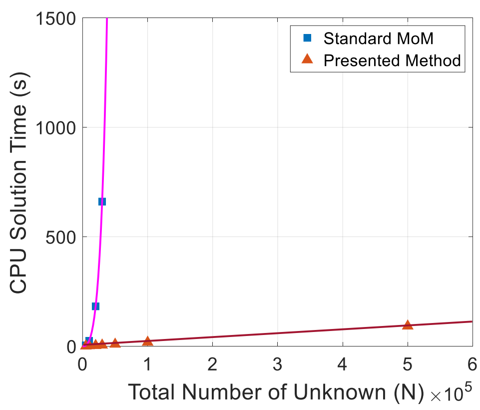

(a)

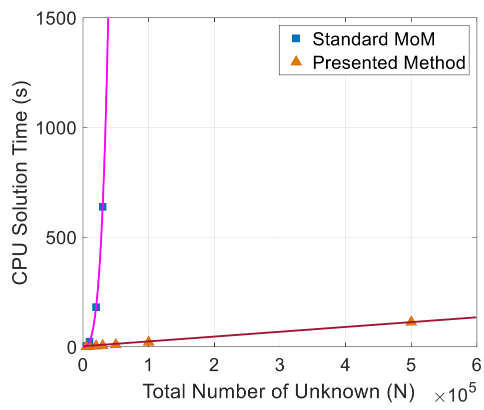

(b)

Figure 4.12 The overall running CPU times of the computation versus the total number of the unknown for strip geometry (a) E-pol and (b) H-pol

The difference in the CPU time becomes more attractive if the strip width gets larger. Beyond the total number of the unknown of 30000 (L = 3000λ), our desktop PC does not give any results as its capacity is not enough to solve the problem with MoM, whereas the presented method can be used.

For larger strip sizes than 3000λ, the proposed method has been compared with the UTD solution to put forward an acceptable result. Figure 4.13 proves the comparison in both polarizations between the proposed method and the UTD solution for L = 5000λ. Results are in good harmony with the RE 0.03% for E-pol and RE 0.97% for H-pol.

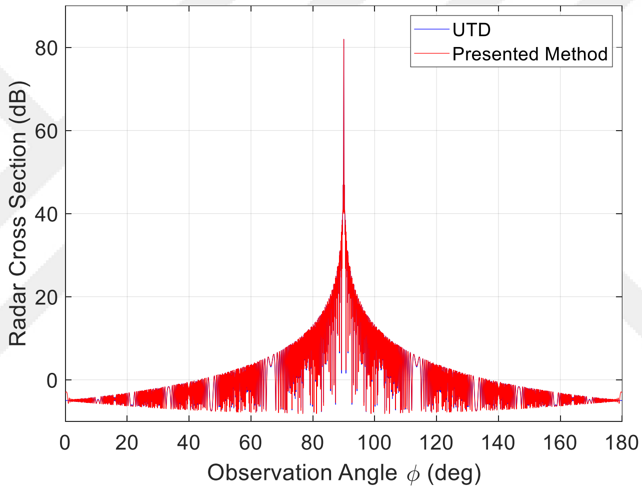

(a) E-pol case, b = 2.5λ, α = 5λ and RE = 0.03%

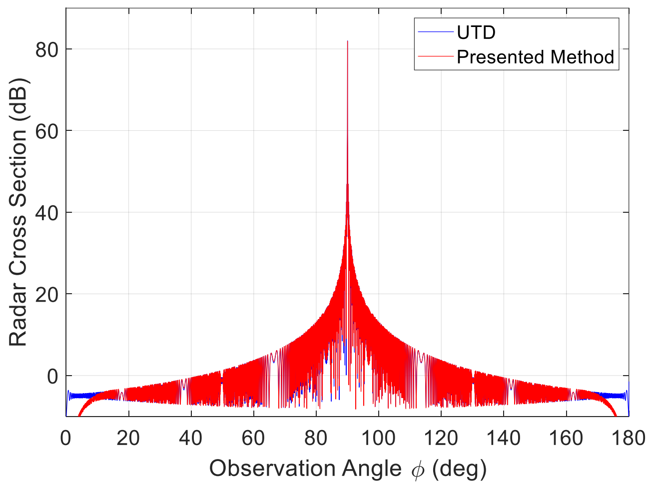

(b) H-pol case, b = 2.5λ, α = 5λ and RE = 0.97%

Figure 4.13 RCS pattern comparison between UTD solution and the proposed method for L = 5000λ, $\phi^{in} = 90^o$

4.3 2D Scattering from A Large PEC Polygon Cylinder with N-Sided Convex Cross-Section

After analyzing the strip geometry, more complex geometry is considered in this section to examine the proposed method.

4.3.1 MoM Procedure with CSP Type Green's Function

The geometry is a PEC polygonal cylinder with N-sided convex cross-section, as shown in Figure 4.14, illuminated by an EM plane wave of one of two polarizations.

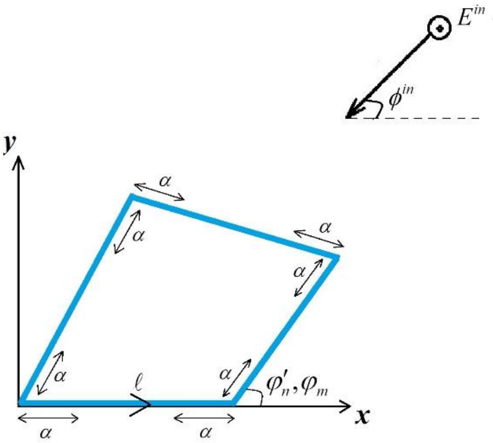

Figure 4.14 Four-sided polygon cross-sectional 2D PEC cylinder geometry

4.3.1.1 E-polarization

The same procedure in the strip geometry is followed with equation (4.1a), and the complex beam vector is defined as below:

$$\vec{b} = \hat{x}b\sin(\varphi) - \hat{y}b\cos(\varphi) \qquad (4.63)$$

where φ is the angle between the edge and the *x*-axis, and beam vector $\vec{b}$ is directed outward from the structure for all facets. As explained in the strip section, the second term vanishes in (3.13) due to the geometry, then, the EFIE can be presented as:

$$E_z^{inc} = jk\eta\int_{Ct} J_z^{csp}(\vec{r}')G_{csp}(\vec{r}-\vec{r}', b(\vec{r}'))d\ell' \qquad (4.64)$$

In order to find CSP type Green's function in parallel to (4.14), $\vec{r}'_{csp}$ is derived as below with the complex beam vector defined in (4.63):

$$\vec{r}' \to \vec{r}'_{csp} = \vec{r}' - j\vec{b} = \hat{x}(x' - jb\sin(\varphi')) + \hat{y}(y' + jb\cos(\varphi')) \quad (4.65)$$

Using (4.65), CSP type Green's function is formed as below:

$$G_{csp}(\vec{r}-\vec{r}', b(\vec{r}')) = -\frac{j}{4}H_0^{(2)}(k\sqrt{(x-x'+jb(r')\sin(\varphi'))^2 + (y-y'-jb(r')\cos(\varphi'))^2} \quad (4.66)$$

Here, $b(\vec{r}')$ is the beam parameter in parallel to (4.25):

$$b(r') = \begin{cases} 0, & near\ edges \\ b, & non-near\ edges \end{cases} \quad (4.67)$$

If considering only for the non-near edge regions, expressions in the Hankel function are written as follows:

$$(x-x'+jb\sin(\varphi'))^2 = (x-x')^2 + (jb\sin(\varphi'))^2 + 2(x-x')jb\sin(\varphi') \quad (4.68a)$$
$$(y-y'-jb\cos(\varphi'))^2 = (y-y')^2 + (jb\cos(\varphi'))^2 - 2(y-y')jb\cos(\varphi') \quad (4.68b)$$

Summation of the last two terms in 4.68(a) and 4.68(b) yields:

$$\begin{aligned} & 2(x-x')jb\sin(\varphi') - 2(y-y')jb\cos(\varphi') \\ & = 2jb\sin(\varphi') - 2\tan(\varphi')jb\cos(\varphi') \\ & = 0 \end{aligned} \quad (4.69)$$

based on $(y-y')/(x-x') = \tan(\varphi')$ because the source point and testing point are in the same facet. In the case of $b \neq 0$, it should be noted that the beam type radiation of the basis functions interacts with the testing points only on the same facet because the beam radiates outward from the facet. Then, the CSP type Green's function for this geometry is found as:

$$G_{csp}(\vec{r}-\vec{r}', b(\vec{r}')) = -\frac{j}{4}H_0^{(2)}(k\sqrt{(x-x')^2 + (y-y')^2 - b(r')^2} \quad (4.70)$$

Afterward, applying Galerkin's procedure with pulse basis functions, the following matrix equation can be found for the E-pol case:

$$\int_0^{\Delta_m} p_m(\ell)E_z^{in}(\ell)d\ell = jk\eta\sum_{n=1}^{N} a_n \int_0^{\Delta_m} p_m(\ell)\int_0^{\Delta_n} p_n(\ell')G_{csp}(\tilde{x}_m - \tilde{x}'_n, \tilde{y}_m - \tilde{y}'_n, b_n)d\ell' d\ell \quad (4.71)$$

m=1,2,….N

where $E_z^{in}(\ell) = e^{jk(\tilde{x}\cos\phi^{in} + \tilde{y}\sin\phi^{in})}$ and the rectangular coordinate parameters are defined as below:

$$(\tilde{x}_m, \tilde{y}_m) = (x_{ms} + \ell\cos(\varphi_m), y_{ms} + \ell\sin(\varphi_m)) \quad (4.72a)$$

$$(\tilde{x}'_n, \tilde{y}'_n) = (x'_{ns} + \ell'\cos(\varphi'_n), y'_{ns} + \ell'\sin(\varphi'_n)) \quad (4.72b)$$

This is a coordinate transformation from (x,y) to (ℓ, φ), x_{ms} and y_{ms} are the initial coordinates of the m'th pulse testing function, ℓ is the distance measured along the path in the used coordinates as visible in Figure 4.15a. Then, the integral limits are adjusted according to these coordinates along the contour. For the basis functions, the format is the same for the initial coordinates with n'th pulse basis function. Similar to the strip scattering, b_n is the complex beam parameter, it is selected $b_n = 0$ in the near edge regions and a real constant value in the non-near edge region, $b_n = b$. In matrix form, the main matrix and excitation vector can now be written as follows:

$$Z_{mn} = \frac{k\eta}{4}\sum_{n=1}^{N} a_n \int_0^{\Delta_m}\int_0^{\Delta_n} H_0^{(2)}\left(k\sqrt{(\tilde{x}_m - \tilde{x}_n')^2 + (\tilde{y}_m - \tilde{y}_n')^2 - b_n^{\,2}}\right) d\ell' d\ell \tag{4.73}$$

$$g_m = \int_0^{\Delta_m} e^{jk(\tilde{x}_m \cos\phi^{in} + \tilde{y}_m \sin\phi^{in})} d\ell \tag{4.74}$$

It should be reminded that equation (4.73) can be reduced to the main matrix definition for the MoM solution by assigning $b_n = 0$ for all n values.

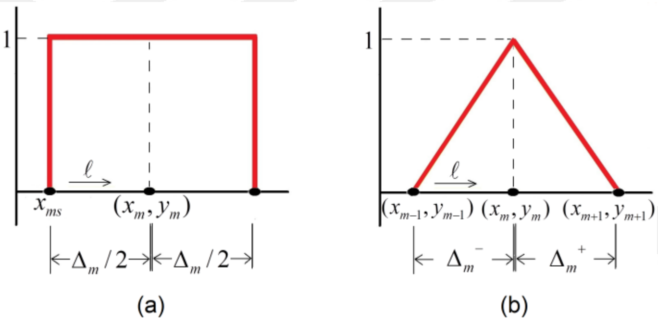

Figure 4.15 Testing functions (a) pulse function for E-pol and (b) triangular function for H-pol

4.3.1.2 H-polarization

In H-pol, assuming a magnetic field with $\vec{H}_z^{in}$ is illuminated the cylinder instead of $\vec{E}_z^{in}$ in Figure 4.14, and it is applied with the triangular basis functions as depicted in Figure 4.15b. The triangular basis functions are defined as:

$$t_m(\ell) = \begin{cases} \dfrac{\ell}{\Delta_m^{\,-}}, & \textit{in left segment} \\[2ex] \dfrac{\Delta_m^{\,+} - \ell}{\Delta_m^{\,+}}, & \textit{in right segment} \\[2ex] 0, & \textit{elsewhere} \end{cases} \tag{4.75}$$

In order to define the CSP type Green's function, a similar coordinate transformation is again described below:

$$(\bar{x}_m, \bar{y}_m) = (x_{m-1} + \ell\cos(\varphi_m^-), y_{m-1} + \ell\sin(\varphi_m^-)) \tag{4.76a}$$

$$(\bar{x}_m, \bar{y}_m) = (x_m + \ell\cos(\varphi_m^+), y_m + \ell\sin(\varphi_m^+)) \tag{4.76b}$$

where equation (4.76a) is for the left segment of the triangular testing function and equation (4.76b) for the right segment of the triangular testing function. Also, x_{m-1}, y_{m-1}, x_m, y_m are some related coordinates shown in Figure 4.15b, φ_m^- and φ_m^+ are the angles between the edge and the *x*-axis for the left segment and the right segment of the related testing function on a facet. Note that φ_m^- and φ_m^+ are different, if and only if, the testing function is on the corner of the structure. In this case, the delta distance is also different in each segment. Hence, Δ_m^- and Δ_m^+ are defined as delta distance for the left segment and the right segment of the triangular testing function, respectively. For the source basis functions, the format is the same for all representations above.

The complex beam vector in (4.63) is also utilized for the H-pol case. The derivation of the CSP type Green's function is obtained through equations from (4.65) to (4.70). When obtaining equation (4.69), equality $(y-y')/(x-x') = \tan(\varphi')$ is not correct for the basis or testing triangular functions at the corner of the structure. If the source point is at the corner of the structure, it is in the near-edge region and applied MoM procedure, which is $b = 0$, and equation (4.69) is verified straightforward. If the source point is in the non-near edge region, since α should be equal or greater than b, as explained in section 4.2.3, complex source radiation does not interact with the testing function on the corner of the structure. In other saying, the equality $(y-y')/(x-x') = \tan(\varphi')$ remains valid for the source points in the non-near edge region, and equation (4.70) is obtained for the H-pol case.

As explained in the strip section for H-pol, the second term does not vanish in (3.13). For the implementation of BC and utilizing the tangential electric field, scalar multiplication with $\hat{\ell}$ is applied to the equation, and it yields as below for H-pol case:

$$\hat{\ell}\cdot\vec{E}_{\ell}^{\,in}(\ell)=jk\eta\int_{Ct}(\hat{\ell}\cdot\hat{\ell}')J_{\ell}^{\,csp}(\vec{r}')G_{csp}(\vec{r}-\vec{r}',b(\vec{r}'))d\ell' \\ -\frac{j\eta}{k}\frac{\partial}{\partial\ell}\int_{Ct}\frac{\partial}{\partial\ell'}J_{\ell}^{\,csp}(\vec{r}')\cdot G_{csp}(\vec{r}-\vec{r}',b(\vec{r}'))d\ell' \tag{4.77}$$

where $\vec{E}_{\ell}^{in}(\ell)=\eta(\hat{x}\sin\phi^{in}-\hat{y}\cos\phi^{in})e^{jk(\bar{x}\cos\phi^{in}+\bar{y}\sin\phi^{in})}$. The next step is to apply the Galerkin method with triangular basis functions $t_m(\ell)$, and the EFIE is obtained by using integration by parts as follows:

$$\int_0^{\Delta_m^-+\Delta_m^+}t_m(\ell)\left(\hat{\ell}_m\cdot\vec{E}_{\ell}^{\,in}(\ell)\right)d\ell= \\ jk\eta\sum_{n=1}^{N}a_n\int_0^{\Delta_m^-+\Delta_m^+}\int_0^{\Delta_n^-+\Delta_n^+}(\hat{\ell}_m\cdot\hat{\ell}'_n)t_m(\ell)t_n(\ell')G_{csp}(\bar{x}_m-\bar{x}'_n,\bar{y}_m-\bar{y}'_n,b_n)d\ell'd\ell \\ -\frac{j\eta}{k}\sum_{n=1}^{N}a_n\int_0^{\Delta_m^-+\Delta_m^+}\frac{\partial t_m(\ell)}{\partial\ell}\int_0^{\Delta_n^-+\Delta_n^+}\frac{\partial t_n(\ell')}{\partial\ell'}G_{csp}(\bar{x}_m-\bar{x}'_n,\bar{y}_m-\bar{y}'_n,b_n)d\ell'd\ell \tag{4.78}$$

m=1,2,….N

Here $\hat{\ell}_m=\hat{x}\cos(\varphi_m)+\hat{y}\sin(\varphi_m)$ and $\hat{\ell}'_n=\hat{x}\cos(\varphi'_n)+\hat{y}\sin(\varphi'_n)$. In (4.78), since the definitions for parametric equations vary in the interval of the integrals, it must be described in the split form. The excitation matrix is given by:

$$g_m=\int_0^{\Delta_m^-}\frac{\ell}{\Delta_m^-}(\sin(\phi^{in})\cos(\varphi_m^-)-\cos(\phi^{in})\sin(\varphi_m^-))e^{jk\left[(x_{m-1}+\ell\cos\varphi_m^-)\cos\phi^{in}+(y_{m-1}+\ell\sin\varphi_m^-)\sin\phi^{in}\right]}d\ell \\ +\int_0^{\Delta_m^+}\frac{\Delta_m^+-\ell}{\Delta_m^+}(\sin(\phi^{in})\cos(\varphi_m^+)-\cos(\phi^{in})\sin(\varphi_m^+))e^{jk\left[(x_m+\ell\cos\varphi_m^+)\cos\phi^{in}+(y_m+\ell\sin\varphi_m^+)\sin\phi^{in}\right]}d\ell \tag{4.79}$$

Furthermore, the main matrix is decomposed of two parts:

$$Z_{mn}=\frac{k}{4}\sum_{n=1}^{N}a_nZ_1-\frac{1}{4k}\sum_{n=1}^{N}a_nZ_2 \tag{4.80}$$

The first part of the main matrix can be written as:

$$Z_1=(\hat{\ell}_m^{\,-}\cdot\hat{\ell}'^{\,-}_n)\int_0^{\Delta_m^-}\frac{\ell}{\Delta_m^-}\int_0^{\Delta_n^-}\frac{\ell'}{\Delta_n^-}H_0^{(2)}(kR_{csp}^{\;11})d\ell'd\ell \\ +(\hat{\ell}_m^{\,-}\cdot\hat{\ell}'^{\,+}_n)\int_0^{\Delta_m^-}\frac{\ell}{\Delta_m^-}\int_0^{\Delta_n^+}\frac{\Delta_n^+-\ell'}{\Delta_n^+}H_0^{(2)}(kR_{csp}^{\;12})d\ell'd\ell \\ +(\hat{\ell}_m^{\,+}\cdot\hat{\ell}'^{\,-}_n)\int_0^{\Delta_m^+}\frac{\Delta_m^+-\ell}{\Delta_m^+}\int_0^{\Delta_n^-}\frac{\ell'}{\Delta_n^-}H_0^{(2)}(kR_{csp}^{\;21})d\ell'd\ell \\ +(\hat{\ell}_m^{\,+}\cdot\hat{\ell}'^{\,+}_n)\int_0^{\Delta_m^+}\frac{\Delta_m^+-\ell}{\Delta_m^+}\int_0^{\Delta_n^+}\frac{\Delta_n^+-\ell'}{\Delta_n^+}H_0^{(2)}(kR_{csp}^{\;22})d\ell'd\ell \tag{4.81}$$

where $\hat{\ell}_m^{\ \pm} = \hat{x}\cos(\varphi_m^{\ \pm}) + \hat{y}\sin(\varphi_m^{\ \pm})$ and $\hat{\ell}'^{\ \pm}_n = \hat{x}\cos(\varphi_n'^{\ \pm}) + \hat{y}\sin(\varphi_n'^{\ \pm})$.

$$R_{csp}^{\ 11} = \sqrt{\left(x_{m-1} + \ell\cos\varphi_m^- - x'_{n-1} - \ell'\cos\varphi_n'^-\right)^2 + \left(y_{m-1} + \ell\sin\varphi_m^- - y'_{n-1} - \ell'\sin\varphi_n'^-\right)^2 - b_n^{\ 2}} \quad (4.82a)$$

$$R_{csp}^{\ 12} = \sqrt{\left(x_{m-1} + \ell\cos\varphi_m^- - x'_n - \ell'\cos\varphi_n'^+\right)^2 + \left(y_{m-1} + \ell\sin\varphi_m^- - y'_n - \ell'\sin\varphi_n'^+\right)^2 - b_n^{\ 2}} \quad (4.82b)$$

$$R_{csp}^{\ 21} = \sqrt{\left(x_m + \ell\cos\varphi_m^+ - x'_{n-1} - \ell'\cos\varphi_n'^-\right)^2 + \left(y_m + \ell\sin\varphi_m^+ - y'_{n-1} - \ell'\sin\varphi_n'^-\right)^2 - b_n^{\ 2}} \quad (4.82c)$$

$$R_{csp}^{\ 22} = \sqrt{\left(x_m + \ell\cos\varphi_m^+ - x'_n - \ell'\cos\varphi_n'^+\right)^2 + \left(y_m + \ell\sin\varphi_m^+ - y'_n - \ell'\sin\varphi_n'^+\right)^2 - b_n^{\ 2}} \quad (4.82d)$$

As the derivative of the triangular function is a pulse function, then the second part of the main matrix is found as below:

$$\begin{aligned} Z_2 = &\frac{1}{\Delta_m^{\ -}\Delta_n^{\ -}} \int_0^{\Delta_m^{\ -}} \int_0^{\Delta_n^{\ -}} H_0^{(2)}(kR_{csp}^{\ 11})d\ell' d\ell - \frac{1}{\Delta_m^{\ -}\Delta_n^{\ +}} \int_0^{\Delta_m^{\ -}} \int_0^{\Delta_n^{\ +}} H_0^{(2)}(kR_{csp}^{\ 12})d\ell' d\ell \\ &+ \frac{1}{\Delta_m^{\ +}\Delta_n^{\ -}} \int_0^{\Delta_m^{\ +}} \int_0^{\Delta_n^{\ -}} H_0^{(2)}(kR_{csp}^{\ 21})d\ell' d\ell + \frac{1}{\Delta_m^{\ +}\Delta_n^{\ +}} \int_0^{\Delta_m^{\ +}} \int_0^{\Delta_n^{\ +}} H_0^{(2)}(kR_{csp}^{\ 22})d\ell' d\ell \end{aligned} \quad (4.83)$$

It should be reminded that equation (4.80) can be reduced to the main matrix definition for the MoM solution, by assigning $b_n = 0$ for all n values through the equations from (4.82a) to (4.82d).

4.3.2 Determination of the Radiation Characteristics

After finding the current density function in the proposed method, the far zone scattered electric field from the cylinder can be found in E-pol. The complex source position vector $\vec{r}'_{csp}$ obtained in (4.65) is replaced with a real source vector for this geometry, $\vec{r}' \to \vec{r}'_{csp}$ in the Hankel function. Then, the far-field approximations for the proposed method, which are $R_{csp} \cong r - \vec{r}'_{csp} \cdot \hat{r}$ in phase term and $R_{csp} \cong r$ in amplitude term, are applied to the large argument form of the Hankel function. The vector scalar multiplication in CSP vector:

$$\begin{aligned} \vec{r}'_{csp} \cdot \hat{r} &= \cos(\phi)(x' - jb\sin(\varphi')) + \sin(\phi)(y' + jb\cos(\varphi')) \\ &= \cos(\phi)x' + \sin(\phi)y' - jb\left(\cos(\phi)\sin(\varphi') - \sin(\phi)\cos(\varphi')\right) \\ &= \cos(\phi)x' + \sin(\phi)y' - jb\sin(\varphi' - \phi) \end{aligned} \quad (4.84)$$

Applying (4.84) to the Hankel function:

$$\begin{aligned} \lim_{R_{csp}\to\infty} H_0^{(2)}(kR_{csp}) &= \sqrt{\frac{2j}{\pi kr}} e^{-jk(r - x'\cos\phi - y'\sin\phi + jb\sin(\varphi' - \phi))} \\ &= \sqrt{\frac{2j}{\pi kr}} e^{-jkr} e^{jk(x'\cos\phi + y'\sin\phi)} e^{kb\sin(\varphi' - \phi))} \end{aligned} \quad (4.85)$$

The scattered field at the far zone is written by substituting this large argument form of the Hankel function:

$$E_z^{\ sc} = -\frac{k\eta}{4}\int_{Ct} J_z^{\ csp}(\vec{r}')H_0^{\ (2)}(kR_{csp})d\ell'$$
$$= -\sqrt{\frac{2j}{\pi kr}}\cdot e^{-jkr}\underbrace{\left(\frac{k\eta}{4}\right)\sum_{n=1}^{N} a_n e^{kb_n \sin(\varphi_n' - \phi))}\int_0^{\Delta_n} e^{jk(\tilde{x}_n' \cos\phi + \tilde{y}_n' \sin\phi)}d\ell'}_{\psi^5(\phi)} \tag{4.86}$$

where $\psi^5(\phi)$ is the scattering pattern for *the MoM procedure with CSP type Green's function* solution in the E-pol case. The bistatic RCS is given as:

$$\sigma = 2\pi r\frac{\left|E_z^{\ sc}\right|^2}{\left|E_z^{\ in}\right|^2} = \frac{4}{k}\left|\psi^5(\phi)\right|^2 \tag{4.87}$$

In (4.86), the integral function is integrable, and it is found for computational cost:

$$\int_0^{\Delta_n} e^{jk(\tilde{x}_n' \cos\phi + \tilde{y}_n' \sin\phi)}d\ell' = e^{jk(\cos\phi(x_{ns}' + \ell'\cos\varphi_n') + \sin\phi(y_{ns}' + \ell'\sin\varphi_n'))}d\ell'$$
$$= e^{jk(x_{ns}'\cos\phi + y_{ns}'\sin\phi)}\int_0^{\Delta_n} e^{jk\ell'(\cos(\phi - \varphi_n'))}d\ell' \tag{4.88}$$
$$= \frac{e^{jk\left[x_{ns}'\cos\phi + y_{ns}'\sin\phi\right]}}{jk\cos(\phi - \varphi_n')} e^{jk\ell'\cos(\phi - \varphi_n')}\Bigg|_0^{\Delta_n}$$

Nevertheless, the term $(\phi - \varphi_n')$ can be 90^o; therefore, it can now be written as below:

$$\int_0^{\Delta_n} e^{jk(\tilde{x}_n' \cos\phi + \tilde{y}_n' \sin\phi)}d\ell' = \left\{\begin{array}{ll} \dfrac{e^{jk\left[x_{ns}'\cos\phi + y_{ns}'\sin\phi\right]}}{jk\cos(\phi - \varphi_n')}\left(e^{jk\Delta_n\cos(\phi - \varphi_n')} - 1\right) & , \quad \cos(\phi - \varphi_n') \neq 0 \\ e^{jk\left[x_{ns}'\cos\phi + y_{ns}'\sin\phi\right]}\Delta_n & , \quad \cos(\phi - \varphi_n') = 0 \end{array}\right\} \tag{4.89}$$

In H-pol, the scattered electric field has only $\hat{\phi}$ component in cylindrical coordinates since the EM wave travels in the direction $\hat{r}$, and the magnetic field is in the $\hat{z}$ direction. In the far-field region, the electric field is expressed by vector potential as $\vec{E}_\phi^{\ sc} = j\omega\vec{A}_\phi$. The far zone scattered magnetic field from the cylinder can be written through the electric field linked to the vector potential, we have:

$$\vec{H}_z^{\ sc} = \frac{1}{\eta}(\hat{r})\times(\hat{\phi})\vec{E}^{sc} = \left(-\frac{j\omega}{\eta}\right)\left(-\frac{j\mu}{4}\int_{Ct} J_s^{\ csp}(\vec{r}')H_0^{\ (2)}(kR_{csp})d\ell'\right)$$
$$= -\frac{k}{4}\int_{Ct}(\hat{\ell}'\cdot\hat{\phi})J_\ell^{\ csp}(\vec{r}')H_0^{\ (2)}(kR_{csp})d\ell' \tag{4.90}$$

Considering BC, $\hat{\ell}'$ is multiplied with the current density function in the equation. Using (4.85) for the complex source vector, and the far zone scattered magnetic field from the cylinder is:

$$\begin{aligned}\vec{H}_z^{sc} &= -\frac{k}{4}\int_{Ct}(-\cos\varphi_n'\sin\phi+\sin\varphi_n'\cos\phi)J_\ell^{csp}(\vec{r}')H_0^{(2)}(kR_{csp})d\ell' \\ &= -\sqrt{\frac{2j}{\pi kr}}e^{-jkr}\underbrace{\left(\frac{k}{4}\right)\sum_{n=1}^{N}a_n e^{kb_n\sin(\varphi_n'-\phi))}\int_0^{\Delta_n^-+\Delta_n^+}t_n(\ell')\sin(\varphi_n'-\phi)e^{jk(\overline{x}_n'\cos\phi+\overline{y}_n'\sin\phi)}d\ell'}_{\psi^6(\phi)}\end{aligned} \tag{4.91}$$

where $\psi^6(\phi)$ is the scattering pattern for *the MoM procedure with CSP type Green's function* solution in H-pol case. The bistatic RCS is given by:

$$\sigma = 2\pi r\frac{\left|H_z^{sc}\right|^2}{\left|H_z^{in}\right|^2} = \frac{4}{k}\left|\psi^6(\phi)\right|^2 \tag{4.92}$$

The integral in the far zone scattered magnetic field is algebraical and has a solution for reducing RCS computations considerably in MATLAB. The solution is found as below:

$$\begin{aligned}&\int_0^{\Delta_n^-+\Delta_n^+}t_n(\ell')\sin(\varphi_n'-\phi)e^{jk(\overline{x}_n'\cos\phi+\overline{y}_n'\sin\phi)}d\ell' = \\ &\int_0^{\Delta_n^-}\frac{\ell'}{\Delta_n^-}\sin(\varphi_n'^- -\phi)e^{jk((x_{n-1}+\ell'\cos\varphi_n^-)\cos\phi+(y_{n-1}+\ell'\sin\varphi_n^-)\sin\phi)}d\ell' \\ &+\int_0^{\Delta_n^+}\frac{\Delta_n^+-\ell'}{\Delta_n^+}\sin(\varphi_n'^+ -\phi)e^{jk((x_n+\ell'\cos\varphi_n^+)\cos\phi+(y_n+\ell'\sin\varphi_n^+)\sin\phi)}d\ell' \\ &= I1+I2\end{aligned} \tag{4.93}$$

Two parts of the integral are found separately, depending on cosine $(\phi-\varphi_n'^-)$. For the case of $\cos(\phi-\varphi_n')\neq 0$, outcomes are as below:

$$I1=\frac{\sin(\varphi_n'^- -\phi)}{\Delta_n^-}e^{jk(x_{n-1}\cos\phi+y_{n-1}\sin\phi)}\left[\frac{e^{jk\cos(\phi-\varphi_n'^-)\Delta_n^-}}{jk\cos(\phi-\varphi_n'^-)}\left(\Delta_n^- -\frac{1}{jk\cos(\phi-\varphi_n'^-)}\right)-\frac{1}{k^2\cos^2(\phi-\varphi_n'^-)}\right] \tag{4.94a}$$

$$I2=\left[\begin{array}{l}\dfrac{(e^{jk\cos(\phi-\varphi_n'^+)\Delta_n^+}-1)}{jk\cos(\phi-\varphi_n'^+)}-\dfrac{e^{jk\cos(\phi-\varphi_n'^+)\Delta_n^+}}{jk\cos(\phi-\varphi_n'^+)\Delta_n^+}\left(\Delta_n^+ -\dfrac{1}{jk\cos(\phi-\varphi_n'^+)}\right) \\ -\dfrac{1}{k^2\cos^2(\phi-\varphi_n'^+)}\end{array}\right]\sin(\varphi_n'^+ -\phi)e^{jk(x_n\cos\phi+y_n\sin\phi)} \tag{4.94b}$$

Moreover, for the case of $\cos(\phi-\varphi_n')=0$, results are as follows:

$$I1 = \frac{\sin(\varphi_n'^{-} - \phi)\Delta_n^{-}}{2} e^{jk(x_{n-1}\cos\phi + y_{n-1}\sin\phi)} \quad (4.95a)$$

$$I2 = \frac{\sin(\varphi_n'^{+} - \phi)\Delta_n^{+}}{2} e^{jk(x_n\cos\phi + y_n\sin\phi)} \quad (4.95b)$$

It should be reminded that the scattering patterns $\psi^5(\phi)$ and $\psi^6(\phi)$ are reduced to the definitions for MoM solution by assigning $b_n = 0$. Then, the bistatic RCS is found using (4.87) and (4.92) for the E-pol and H-pol case, respectively.

4.3.3 Numerical Results

In order to verify the performance of the presented method, square and triangular cross-sectional PEC cylinders have been examined in both polarisations. The proposed procedure has been applied to the cylinder geometries, as introduced in Section 4.3.1. Then, after obtaining the scattered fields presented in section 4.3.2, RCS results are shown in the following sections. In the case of cylinder geometry, Toeplitz matrix symmetries disappear. Nonetheless, a block-Toeplitz matrix can be used for this geometry; however, it was not implemented in the solution of this geometry.

4.3.3.1 Convergence Investigation of MoM Solutions for PEC Cylinder Geometries

Although MoM solution is a valid numerical technique for 2D scattering problems with $\lambda/10$ step interval, higher discretization levels have been investigated to ensure the results are in convergent nature. First, the PEC square cylinder geometry has been searched for a side of square $L = 25\lambda$ and the incidence angle $\phi^{in} = 45^o$, as shown in Figure 4.16 for both polarizations. Results are depicted by using MoM for the three different step interval, which are $\Delta = \lambda/10$, $\Delta = \lambda/20$, and $\Delta = \lambda/30$. In Figure 4.16a for the E-pol case, it has been observed that there is not any difference between the outcomes obtained from the different step intervals. In Figure 4.16b for the H-pol case, it can be seen that the result obtained from the step interval $\lambda/10$ is slightly different from the other higher segment levels in step interval for some angles.

Second, the PEC triangle cylinder geometry has been examined for $L = 25\lambda$ and the incidence angle $\phi^{in} = 90^o$ in both polarizations as shown in Figure 4.17. Similar results to the square cross-section geometry have been achieved for both polarizations.

The major lobes in the RCS figures have matched each other perfectly for all step intervals. Slight deviations occur in the angles of minor lobes only for the H-pol case. However, these regions are insignificant in the dB magnitudes scale when compared to the major lobes in the scattering pattern. Thus, these deviations do not affect RE comparisons. Consequently, MoM solutions for these geometries have converged to the realistic solutions using the step interval $\Delta = \lambda/10$. Hence, all results analyzed in the next sections have been obtained using the step interval $\Delta = \lambda/10$ for the MoM and proposed methods.

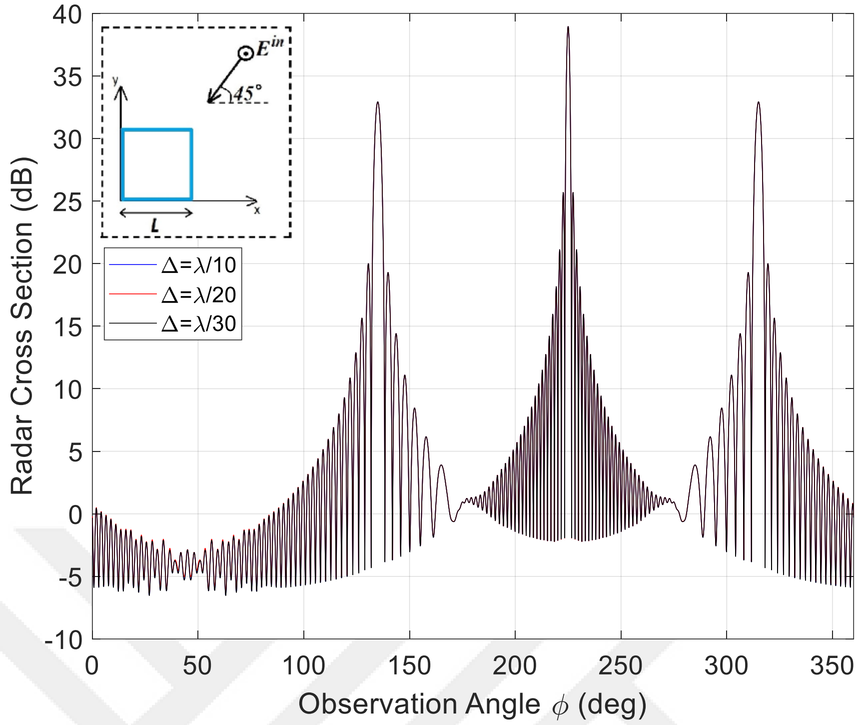

(a) E-pol case

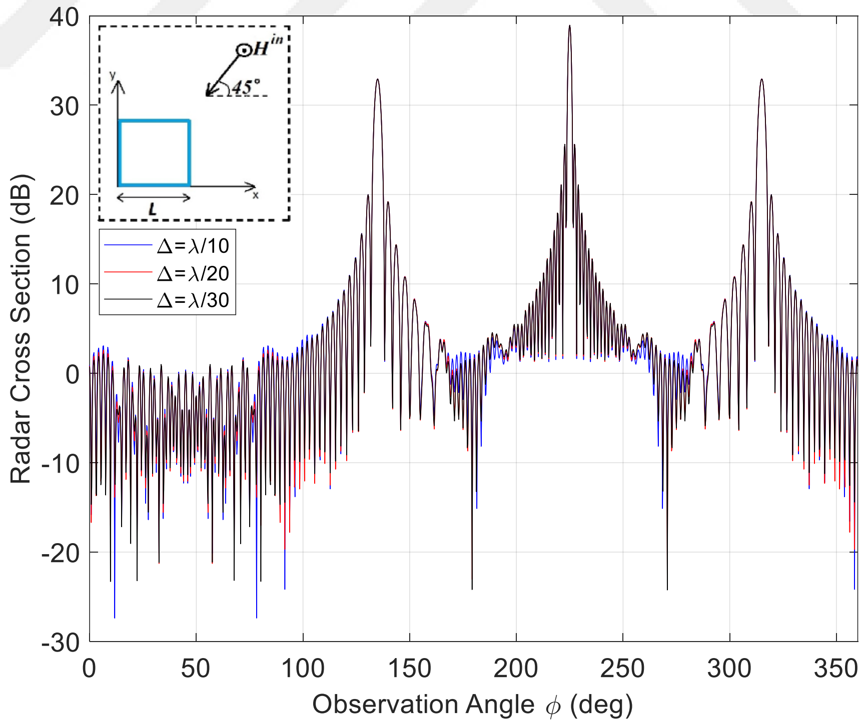

(b) H-pol case

Figure 4.16 RCS pattern comparison between the step intervals in the standard MoM for square cross-section PEC cylinder, L = 25λ, $\phi^{in} = 45^o$

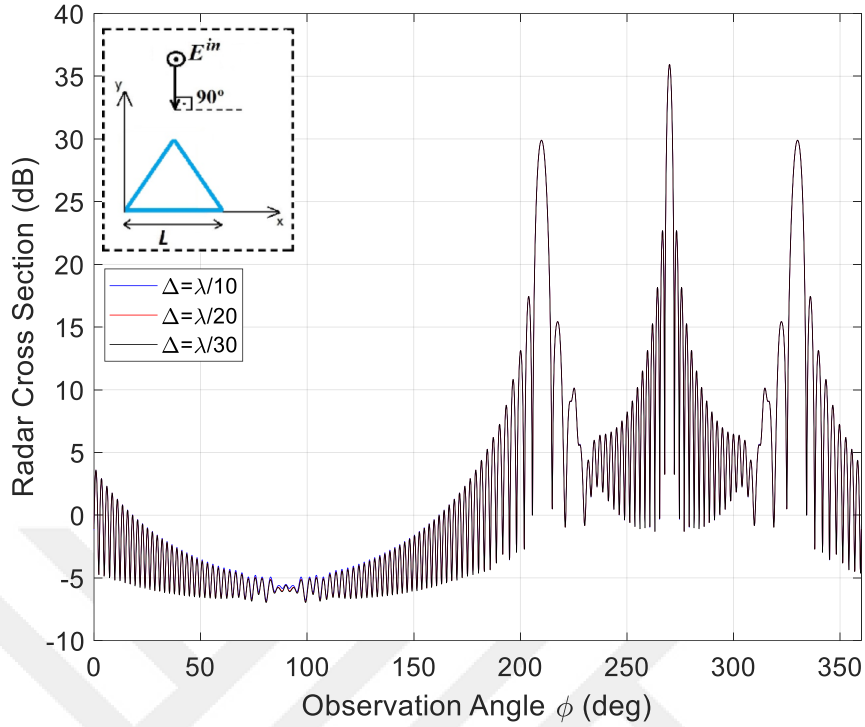

(a) E-pol case

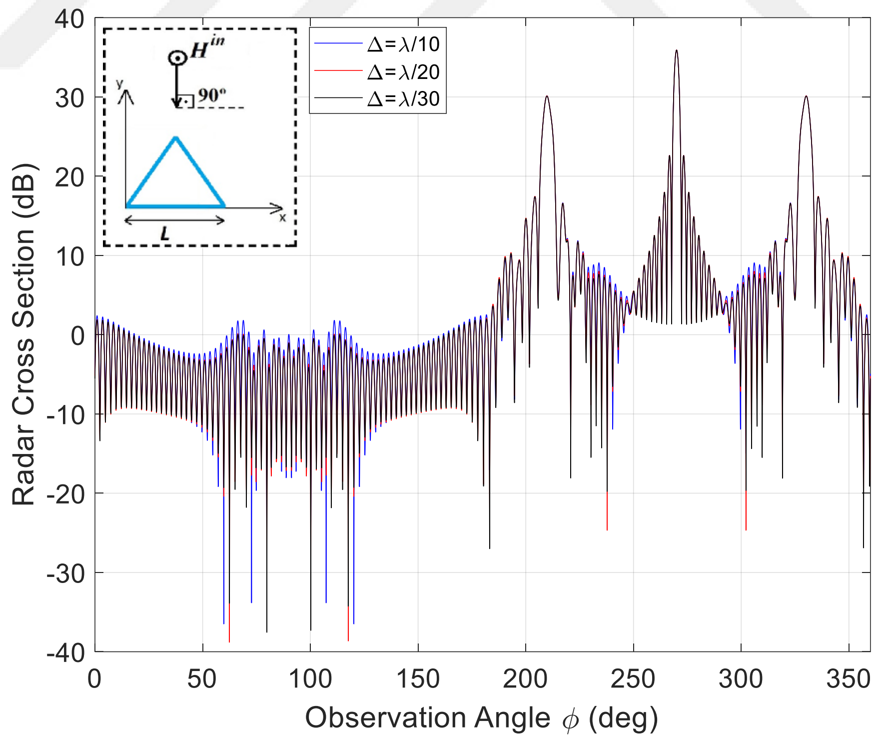

(b) H-pol case

Figure 4.17 RCS pattern comparison between the step intervals in the standard MoM for triangle cross-section PEC cylinder, L = 25λ, $\phi^{in} = 90^{o}$

4.3.3.2 Square Cross-Sectional PEC Cylinder Geometry

Here, the square shape of a PEC cylinder cross-section is considered with a side width of 25λ. The incidence angle is assumed as $\phi^{in} = 45^o$ for both polarisations. In Figure 4.18a, the obtained bistatic RCS from equation (4.87) has been plotted for the E-polarization case, and in Figure 4.18b for the H-polarization case using (4.92). The outcomes are excellent agreement with the MoM, and REs are minimal values such as 0.01% for E-pol case and 0.18% for H-pol case.

Figure 4.19 depicts the RE plots for the PEC square cylinder geometry. In all cases for $\alpha \geq b$, the RE values are approximately one percent or less. As highlighted earlier, the selection of the parameters b and α is satisfied with our main statements and convenient with the related section.

Figure 4.20 represents the obtained bistatic RCS for the incidence angle $\phi^{in} = 90^o$ and $L = 25\lambda$ with less than one percent REs for both polarisations. Due to the incident angle, two edges of the PEC square cylinder are illuminated by the wave with grazing incidence. So the problem can be considered similar to the inclined incidence at the PEC strip, as presented in section 4.2.4. Therefore, the CSP Green's function parameter values were assigned $b = 2.5\lambda$ and $\alpha = 4\lambda$ for both polarisations, like in the inclined incidence case for the strip geometry.

To realize the problem with very large size in this geometry, the method has been tested with a facet of square $L = 250\lambda$ and incidence angle $\phi^{in} = 45^o$ for both polarizations. In this size, since the edge effects are less important as the geometry becomes larger, it is chosen $\alpha = b$. In Figure 4.21, by assigning $\alpha = b = 3\lambda$, remarkable results have been observed in RCS plots with REs 0.002% and 0.05% for E-pol and H-pol, respectively. The step number in RCS computation of this large structure was reduced to smaller ones for clearly recognizing the comparisons.

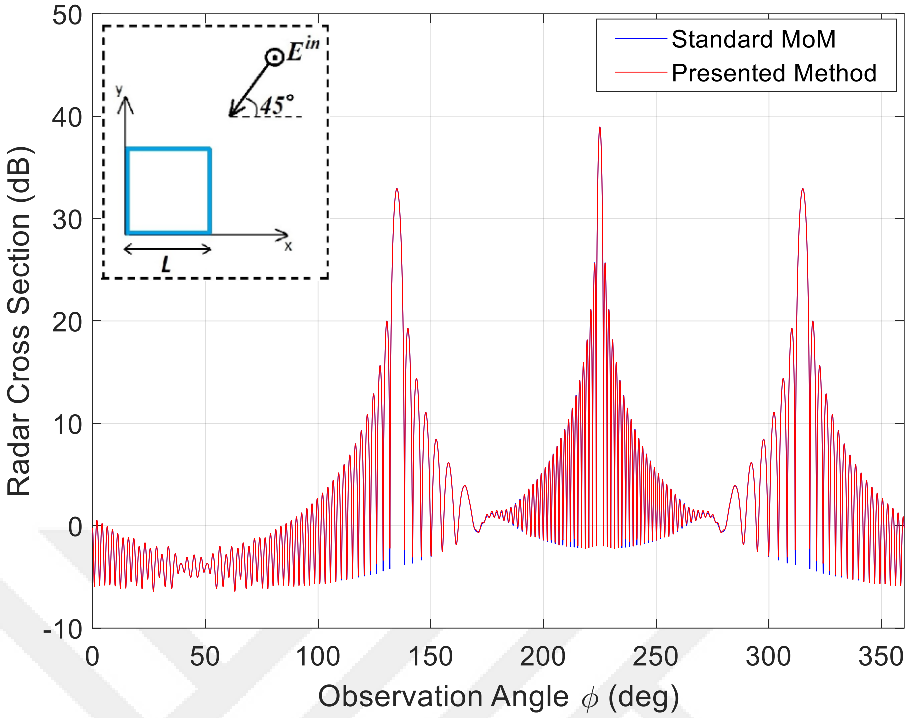

(a) E-pol case, b = 2.5λ, α = 3.1λ and RE = 0.01%

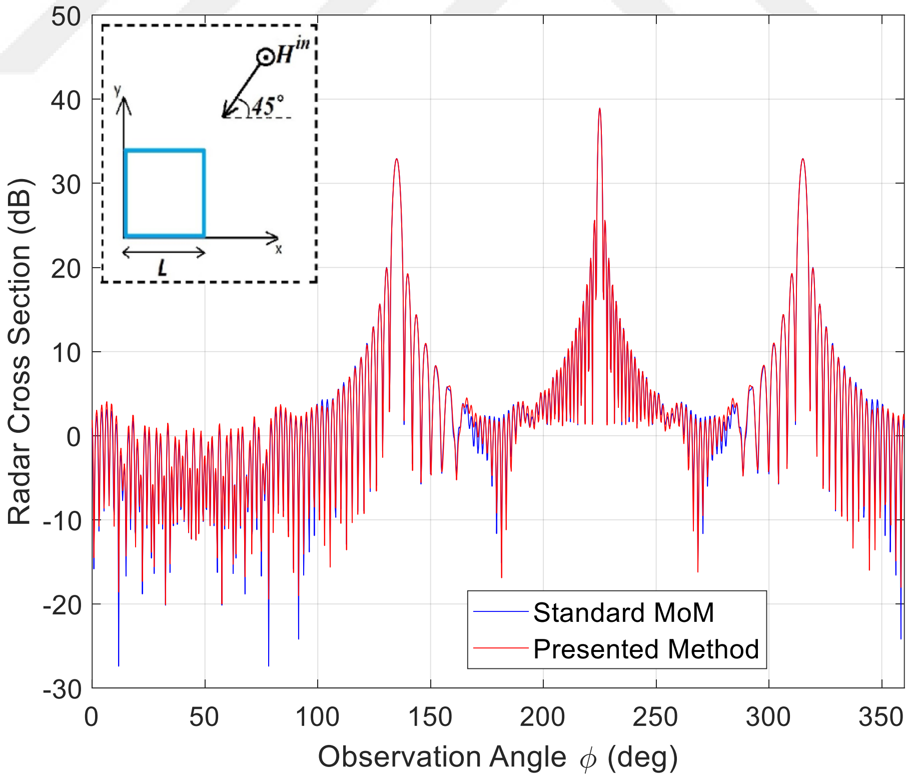

(b) H-pol case, b = 2.5λ, α = 3.3λ and RE = 0.18%.

Figure 4.18 RCS pattern comparison between the standard MoM and the proposed method for L = 25λ, $\phi^{in} = 45^o$

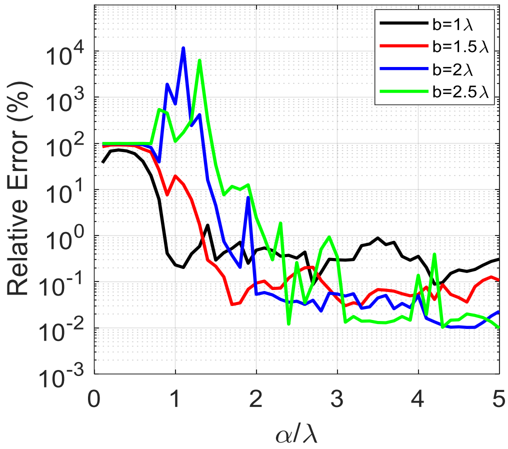

(a)

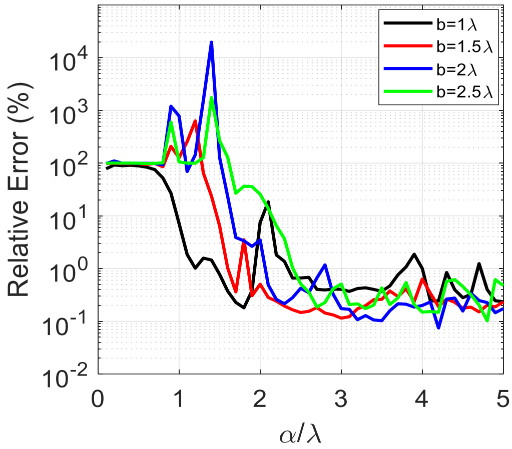

(b)

Figure 4.19 RE plots for square geometry L = 25λ, ϕ^{in} = 45° (a) E-pol and (b) H-pol

Beyond the facet length L = 250λ, the computer encounters an error message in MATLAB with insufficient memory for the MoM solution. For this reason, the comparison is restricted with this size, while the proposed method runs properly without any error. The number of memory storage is demonstrated in Table 4.3 and Table 4.4 for PEC square cylinder geometry for both polarizations. The memory restriction in MoM solution for H-pol case is from the facet length L = 200λ, thereby comparing the standard MoM and the proposed method is limited to this length for the H-pol case.

The overall CPU time for obtaining the current density function is also presented in Table 4.3 and Table 4.4 for the MoM and the proposed method. Significant time gains have been achieved in the largest sizes for both polarizations, such as over 30 times less compared to the MoM solution. Furthermore, REs values are less than 0.1%, although the geometrical size of the problem is extended notably.

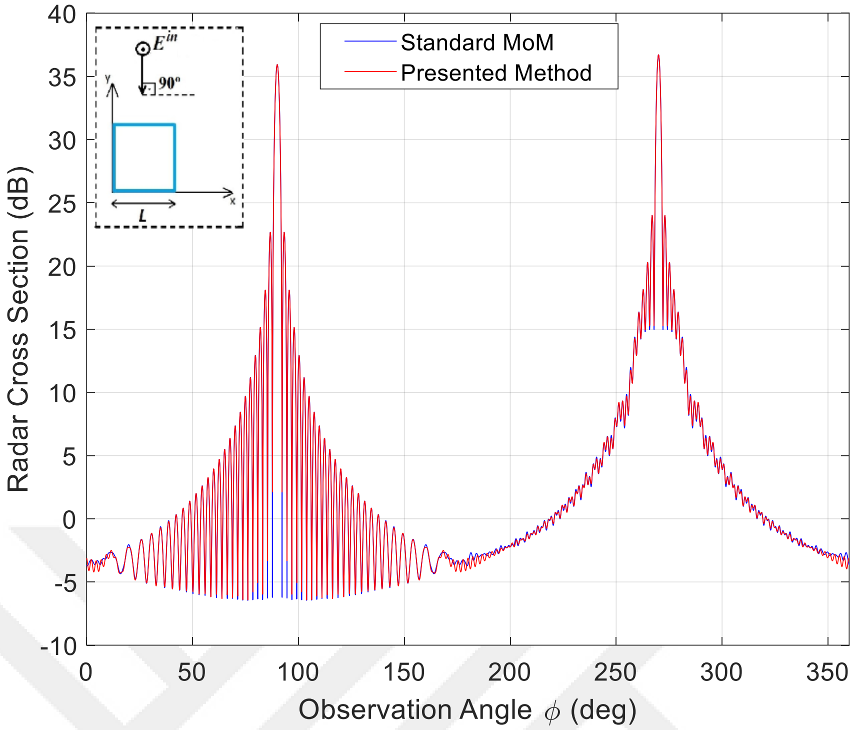

(a) E-pol case, b = 2.5λ, α = 4λ and RE = 0.09%

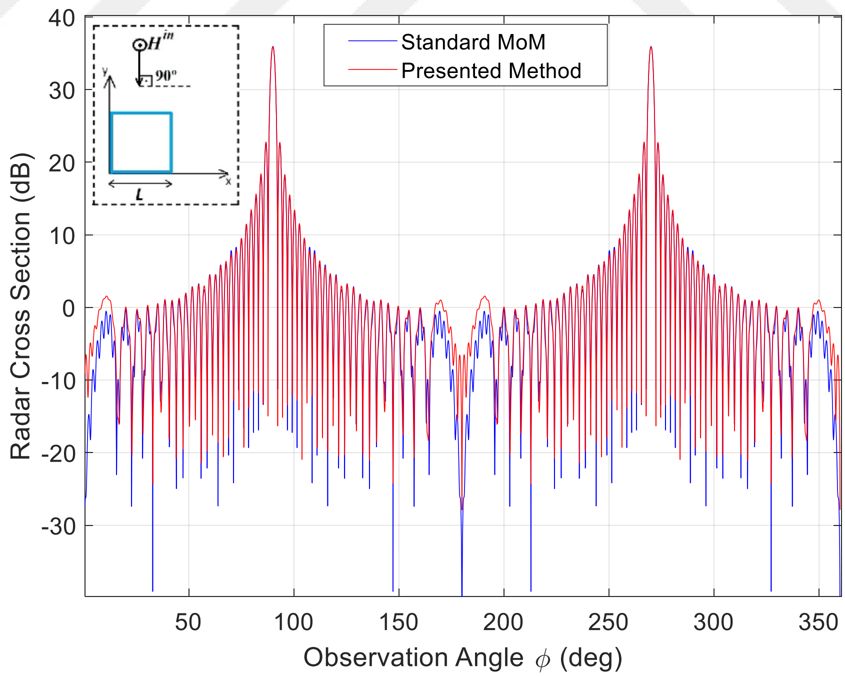

(b) H-pol case, b = 2.5λ, α = 4λ and RE = 0.34%

Figure 4.20 RCS pattern comparison between the standard MoM and the proposed method for L = 25λ, $\phi^{in} = 90^o$

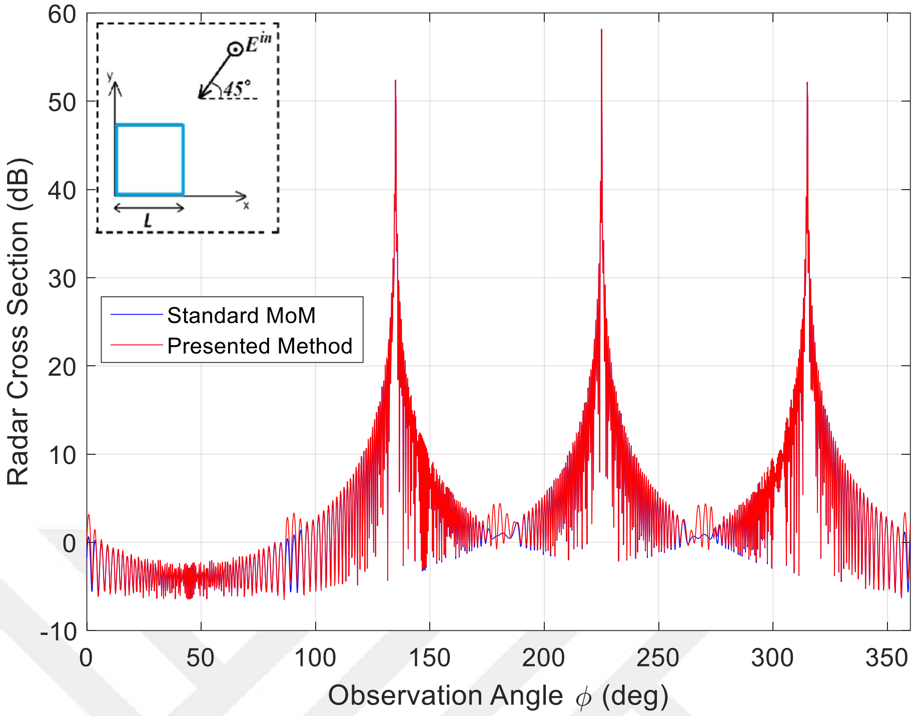

(a) E-pol case, L = 250λ b = 3λ, α = 3λ and RE = 0.002%

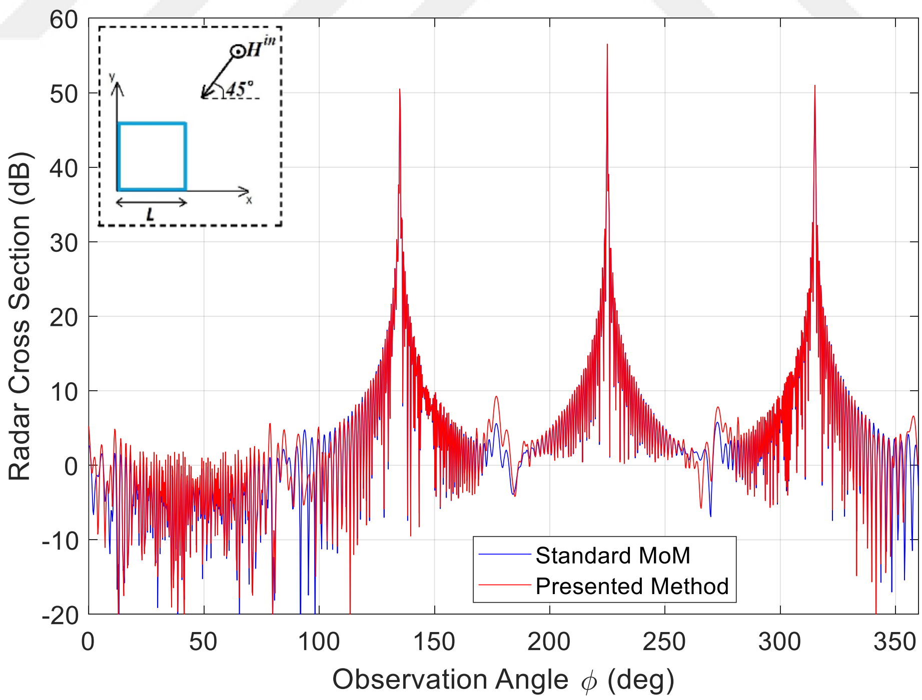

(b) H-pol case, L = 200λ, b = 3λ, α = 3λ and RE = 0.05%

Figure 4.21 RCS pattern comparison between the standard MoM and the proposed method for $\phi^{in} = 45^o$

In order to check the convergence of the solution, according to section 4.3.3.1, different step sizes in discretization have been considered for PEC square cylinder geometry with the incidence angle $\phi^{in} = 45^o$ and $L = 25\lambda$. RE values between the MoM and presented method have been found 0.01%, 0.005%, 0.005% in E-pol and 0.14%, 0.06%, 0.10% in H-pol for $\Delta = \lambda/10$, $\Delta = \lambda/20$, and $\Delta = \lambda/30$, respectively. They are very close to each other and around one per thousand. As expected, solutions have converged for the discretization levels $\lambda/10$ or less.

Figure 4.22 shows the running CPU solution times for the MoM and the presented method according to the total number of unknown N for all sizes of PEC square cylinder geometry. From those figures, the advantage of the proposed method is clearly seen, and the timelines deviate from each other when the size is more extensive. Nevertheless, the more important part is the declination that belongs to the proposed method. It assures that the total number of the unknown for the proposed method will be low enough to solve the problem even if the problem size is extremely large.

Table 4.3 CPU time and memory storage comparison for PEC square cylinder geometry (E-Pol)

Cross-sectional area	**Length of the facet (λ)**	**Incident angle (degree)**	**b (λ)**	**α (λ)**	**Solution Time For E-pol (seconds)**		**Memory Storage**			**Relative error (%)**
					MoM	***Presented method***	***Number of the unknown, N***	***MoM***	***Presented method***	
Square	L=25	45	2.5	3.1	1572	368	1000	1000·N	298·N	0.01
Square	L=25	90	2.5	4	1526	482	1000	1000·N	370·N	0.09
Square	L=100	45	3	3	24874	1634	4000	4000·N	300·N	0.008
Square	L=250	45	3	3	153671	4173	10000	10000·N	300·N	0.002

Table 4.4 CPU time and memory storage comparison for PEC square cylinder geometry (H-Pol)

Cross-sectional area	**Length of the facet (λ)**	**Incident angle (degree)**	**b (λ)**	**α (λ)**	**Solution Time For H-pol (seconds)**		**Memory Storage**			**Relative error (%)**
					MoM	***Presented method***	***Number of the unknown, N***	***MoM***	***Presented method***	
Square	L=25	45	2.5	3.3	8397	1956	1000	1000·N	314·N	0.14
Square	L=25	90	2.5	4	8411	2218	1000	1000·N	370·N	0.34
Square	L=100	45	3	3	109135	8055	4000	4000·N	300·N	0.12
Square	L=200	45	3	3	473588	13869	8000	8000·N	300·N	0.05

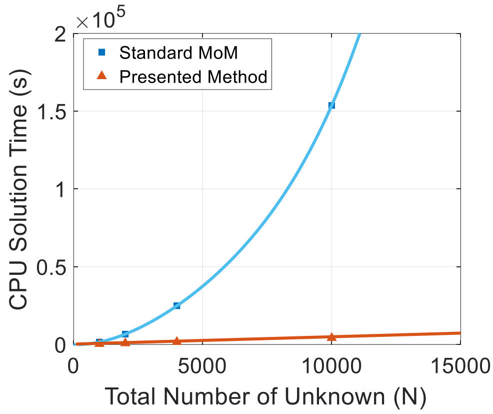

(a)

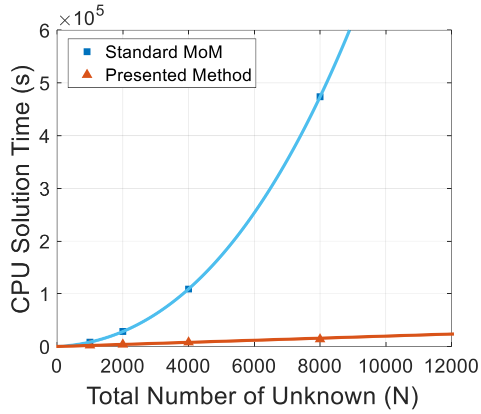

(b)

Figure 4.22 The running CPU solution times of the computation current density function versus the total number of unknown for PEC cylinder geometry (a) E-pol and (b) H-pol

4.3.3.3 Triangle Cross-Sectional PEC Cylinder Geometry

Here, a different cross-sectional geometrical shape of the cylinder has been examined to present the method availability. In Figure 4.23, the triangle shape of a PEC cylinder cross-section is considered with a side width of 25λ. The incidence angle is assumed as $\phi^{in} = 90^o$ for both polarisations. Quite satisfying results have also been obtained for this geometry with very small REs, which are less than 0.1%, as seen in Figure 4.24.

The incidence angle $\phi^{in} = 45^o$ can be considered as an inclined angle for this geometry because the incident wave impinges on only one surface of the cylinder. Therefore, as in the previous geometries, edge effects are effective, and it has been achieved good results by setting α values a bit larger. In Figure 4.25, RCS pattern comparisons are presented for $L = 25\lambda$ and $\phi^{in} = 45^o$ for both polarizations.

The method has also been shown with a very large size for the problem in both polarizations and incidence angle $\phi^{in} = 90^o$. As mentioned before in square geometry for this size, favorable RCS outcomes have been obtained by setting $\alpha = b = 3\lambda$. In Figure 4.26, RCS plots are illustrated for E-pol case with a facet of triangle $L = 250\lambda$ and H-pol case with a facet of triangle $L = 200\lambda$. Considerable REs have also been reached in this structure with 0.81% and 0.05% for E-pol and H-pol, respectively.

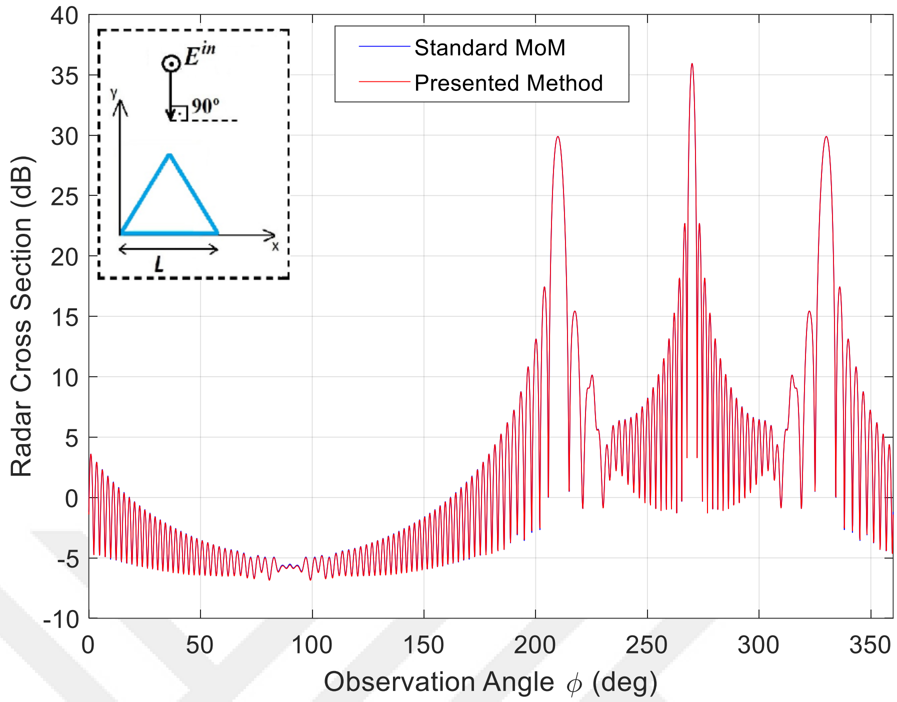

(a) E-pol case, b = 2.5λ, α = 3.5λ and RE = 0.01%

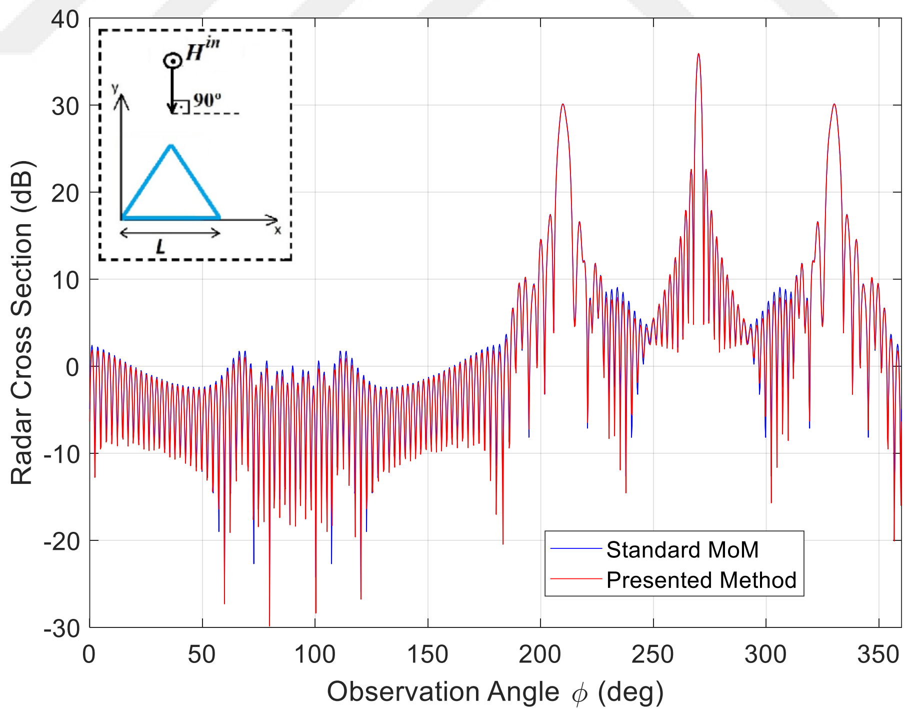

(b) H-pol case, b = 2.5λ, α = 3λ and RE = 0.16%

Figure 4.23 RCS pattern comparison between the standard MoM and the proposed method for L = 25λ, $\phi^{in} = 90^o$

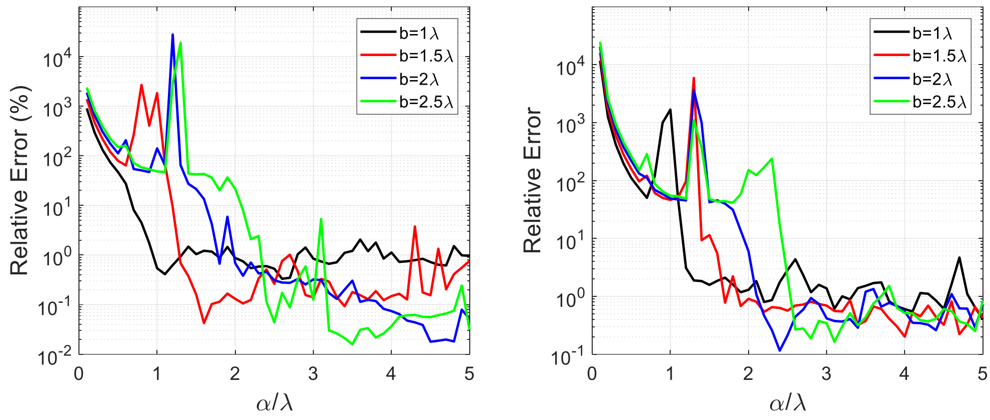

(a) (b)

Figure 4.24 RE plots for triangle geometry L = 25λ, ϕ^{in} = 90° (a) E-pol and (b) H-pol

The overall CPU time and memory storage comparisons are listed in Table 4.5 and Table 4.6 for the MoM and the proposed method in this geometry. Respectable time gains have also been achieved in the largest sizes for both polarizations such as over 20 times in E-pol and 30 times in H-pol, compared to the MoM solution. Moreover, RE values indicate that analyzing very large sizes is possible.

Like in the square cross-sectional case, different discretization levels have been examined for PEC triangle cylinder geometry to explore the convergence of solution with the incidence angle $\phi^{in} = 90^o$ and $L = 25\lambda$. RE values between the MoM and presented method have been obtained 0.01%, 0.03%, 0.02% in E-pol and 0.16%, 0.04%, 0.59% in H-pol for $\Delta = \lambda/10$, $\Delta = \lambda/20$, and $\Delta = \lambda/30$, respectively.

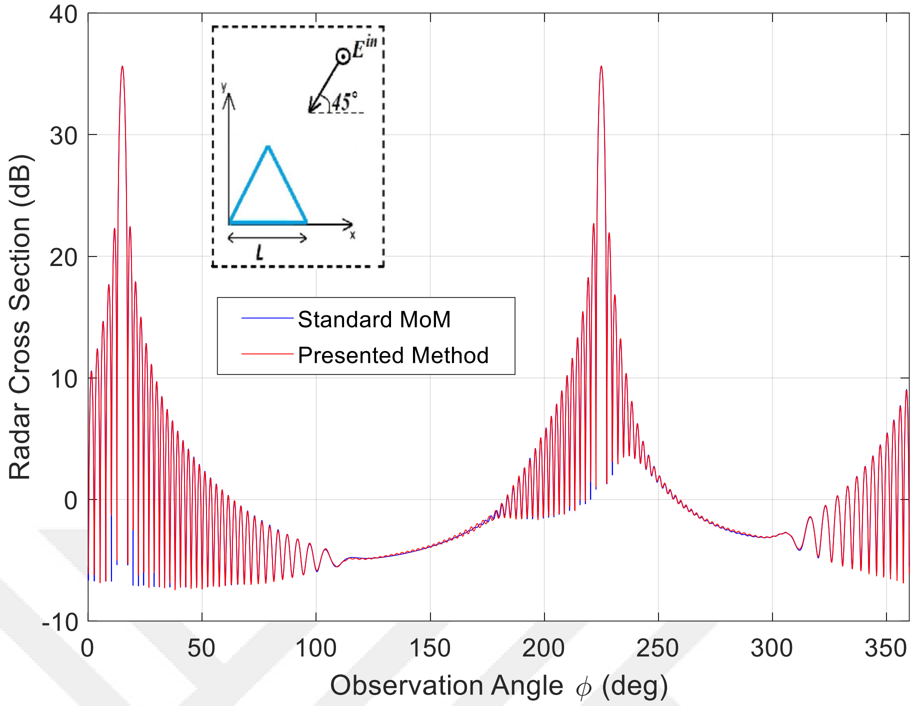

(a) E-pol case, b = 2.5λ, α = 3.8λ and RE = 0.04%

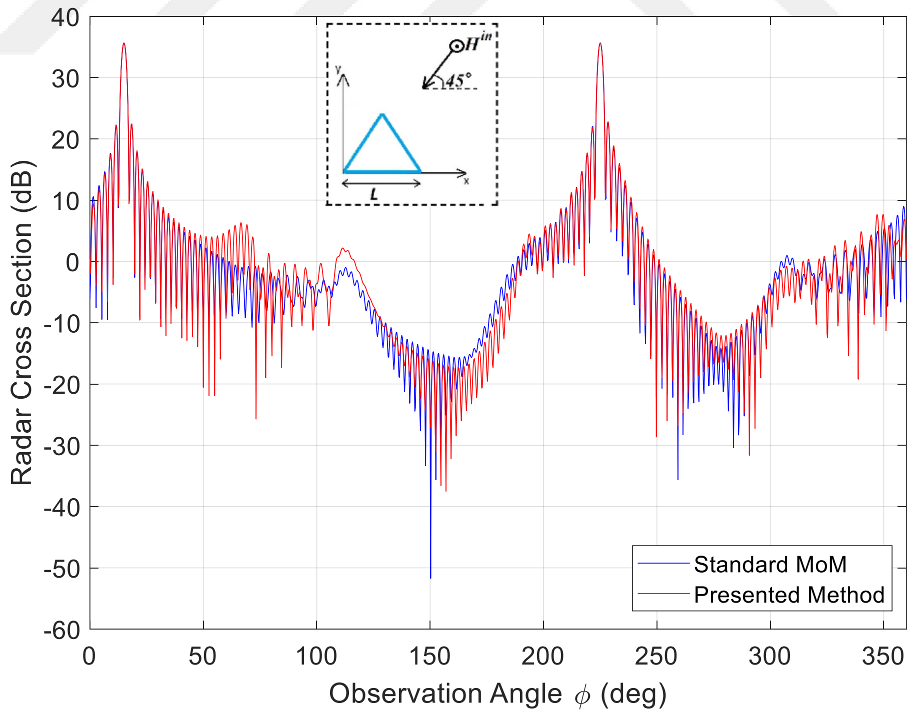

(b) H-pol case, b = 2.5λ, α = 4λ and RE = 0.61%

Figure 4.25 RCS pattern comparison between the standard MoM and the proposed method for L = 25λ, $\phi^{in} = 45^o$

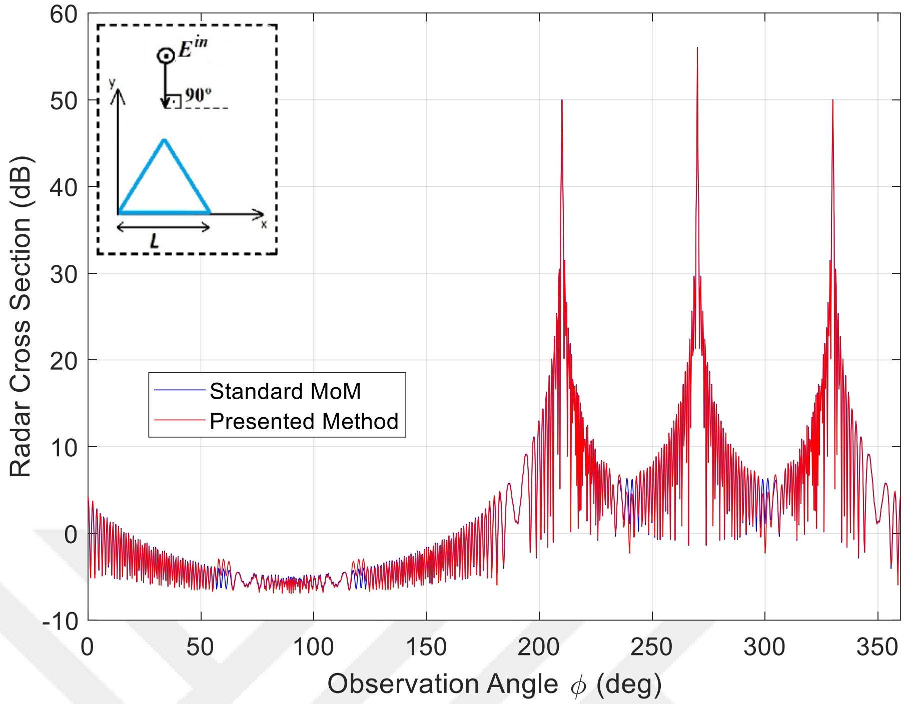

(a) E-pol case, L = 250λ b = 3λ, α = 3λ and RE = 0.81%

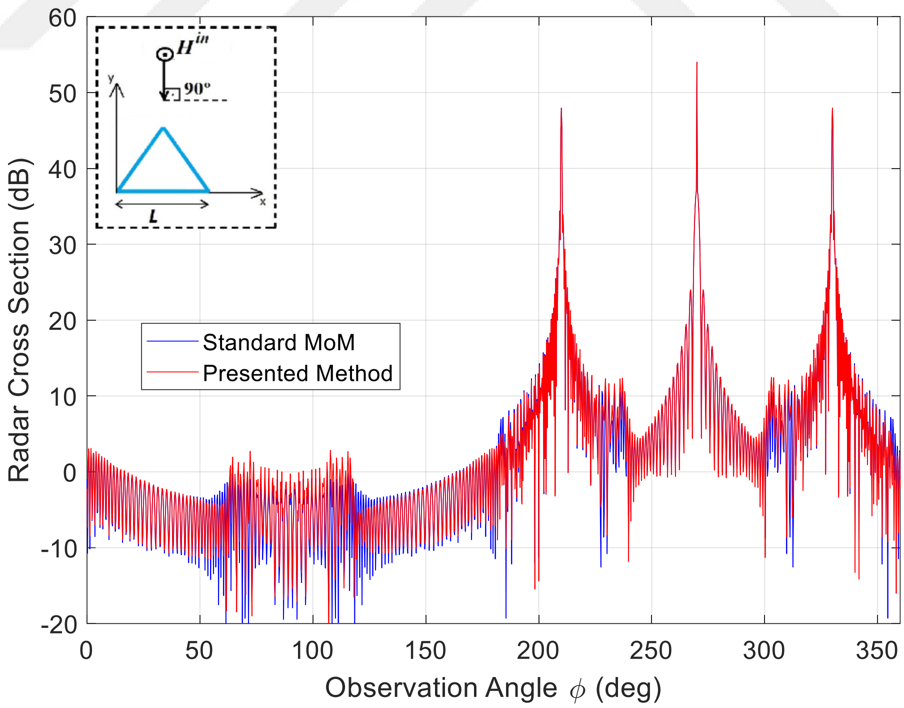

(b) H-pol case, L = 200λ, b = 3λ, α = 3λ and RE = 0.05%

Figure 4.26 RCS pattern comparison between the standard MoM and the proposed method for $\phi^{in} = 90^o$

Table 4.5 CPU time and memory storage comparison for PEC triangle cylinder geometry (E-Pol)

Cross-sectional area	Length of the facet (λ)	Incident angle (degree)	b (λ)	α (λ)	Solution Time For E-pol (seconds)		Memory Storage			Relative error (%)
					MoM	*Presented method*	*Number of the unknown, N*	*MoM*	*Presented method*	
Triangle	L=25	45	2.5	3.8	982	304	750	750·N	278·N	0.04
Triangle	L=25	90	2.5	3.5	967	284	750	750·N	260·N	0.01
Triangle	L=100	90	3	3	14863	907	3000	3000·N	240·N	0.09
Triangle	L=250	90	3	3	83054	2574	7500	7500·N	240·N	0.81

Table 4.6 CPU time and memory storage comparison for PEC triangle cylinder geometry (H-Pol)

Cross-sectional area	Length of the facet (λ)	Incident angle (degree)	b (λ)	α (λ)	Solution Time For H-pol (seconds)		Memory Storage			Relative error (%)
					MoM	*Presented method*	*Number of the unknown, N*	*MoM*	*Presented method*	
Triangle	L=25	45	2.5	4	3556	1057	750	750·N	290·N	0.61
Triangle	L=25	90	2.5	3	3497	1038	750	750·N	230·N	0.16
Triangle	L=100	90	3	3	59109	3648	3000	3000·N	240·N	0.26
Triangle	L=200	90	3	3	231284	7682	6000	7500·N	240·N	0.05

4.3.3.4 A Large PEC Open Body Structure

Unlike the previous examples, the third geometry has been investigated in this section for the proposed method. Open body structure, like a corner reflector geometry, as shown in Figure 4.27, has been investigated for both polarizations.

The procedure is the same as the polygonal cylinder geometry in the previous parts. Hence, the same formulation is used with the complex beam vector, as described in (4.63). The angle φ between the edge and the *x*-axis is determined by following the counter-clockwise path direction on edge. However, the beam radiation must be tracked from the observation angle during the RCS computations. To ensure the implementation of this requirement, the opposite direction of the beam vector should be taken for some degrees. For instance, in strip geometry, the CSP beam was launching from the x-axis to the upward y-direction, as in Figure 4.4. Therefore, the beam direction was reversed for the observation angles $180^o \leq \phi \leq 360^o$ in the strip

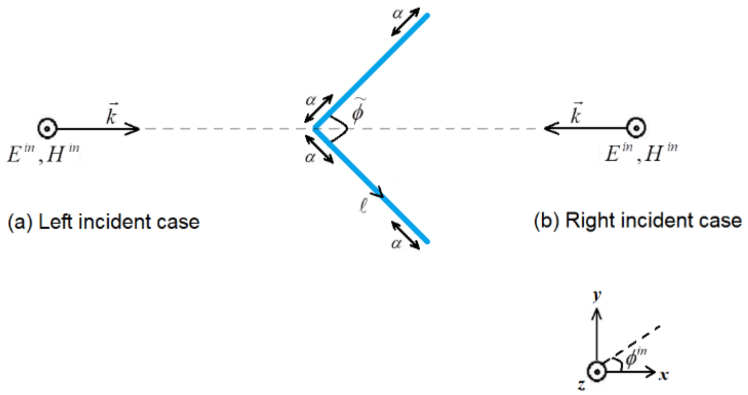

Figure 4.27 2D PEC corner reflector geometry (a) Left incident case ϕ^{in} = 180º and (b) Right incident case ϕ^{in} = 0º

geometry. If the corner reflector with the angle $\tilde{\phi} = 120^o$ is at the origin on the x-y plane, beam direction is reversed for the observation angles -60º ≤ ϕ ≤ +60º. This action does not make any difference in the main matrix elements when the current density function is found. Because the last terms in equation (4.68a) and (4.68b) would cancel each other again, it is obtained the same CSP type Green's function mathematically. However, the beam vector in (4.84) changes the sign in the term $e^{kb\sin(\varphi'-\phi))}$ for the scattered field. Briefly, beam radiations interact with each other for the observation angles -60º ≤ ϕ ≤ +60º, and the scattered fields should be regarded as an incident field for the next iteration. This research, based on the iterations, will be left as another study in the future.

Since the interactions between beam radiations can affect the solution for angles $\tilde{\phi} < 90^{\,o}$, so the structures with angle $\tilde{\phi} = 120^o$ are examined in this section. Figure 4.28 presents the RCS pattern comparison between the standard MoM and the proposed method for the left incident case in E-pol. As expected, the RCS plots are in harmony with each other for L = 25λ, L = 250λ, and $\phi^{\,in}$ = 0º with REs around 1%.

For the right incident case, which is more often used in corner reflector geometry, the outcomes are more compatible, as shown in Figure 4.29. The results are remarkable for E-pol with RE 0.63% and 0.61% for L = 25λ, L = 250λ, respectively. RCS plots are shown in Figure 4.30 for H-pol and the right incident case, for L = 25λ, L = 250λ. The comparisons are matched and satisfied in RCS computations with very small RE values such as 0.37% for L = 25λ and 0.03% for L = 250λ.

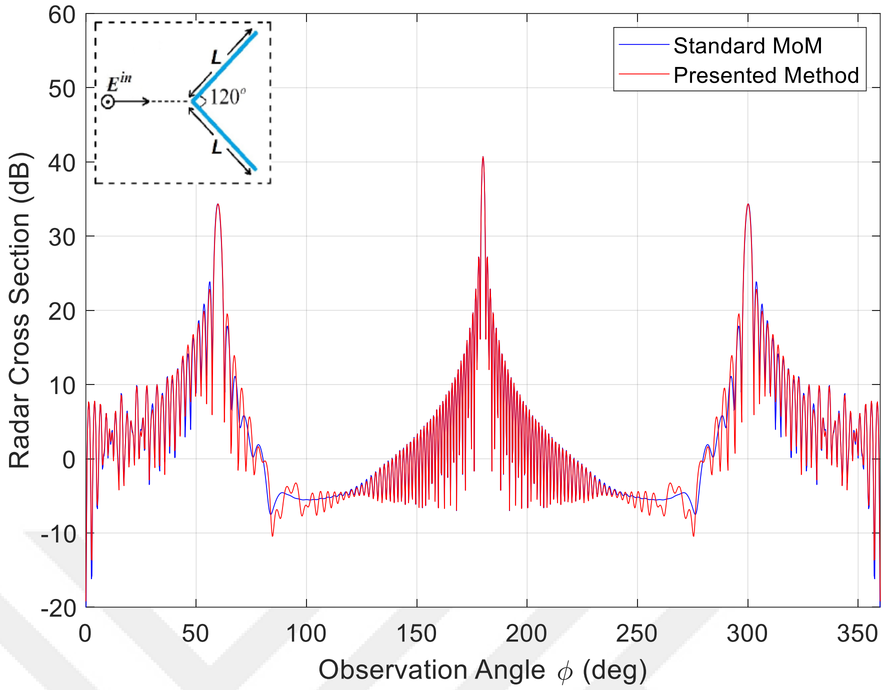

(a) L = 25λ, b = 1.5λ, α = 2.7λ and RE = 1.58%

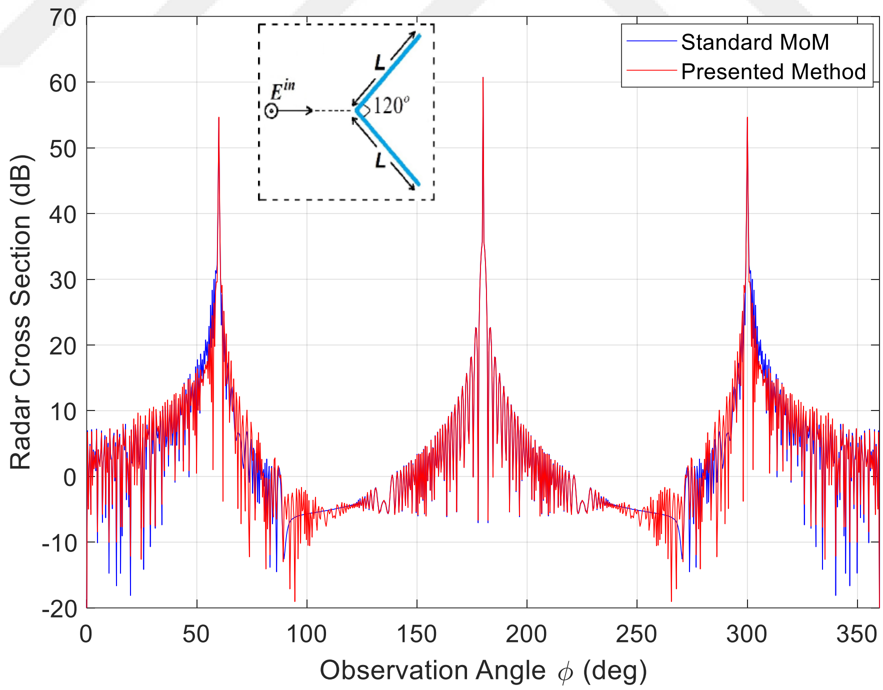

(b) L = 250λ b = 2.5λ, α = 2.5λ and RE = 1.4%

Figure 4.28 RCS pattern comparison between the standard MoM and the proposed method for E-pol case, $\tilde{\phi} = 120^o$ and $\phi^{in} = 0^o$

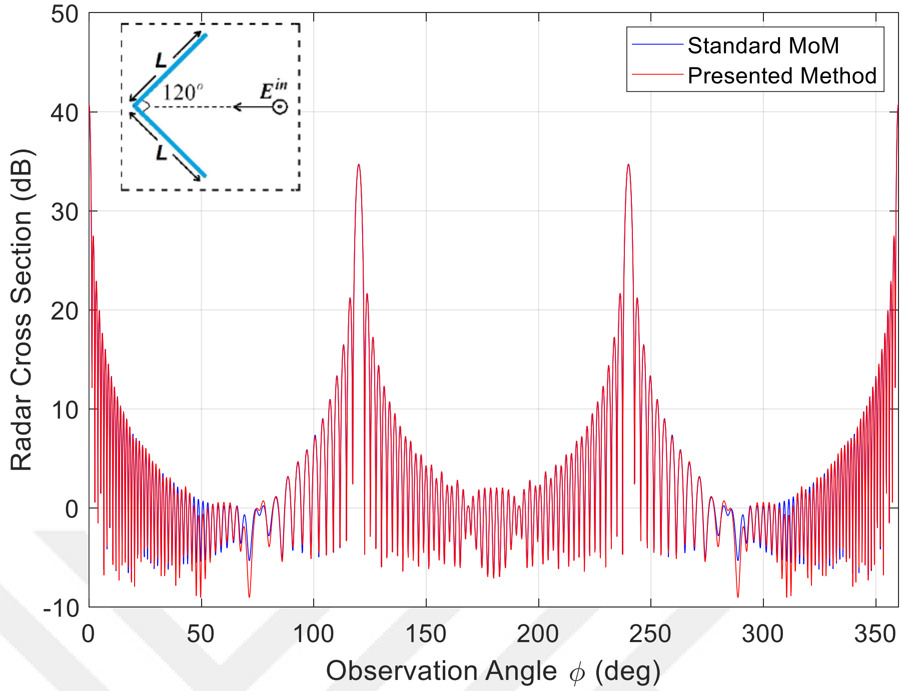

(a) L = 25λ, b = 1.5λ, α = 2λ and RE = 0.63%

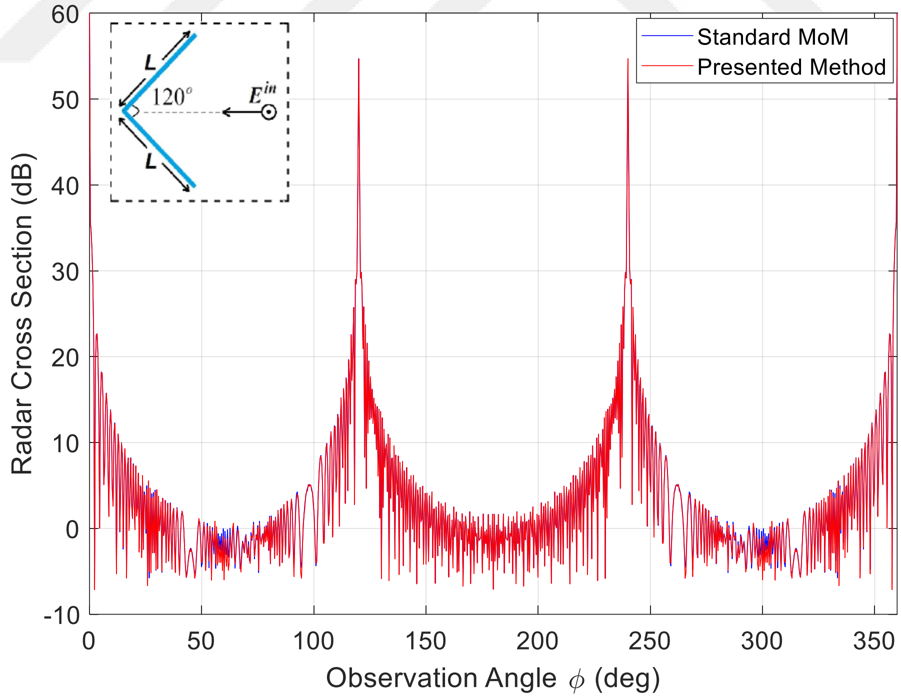

(b) L = 250λ b = 2.5λ, α = 2.5λ and RE = 0.61%

Figure 4.29 RCS pattern comparison between the standard MoM and the proposed method for E-pol case, $\tilde{\phi} = 120^o$ and $\phi^{in} = 180^o$

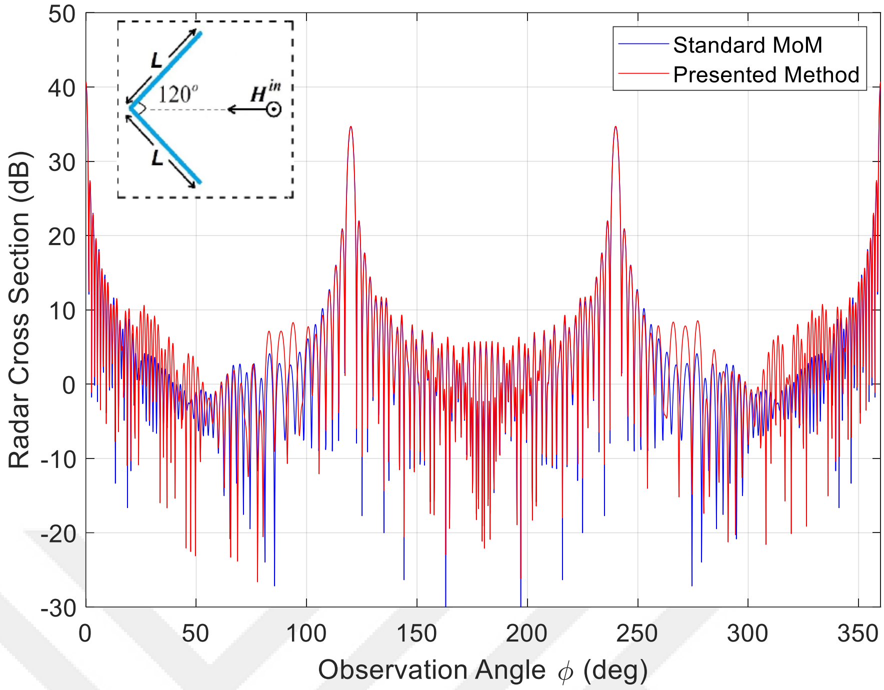

(a) $L = 25\lambda$, b = 2.5λ, α = 2.5λ and RE = 0.37%

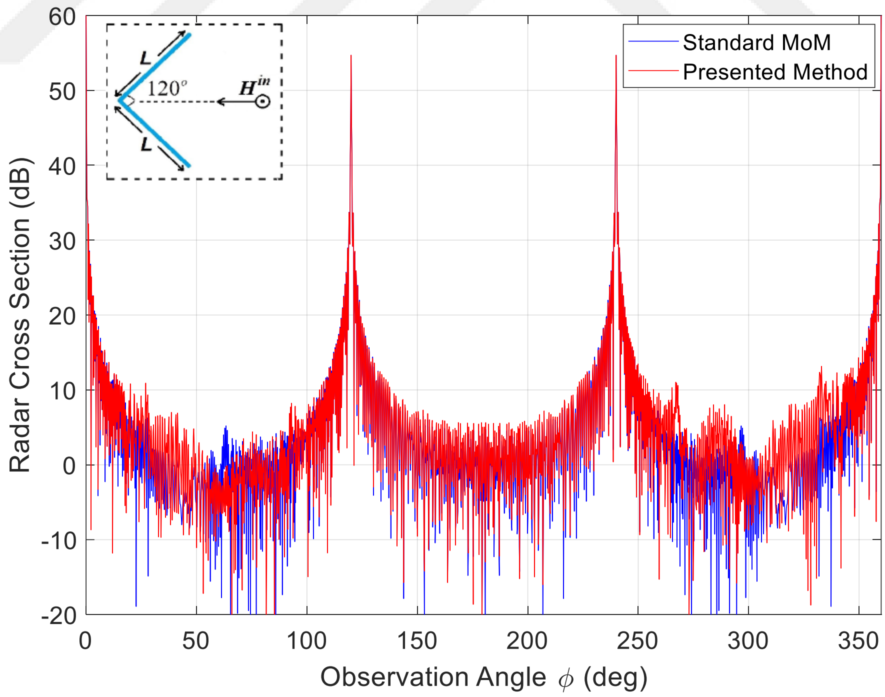

(b) $L = 250\lambda$ b = 2.5λ, α = 2.5λ and RE = 0.03%

Figure 4.30 RCS pattern comparison between the standard MoM and the proposed method for H-pol case, $\tilde{\phi} = 120^o$ and $\phi^{in} = 180^o$

The CPU time and memory storage comparisons for the PEC corner reflector geometry are denoted in Table 4.7. As the previous results, substantial time gain have also been observed in this geometry. For $L = 250\lambda$, solution time gains are over 40 times less than the MoM solution in both polarizations.

Table 4.7 CPU time and memory storage comparison for PEC corner reflector geometry

Polarization of incident	**Length of the facet (λ)**	**Incident angle (degree)**	**b (λ)**	**α (λ)**	**Solution Time (seconds)**		**Memory Storage**			**Relative error (%)**
					MoM	***Presented method***	***Number of the unknown, N***	***MoM***	***Presented method***	
E-pol	L=25	0	1.5	2.7	512	81	500	500·N	138·N	1.58
E-pol	L=250	0	2.5	2.5	48523	1056	5000	5000·N	150·N	1.4
E-pol	L=25	180	1.5	2	493	68	500	500·N	110·N	0.63
E-pol	L=250	180	2.5	2.5	46143	1021	5000	5000·N	150·N	0.61
H-pol	L=25	180	2.5	2.5	1806	362	500	500·N	150·N	0.37
H-pol	L=250	180	2.5	2.5	145698	3348	5000	5000·N	150·N	0.03

CHAPTER FIVE
MORE LOCALIZATION WITH MODIFIED GREEN'S FUNCTION BY USING GENERALIZED PENCIL OF FUNCTION METHOD

5.1 Generating a Beam-Pattern Function Using the Generalized Pencil of Function Method

As a second hybrid technique, the GPOF method combined with MoM will be presented in this chapter. The late-time EM field, scattered from a finite-sized conducting body, is represented as a sum of damped sinusoids (Lee & Kim, 1999):

$$y(t) = \sum_{s=1}^{M} c_s e^{w_s \cdot t} \tag{5.1}$$

where c_s and w_s are the complex residues and complex natural frequencies, respectively. The GPOF method (Hua & Sarkar, 1989; Mohammadi-Ghazi & Büyüköztürk, 2016) is proposed to obtain these natural frequencies from the transient response of a target. The GPOF method is also used in approximating the spectral domain Green's functions (Dural & Aksun, 1995). In light of this information, spectral-domain functions can be defined by finding the coefficients from the GPOF method, which are obtained in the time domain.

Modeling of the EM scattering from the PEC strip has been formalized with CSP Type Green's Function in section 4.2.1. To obtain a new modified Green's function, a pulse function is convoluted with itself as a first step. Assuming a rectangular pulse function *p(x)* in a spatial domain with the pulse width of *2W* and located on the origin symmetrically, as shown in Figure 5.1.

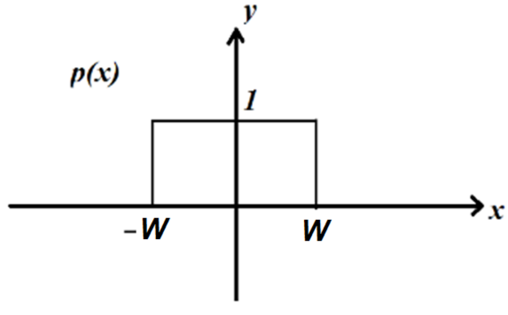

Figure 5.1 Pulse function whose amplitude is '1' and width is 2W.

Let us assume the Fourier transform of this pulse function $\tilde{p}(k_x)$, it is found as below:

$$\tilde{p}(k_x) = \int_{-\infty}^{\infty} p(x) \cdot e^{jk_x x} dx = \int_{-W}^{W} e^{jk_x x} dx = 2W \frac{\sin k_x W}{k_x W} = 2W \mathrm{sinc}(k_x W), \tag{5.2}$$

Then the convolution of these two pulse functions in spectral-domain is given by:

$$\tilde{t}(k_x) = \tilde{p}(k_x) \cdot \tilde{p}(k_x) = (2W)^2 (\mathrm{sinc}(k_x W))^2 \tag{5.3}$$

where $\tilde{t}(k_x)$ is the Fourier transform of *t(x)*. The first convolution is taken with two pulse function, and it produces a triangular function *t(x)* having *4W* width. The second one is taken with these triangular functions and yields a new function *q(x)* in space as given $q(x) = t(x) * t(x)$. This is a smooth signal having the pulse width of *8W*, and the Fourier transform of *q(x)* can easily be derived mathematically as follows:

$$\tilde{q}(k_x) = \tilde{t}(k_x) \cdot \tilde{t}(k_x) = (2W)^4 (\mathrm{sinc}(k_x W))^4 \tag{5.4}$$

The original function *q(x)* can be generated by using the following inverse Fourier transform integral:

$$q(x) = \frac{1}{2\pi} \int_{-\infty}^{+\infty} \frac{P_0(k_y)}{k_y} e^{-jk_x x} dk_x \tag{5.5}$$

where $P_0(k_y) = \tilde{q}(k_x) k_y$ is the spectral domain function and $k_y = \sqrt{k^2 - k_x{}^2}$. The purpose is to relate the function *q(x)* with the Hankel function to constitute a new Green's function. Note that the Hankel function of the second kind used in 2D scattering formulation can be represented by Sommerfeld's identity as follows:

$$H_0{}^{(2)}(k\rho) = \frac{1}{\pi} \int_{\substack{-\infty \\ SIP}}^{+\infty} \frac{e^{-jk_x x}}{k_y} e^{-jk_y |y|} dk_x \tag{5.6}$$

where $\rho = \sqrt{x^2 + y^2}$. Then $P_0(k_y)$ can be expanded into a finite series of exponents by using the GPOF technique. It can be approximated by the complex exponentials as the following serial form:

$$P_0(k_y) \cong \sum_{s=1}^{M} d_s e^{-\beta_s k_y} \tag{5.7}$$

where *M* is the total number of exponentials used in the approximation, d_s is the complex residues, and β_s is the complex poles. To determine the coefficients d_s and β_s from the GPOF method, $P_0(k_y)$ is sampled at any interval of $0<t<T_0$, where T_0 is the

maximum sampling interval. The coefficients are found in compliance with $k_y = k_0 [- jt + (1 - t/T)]$ on a deformed path called Sommerfeld Integration Path (SIP) (Chow et al., 1991). Matching equations (5.1) and (5.7), the coefficients are derived for the spectral domain function:

$$d_s = c_s e^{\beta_s k_0} \tag{5.8a}$$

$$\beta_s = \frac{w_s T}{k_0 (1 + jT)} \tag{5.8b}$$

The coefficients c_s and w_s obtained from GPOF method, are then substituted in the definition of *q(x)*:

$$q(x) \cong \sum_{s=1}^{M} d_s \frac{1}{2\pi} \int_{\substack{-\infty \\ SIP}}^{\infty} \frac{e^{-\beta_s k_y}}{k_y} \cdot e^{-jk_x x} dk_x \tag{5.9}$$

Matching equations (5.6) and (5.9) by assuming $\beta_s = j|y|$, *q(x)* becomes the new Green's function in terms of a serial form of Hankel functions:

$$q(x) \cong \frac{1}{2} \sum_{s=1}^{M} d_s H_0^{(2)}(k\sqrt{x^2 - \beta_s^2}) \tag{5.10}$$

This serial form of the Hankel function is the radiated field representation of various line current sources with different complex source coordinates. It also satisfies all the conditions of the uniqueness theorem so that a unique field distribution is valid. Equation (5.10) is a very close approximation of the *q(x)* function on the *y* = 0 plane. The spatial width of the *q(x)* can be assigned smaller than a beam width in CSP type Green's function (Kutluay & Oğuzer, 2019). It can be narrowed down the pulse width covering two basis function levels and still provides the correct scattered patterns under these conditions.

The new modified Green's function defined in (5.10) is also expressed as the convolution of two triangular functions expressed at the very beginning in this chapter, and it is defined as:

$$z(x)=\begin{cases} 1/6\left(\dfrac{x^3}{(2W)^2}+\dfrac{6x^2}{2W}+12x+16W\right) & -4W\le x<-2W \\ 1/6\left(\dfrac{-3x^3}{(2W)^2}-\dfrac{6x^2}{2W}+8W\right) & -2W\le x<0 \\ 1/6\left(\dfrac{3x^3}{(2W)^2}-\dfrac{6x^2}{2W}+8W\right) & 0\le x<2W \\ 1/6\left(\dfrac{-x^3}{(2W)^2}+\dfrac{6x^2}{2W}-12x+16W\right) & 2W\le x<4W \end{cases} \tag{5.11}$$

For the computational cost in PC, this convolution *z(x)* should be used to obtain the solution of the current density function. However, since the far zone approximations are used in the determination of the radiation characteristics, the Hankel function definition of *q(x)* should be used in the derivation of the scattering pattern, which is equation (5.10). The new modified Green's function G_{gpof} is defined as follows:

$$G_{gpof}(\vec{x}-\vec{x}')=\frac{-j}{4}\begin{cases} H_0^{(2)}\left(k\sqrt{(x-x')^2}\right), & x' \text{ is at the near edge region} \\ \tilde{C}\sum_{s=1}^{M} d_s H_0^{(2)}\left(k\sqrt{(x-x')^2-\beta_s^2}\right), & x' \text{ is at the non-near edge region} \end{cases} \tag{5.12}$$

where $\tilde{C}$ is a real constant to fix the two definitions of *q(x)* and *z(x)*, equation (5.10) and (5.11). It is used in solutions both current density function and RCS results to match the amplitude levels of the functions *q(x)* and *z(x)*.

It is assigned the parameters $W = 0.025$, $M = 12$, $T = 17$, time interval $\delta t = 0.0122$, so t = 0:0.0122:T. As a result, it is achieved c_s and w_s from the GPOF method, then substitute them for obtaining d_s and β_s, as explained above. The function *q(x)* with these parameters or the new modified Green's function G_{gpof} for the non-near edge regions and convolution function *z(x)* are plotted in the same figure as shown below:

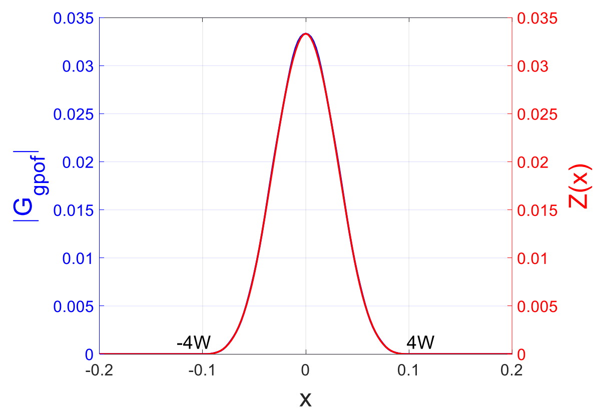

Figure 5.2 The beam-pattern function q(x) obtained from GPOF method

The modified Green's function has a beam nature, and it is the exact solution of the Helmholtz Equation; additionally, it satisfies the radiation condition. In the solution to the problem, BC on the structure must also be applied. The only remaining term is EC, and it is coming from the edge regions. For avoiding the EC violation, the free-space Green's function is implemented in the near edge region. Note that the distance parameter α should be equal or greater than the beam aperture width, which is the pulse width of the G_{gpof} function. So it must be equal to 8W or greater.

This beam-pattern function will be used as a new Green's function for more localization than the CSP type Green's function. When it is used in the non-near edge regions, modified Green's function enables a decline severely in the interaction of the main matrix elements since the width of the function is narrower form.

5.2 2D Scattering from a Large PEC Strip

5.2.1 MoM Procedure with Modified Green's Function by Using GPOF Method

The exception of which Green's function is employed, the procedure is the same performed in section 4.2.1 for 2D PEC strip for both polarizations. The modified Green's function by using the GPOF method is utilized instead of the CSP type Green's function. EM scattering from PEC strip, as shown in Figure 5.3 can be written with a modified Green's function by using GPOF method, and EFIE is as follows:

$$E_z^{inc} = jk\eta \int_0^L J_z^{gpof}(\vec{x}')G_{gpof}(\vec{x}-\vec{x}')d\vec{x}' \tag{5.13}$$

Here $J_z^{gpof}(\vec{x}')$ is the unknown current density function different from the physical current on the strip. Similar to the previous sections, the unknown function is expanded by the pulse basis functions $p(x)$ with unknown coefficients a_n, $n = 1, 2\ldots N$ as MoM procedure. The incident field is assumed as the same E-polarized EM plane wave as $E_z^{in} = e^{jk(x\cos\phi^{in} + y\sin\phi^{in})}$. Then, the Galerkin technique is applied with pulse function $p_m(x)$ to obtain the following algebraic matrix equation:

$$\int_{x_m-\Delta/2}^{x_m+\Delta/2} p_m(x)E_z^{in}(x)dx = jk\eta\sum_{n=1}^{N} a_n \int_{x_m-\Delta/2}^{x_m+\Delta/2} p_m(x) \int_{x_n-\Delta/2}^{x_n+\Delta/2} p_n(x')G_{gpof}(\vec{x}-\vec{x}')dx'dx \tag{5.14}$$

$$\text{m} = 1,2,\ldots\text{N}$$

Equation (5.14) is a matrix equation for the given problem, so the main matrix and excitation vector can be written as:

$$Z_{mn} = \frac{k\eta}{4}\sum_{s=1}^{M} d_s \int_{x_m-\Delta/2}^{x_m+\Delta/2} p_m(x) \int_{x_n-\Delta/2}^{x_n+\Delta/2} p_n(x')H_0^{(2)}(k\sqrt{(x-x')^2-\beta_s{}^2}dx'dx \tag{5.15}$$

$$g_m = \int_{x_m-\Delta/2}^{x_m+\Delta/2} p_m(x)e^{jkx\cos\phi^{in}}dx \tag{5.16}$$

Equation (5.15) and (5.16) are matrices for *the MoM Procedure with Modified Green's Function* solution by using the GPOF method.

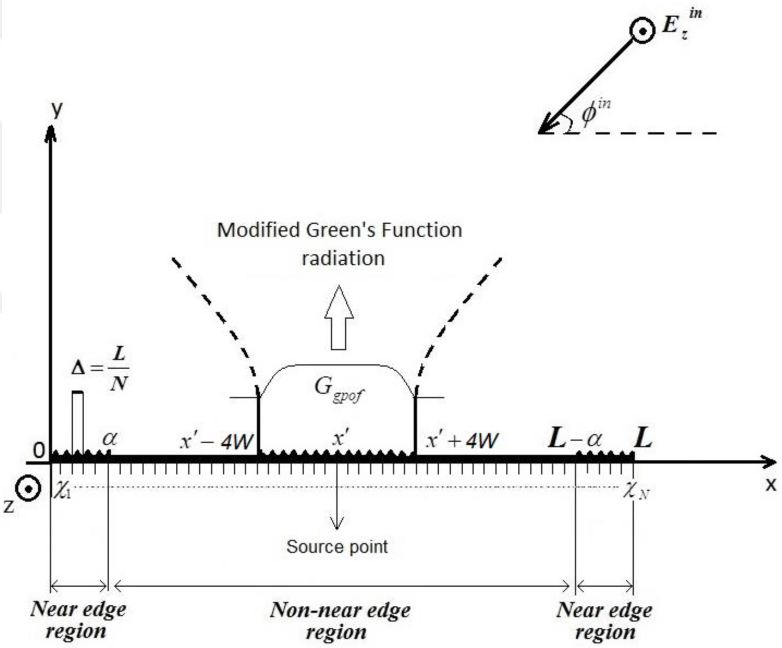

Figure 5.3 Geometry of the finite width 2D PEC strip with E-polarized incident field

For the H-polarization case, the incident field is assumed as a plane wave as $H_z^{in} = e^{jk(x\cos\phi^{in}+y\sin\phi^{in})}$. Applying the Galerkin method with triangular basis functions $t(x)$, the current density is again expanded with the unknown coefficients; a_n's, $n = 1,2\ldots N\text{-}1$ to generate the following matrix equation:

$$\int_{\chi_m-\Delta}^{\chi_m+\Delta} t_m(x)E_x^{in}(x)dx = +jk\eta\sum_{n=1}^{N-1} a_n \int_{\chi_m-\Delta}^{\chi_m+\Delta} t_m(x) \int_{\chi_n-\Delta}^{\chi_n+\Delta} t_n(x')G_{gpof}(\vec{x}-\vec{x}')dx'dx$$
$$-\frac{j\eta}{k}\sum_{n=1}^{N-1} a_n \int_{\chi_m-\Delta}^{\chi_m+\Delta} \frac{\partial t_m(x)}{dx} \int_{\chi_n-\Delta}^{\chi_n+\Delta} \frac{\partial t_n(x')}{dx'} G_{gpof}(\vec{x}-\vec{x}')dx'dx \tag{5.17}$$
$$m = 1,2,\ldots N-1$$

The half-pulse width of G_{gpof} is 4W, and so it may be as small as 0.1λ. This width means that there would be very limited interactions between the source and observation points far from each other as 0.2λ. In this way, most of the interactions between the elements in the impedance matrix turn to zero, and it produces a strongly localized sparse matrix. This is the key point of the presented hybrid method. More localization is proposed with this technique because the beamwidth of 0.2λ is much narrower than the parameter "*b*" in CSP type localization.

The magnitude level mapping of the main matrix is like a form, as shown in Figure 5.4 for L = 10λ, the discretization criterion Δ = 0.1λ and α = 0.5λ. The conventional MoM in the E-pol case has a dense matrix (See Figure 5.4a), but as shown in Figure 5.4b, the main impedance matrix is in the sparse form indicated by white parts in the mapping as zero magnitudes. In the H-pol case, the conversion in the main matrix has the same features, just like in E-pol, and the magnitudes of the main matrix elements are shown in Figure 5.4c and Figure 5.4d. The higher localization between the hybrid methods is noticeable and seen when compared to Figure 5.4 with Figure 4.5.

5.2.2 Determination of the Radiation Characteristics under the Modified Green's Function

After the numerical solution of the matrix equation (5.14), a non-real current density function is obtained. To plot the far-field RCS scattering for the given problem, the large asymptotic argument of the Hankel function is employed in the modified Green's function G_{gpof}. In the derivation of the modified Green's function, it was required $\beta_s = j|y|$, which is needed to use in the large asymptotic argument of the Hankel function for radiation characteristics. Then, a physical representation for the complex source vector can be written by using the fact $\beta_s = j|y|$:

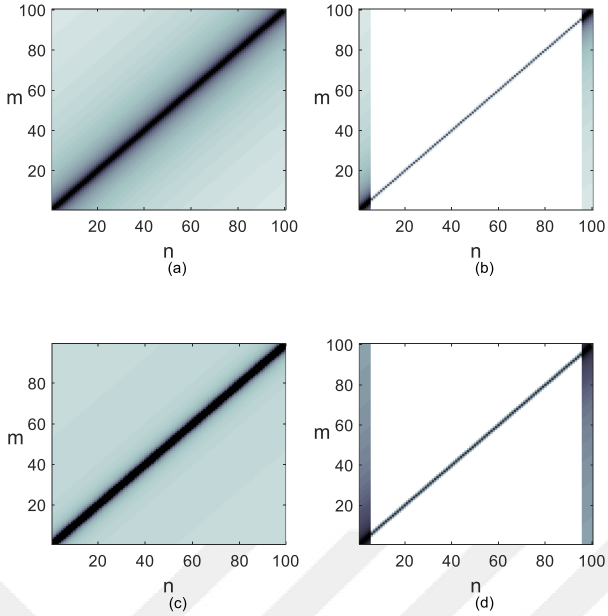

Figure 5.4 The magnitude level of the impedance matrix elements for L = 10λ, Δ = 0.1λ and α = 0.5λ (a) standard MoM and (b) the proposed method for E-pol. (c) standard MoM, and (d) the proposed method for H-pol

$$\vec{r}'_{gpof} = x'\hat{x} - j\beta_s \hat{y} \tag{5.18}$$

The far-field approximations for the proposed method are $R_{gpof} \cong r - \vec{r}'_{gpof} \cdot \hat{r}$ in phase term and $R_{gpof} \cong r$ in amplitude term. If equation (5.18) is substituted in the large argument of the Hankel function, we get:

$$\lim_{R_{gpof} \to \infty} H_0^{(2)}(kR_{gpof}) = \sqrt{\frac{2j}{\pi kr}} e^{-jk(r - x'\cos\phi + j\beta_s \sin\phi)} \tag{5.19}$$

Then, the far zone electric field scattered from the strip can be written as:

$$\begin{aligned} E_z^{sc} &= -\frac{k\eta}{4} \int_L J_z(x') H_0^{(2)}(kR_{gpof}) dx' \\ &= -\sqrt{\frac{2j}{\pi kr}} \cdot e^{-jkr} \underbrace{\left(k\eta/4\right) \sum_{n=1}^{N} a_n \overline{\beta}_n(\phi) \int_{x_n - \Delta/2}^{x_n + \Delta/2} p_n(x') e^{jkx'\cos\phi} dx'}_{\psi^7(\phi)} \end{aligned} \tag{5.20}$$

where

$$\overline{\beta}_n(\phi) = \begin{cases} 1, & \text{n is at the near edge region} \\ \sum_{s=1}^{M} d_s e^{k\beta_s \sin\phi}, & \text{n is at the non - near edge region} \end{cases} \tag{5.21}$$

Furthermore, $\psi^7(\phi)$ is the scattering pattern for *the MoM Procedure with Modified Green's Function* solution by using the GPOF method in the E-pol case. The bistatic RCS can be given as:

$$\sigma = 2\pi r \frac{\left|E_z^{sc}\right|^2}{\left|E_z^{in}\right|^2} = \frac{4}{k}\left|\psi^7(\phi)\right|^2 \tag{5.22}$$

Similarly, for the H-pol case, a non-real current density function is obtained from equation (5.17). The far zone magnetic field scattered from the strip was derived in section 4.2.2.1 for the MoM and the first hybrid technique. In parallel to the derivations from (4.47) to (4.51), and using the large argument of the Hankel function (5.19), the far zone scattered magnetic field can be written as:

$$H_z^{sc} = -\sqrt{\frac{2j}{\pi kr}} e^{-jkr} \underbrace{(k/4)\sin\phi \sum_{n=1}^{N-1} a_n \bar{\beta}_n(\phi) \int_{\chi_n-\Delta}^{\chi_n+\Delta} t_n(x') e^{jkx'\cos\phi} dx'}_{\psi^8(\phi)} \tag{5.23}$$

where $\psi^8(\phi)$ is the scattering pattern for *the MoM Procedure with Modified Green's Function* solution by using the GPOF method in the H-pol case. Then, the bistatic RCS is given by:

$$\sigma = 2\pi r \frac{\left|H_z^{sc}\right|^2}{\left|H_z^{in}\right|^2} = \frac{4}{k}\left|\psi^8(\phi)\right|^2 \tag{5.24}$$

It should be noticed that if $\bar{\beta}_n = 1$ at the near edge regions, the scattering patterns $\psi^7(\phi)$ and $\psi^8(\phi)$ for the proposed method is equal to the scattering patterns for MoM solution, $\psi^7(\phi) = \psi^1(\phi)$ in (4.43) and $\psi^8(\phi) = \psi^3(\phi)$ in (4.51).

5.2.3 Numerical Results

The proposed method has been applied with the modified Green's function G_{gpof}. The parameter α is assigned 0.5λ to define the size of the near edge regions while the total length of the strip is L = 10λ and L = 50λ for perpendicular incidence angle. Here, the sparsity of the resultant matrix is exceptionally high because near edge regions are very limited to a few basis functions. To compare the presented method with the standard MoM, the RE is defined as below:

$$\tilde{\varepsilon} = \sqrt{\sum_{n=1}^{N} \left| e^{mom} - e^{\text{mod}} \right|^2} \cdot \left(\sqrt{\sum_{n=1}^{N} \left| e^{mom} \right|^2} \right)^{-1} \tag{5.25}$$

where e^{mom} is the solution for the conventional MoM, and e^{mod} is the solution for *the MoM procedure with modified Green's function* by using the GPOF method.

In Figure 5.5, the true surface current density and the pseudo-current density function obtained from the proposed procedure are shown on the same plot for both polarizations. The blue line is the real current density obtained from the standard MoM, and the red line is the pseudo-current function from the proposed method for the strip width $L = 10\lambda$ and $\phi^{in} = 90^o$. As expected, the edge effects present similarly on the edge regions like in the first method. However, since α is assigned smaller than in the first method, current density functions tend to be similar in the narrower region, such as 0.5λ for both polarizations.

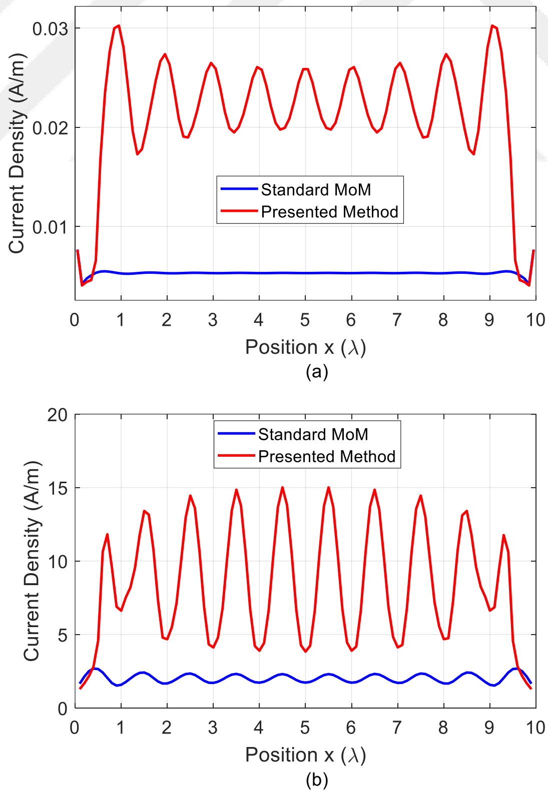

Figure 5.5 Current density examination for L = 10λ and $\phi^{in} = 90^o$, (a) E-pol and (b) H-pol

In Figure 5.6, the normalized RCS is demonstrated for two strip widths for E-pol case. It is obtained similar to the standard MoM with RE 0.31% and 0.67% for L = 10λ and L = 50λ, respectively. In Figure 5.7, the normalized RCS is shown for the H-pol case and the same sizes of the strip. In parallel to the E-pol case, remarkable outcomes are found for the H-pol case with RE 0.11% and 0.43%.

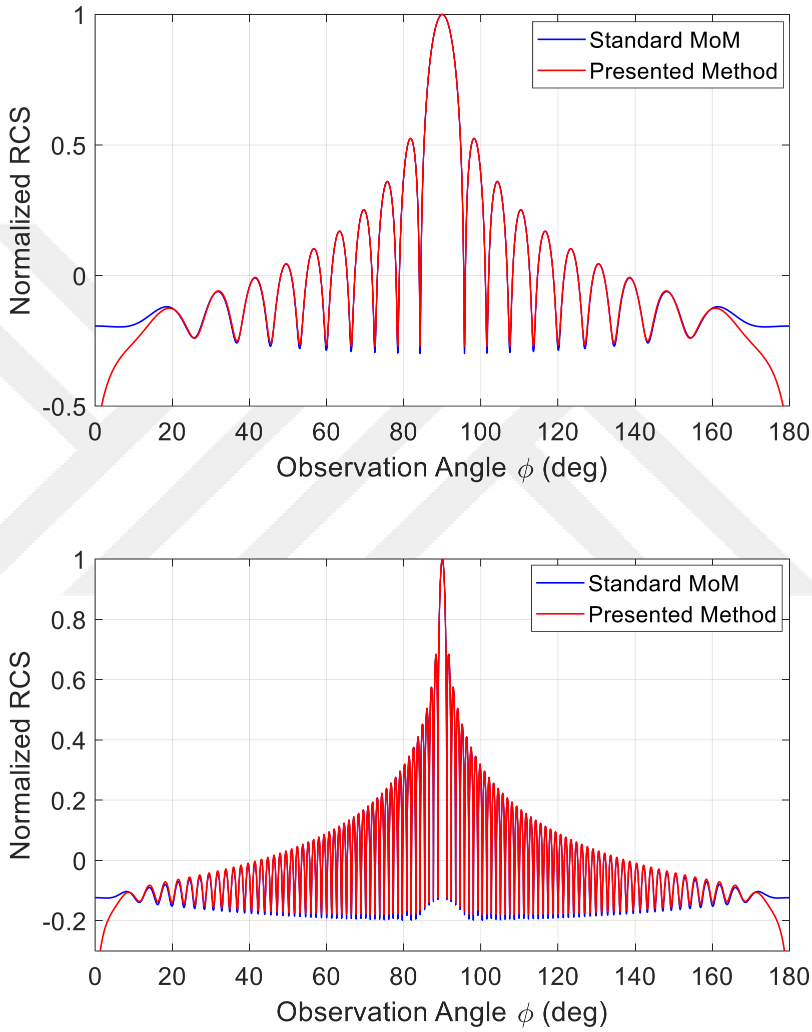

Figure 5.6 Normalized RCS pattern comparison between standard MoM and proposed method for E-pol, $\phi^{in} = 90^o$ and α = 0.5λ, 4W = 0.1λ (a) L = 10λ (b) L = 50λ

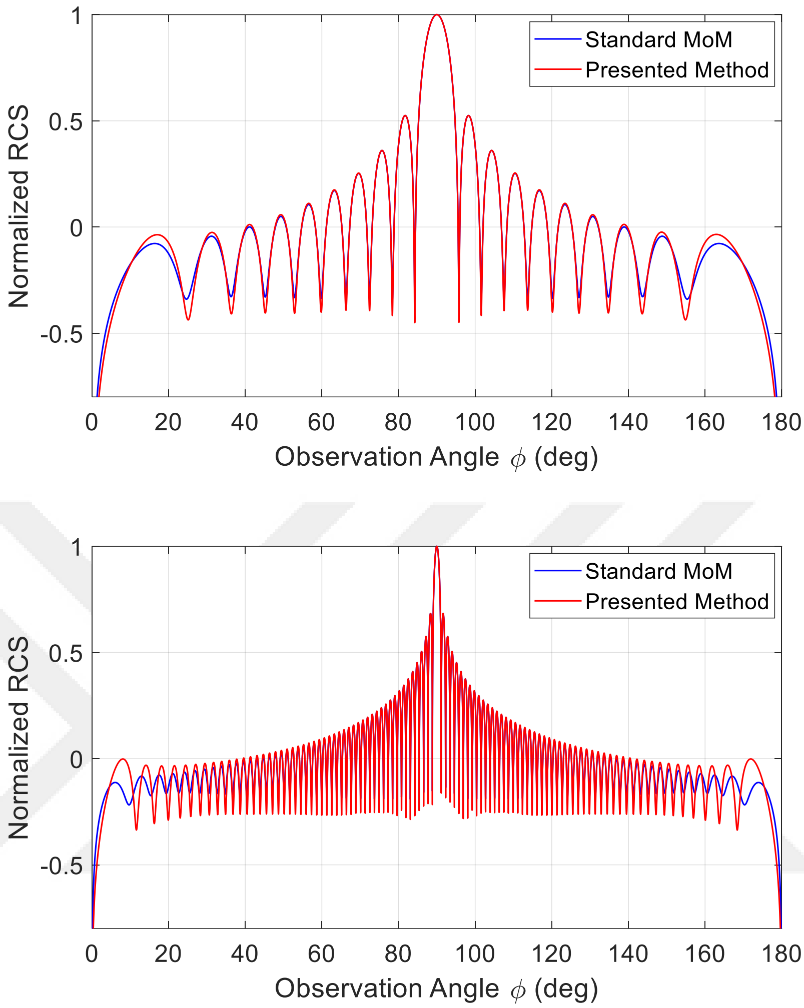

Figure 5.7 Normalized RCS pattern comparison between standard MoM and proposed method for H-pol, ϕ^{in} = 90º, and α = 0.5λ, 4W = 0.1λ (a) L = 10λ (b) L = 50λ

After the successful presentation of numerical results for the perpendicular incidence, it is next tested for the incidence angle of 30º. Some significant results are found for both polarizations, for ϕ^{in} = 30º and L = 20λ, as illustrated in Figure 5.8. The REs are 1% for E-polarization and 4.5% for H-polarization. It can be said that the RCS values become larger for the near grazing incidence illuminations for the H-pol case in this method.

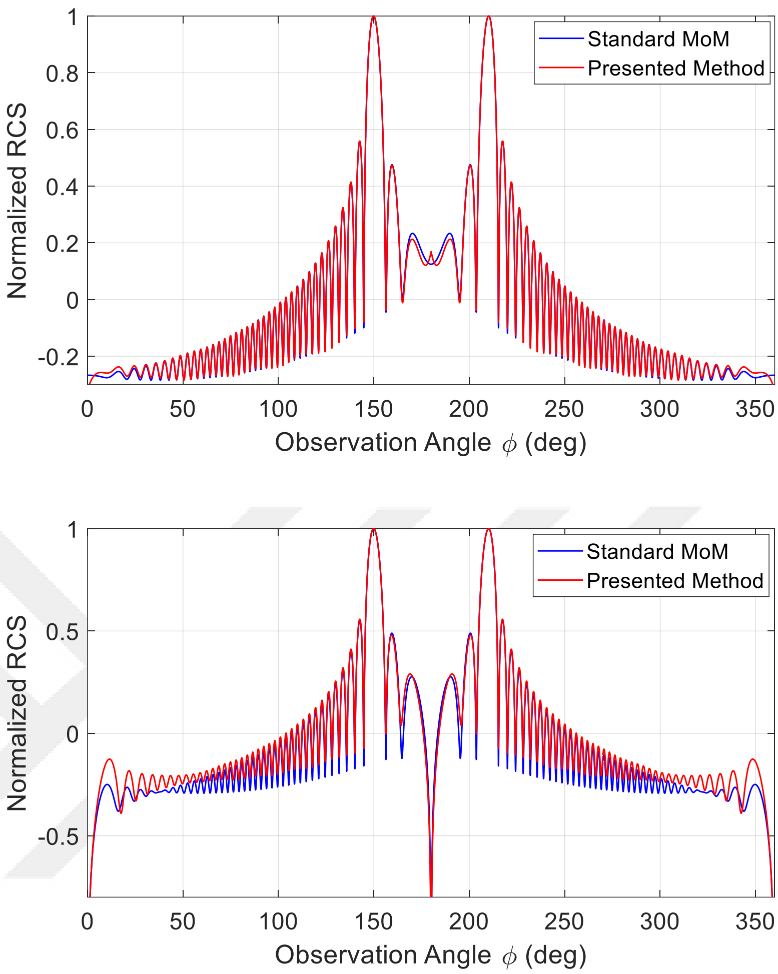

Figure 5.8 Normalized RCS pattern comparison between standard MoM and proposed method for both polarizations, ϕ^{in}=30°, L = 20λ and α = 0.5λ, 4W = 0.1λ (a) E-pol (b) H-pol

In the numerical simulations of (Kutluay & Oğuzer, 2017), the condition number of the main matrix is around 10^6. In contrast to that one, here, the proposed modified Green's function provides us with a reasonable condition number around 10^4 that makes the approach more attractive. This decrease is even valid for the larger strip size, and so there can be a possibility to apply it to more complicated 2D geometries.

Besides, another main criterion is related to the overall running times. Table 5.1 and Table 5.2 introduce the time gain of the solution only for founding the current density function. Since the main impedance matrices have higher localization than the CSP type Green's function (Kutluay & Oğuzer, 2017), the memory storages and the

CPU times reduce notably. Therefore, the larger sizes can be modeled by smaller storages of memory. In this direction, it has been analyzed PEC strips for both polarizations and perpendicular incidence angle. Table 5.1 and Table 5.2 show the time gain in the solution with REs.

For the MoM and the presented method, the Toeplitz property develops the overall running times for the solution of the strip geometry. REs have been computed 0.65% in E-pol and 0.41% in H-pol for all strip size up to 3000λ. This size is the limit for our computer for the standard MoM due to the memory requirement.

It has also been pointed out the memory storage requirements for all strip sizes in Table 5.1, following the λ/10 discretization criterion. Although the memory usage is limited to solve in the standard MoM for larger than 3000λ strip size, the presented method is suitable for analyzing with the strip size of 50000λ with perfect solution time.

The memory storage and the operation count are reduced significantly by applying this localized radiation of Green's function. Therefore, it offers an opportunity to analyze larger geometries with shorter running times because the total number of unknowns does not increase excessively with the size of the strip.

Table 5.1 CPU Time and memory storage comparison (E-pol)

Strip Length (λ)	**Incident angle (degree)**	**Solution Time For E-pol (seconds)**		**Memory Storage**		***Relative Error (%)***
		MoM	***Presented method***	***MoM (N x N)***	***Presented method (14N)***	
L=500	90	4	1	$25 \cdot 10^{6}$	$0.07 \cdot 10^{6}$	0.65
L=1000	90	25	1	$100 \cdot 10^{6}$	$0.14 \cdot 10^{6}$	0.65
L=2000	90	182	2	$400 \cdot 10^{6}$	$0.28 \cdot 10^{6}$	0.65
L=3000	90	661	3	$900 \cdot 10^{6}$	$0.42 \cdot 10^{6}$	0.65
L=5000	90	-	5	$2.5 \cdot 10^{9}$	$0.7 \cdot 10^{6}$	-
L=10000	90	-	9	$1 \cdot 10^{10}$	$1.4 \cdot 10^{6}$	-
L=50000	90	-	51	$2.5 \cdot 10^{11}$	$7 \cdot 10^{6}$	-

Table 5.2 CPU Time and memory storage comparison (H-pol)

Strip Length (λ)	**Incident angle (degree)**	**Solution Time For H-pol (seconds)**		**Memory Storage**		***Relative Error (%)***
		MoM	***Presented method***	***MoM (N x N)***	***Presented method (14N)***	
L=500	90	4	1	$25{\cdot}10^{6}$	$0.07{\cdot}10^{6}$	0.41
L=1000	90	24	1	$100{\cdot}10^{6}$	$0.14{\cdot}10^{6}$	0.41
L=2000	90	181	2	$400{\cdot}10^{6}$	$0.28{\cdot}10^{6}$	0.41
L=3000	90	638	3	$900{\cdot}10^{6}$	$0.42{\cdot}10^{6}$	0.41
L=5000	90	-	5	$2.5{\cdot}10^{9}$	$0.7{\cdot}10^{6}$	-
L=10000	90	-	10	$1{\cdot}10^{10}$	$1.4{\cdot}10^{6}$	-
L=50000	90	-	57	$2.5{\cdot}10^{11}$	$7{\cdot}10^{6}$	-

5.3 2D Scattering from A Large PEC Polygon Cylinder with N-Sided Convex Cross-Section

5.3.1 MoM Procedure with Modified Green's Function by Using GPOF Method

The geometry is the same with the PEC polygonal cylinder with N-sided convex cross-section, as shown in Figure 4.14, illuminated by an EM plane wave of one of two polarizations. The parameter α equals to the same definition, which is the near edge region's width.

5.3.1.1 E-polarization

In parallel to the previous sections, the EFIE can be depicted for this geometry with modified Green's function as below:

$$E_z^{inc} = jk\eta \int_{Ct} J_z^{gpof}(\vec{r}')G_{gpof}(\vec{r}-\vec{r}')d\ell' \tag{5.26}$$

It can be seen that there is an analogy between the first and the second hybrid method. The definitions of complex source vectors, $\vec{r}'_{csp}$ and $\vec{r}'_{gpof}$ are identical except their complex quantities. Amplitude derivations in the Hankel function of Green's function for each method are found by making the same operations. Therefore, the modified Green's function depends on the source position is described as follows:

$$G_{gpof}(\vec{r}-\vec{r}') = \frac{-j}{4}\begin{Bmatrix} H_0^{(2)}(k\sqrt{(\tilde{x}_m-\tilde{x}'_n)^2+(\tilde{y}_m-\tilde{y}'_n)^2}, & \text{r}' \text{ is at the near edge region} \\ \overline{C}\sum_{s=1}^{M} d_s H_0^{(2)}(k\sqrt{((\tilde{x}_m-\tilde{x}'_n)^2+(\tilde{y}_m-\tilde{y}'_n)^2-\beta_s^{\,2}}, & \text{r}' \text{ is at the non-near edge region} \end{Bmatrix}$$

(5.27)

This is the same coordinate transformation from *(x,y)* to (ℓ,φ) defined in the previous chapter for E-pol case. Applying Galerkin's procedure with the pulse basis functions, the following matrix equation can be written for E-pol:

$$\int_0^{\Delta_m} p_m(\ell)\cdot E_z^{\,in}(\ell)d\ell = jk\eta\sum_{n=1}^{N} a_n \int_0^{\Delta_m} p_m(\ell)\int_0^{\Delta_n} p_n(\ell')G_{gpof}(\tilde{x}_m-\tilde{x}'_n,\tilde{y}_m-\tilde{y}'_n)d\ell' d\ell \qquad (5.28)$$

m=1,2,….N

Then the unknown current density function in (5.26) is found from the matrix form of the above equation.

5.3.1.2 H-polarization

In H-pol, Galerkin's procedure is applied with the triangular basis functions. In parallel to (4.77) for this geometry, the EFIE is obtained as follows:

$$\begin{aligned} &\int_0^{\Delta_m^-+\Delta_m^+} t_m(\ell)(\hat{\ell}_m\cdot\vec{E}_\ell^{\,in}(\ell)d\ell = \\ &jk\eta\sum_{n=1}^{N} a_n \int_0^{\Delta_m^-+\Delta_m^+}\int_0^{\Delta_n^-+\Delta_n^+}(\hat{\ell}_m\cdot\hat{\ell}'_n)t_m(\ell)t_n(\ell')G_{gpof}(\overline{x}_m-\overline{x}'_n,\overline{y}_m-\overline{y}'_n,b_n)d\ell' d\ell \\ &-\frac{j\eta}{k}\sum_{n=1}^{N} a_n \int_0^{\Delta_m^-+\Delta_m^+}\frac{\partial t_m(\ell)}{\partial\ell}\int_0^{\Delta_n^-+\Delta_n^+}\frac{\partial t_n(\ell')}{\partial\ell'}G_{gpof}(\overline{x}_m-\overline{x}'_n,\overline{y}_m-\overline{y}'_n,b_n)d\ell' d\ell \end{aligned} \qquad (5.29)$$

m=1,2,….N

Here, it is the same coordinate transformation from *(x,y)* to (ℓ,φ), as defined in the previous chapter for the H-pol case.

5.3.2 Determination of the Radiation Characteristics

Owing to the analogy between the proposed methods mentioned earlier, derivations for scattering patterns are similar to each other. Therefore, after finding the current density function of the method, in E-pol, the far zone scattered electric field from the cylinder can be written as:

$$E_z^{sc} = -\sqrt{\frac{2j}{\pi kr}} e^{-jkr} \underbrace{(k\eta/4)\sum_{n=1}^{N} a_n \widetilde{\beta}_n(\phi,\varphi_n') \int_0^{\Delta_n} p_n(\ell') e^{jk[\widetilde{x}_n' \cos\phi + \widetilde{y}_n' \sin\phi]} d\ell'}_{\psi^3(\phi)} \tag{5.30}$$

where $\psi^3(\phi)$ is the scattering pattern. The bistatic RCS is given by:

$$\alpha = 2\pi r \frac{\left|E_\ell^{sc}\right|^2}{\left|E_\ell^{in}\right|^2} = \frac{4}{k}\left|\psi^3(\phi)\right|^2 \tag{5.31}$$

In H-pol, the far zone scattered magnetic field from the cylinder is as follows:

$$H_z^{sc} = \sqrt{\frac{2}{j\pi kr}} e^{-jkr} \underbrace{(-k/4)\sum_{n=1}^{N} a_n \widetilde{\beta}_n(\phi,\varphi_n') \int_0^{\Delta_n^- + \Delta_n^+} t_n(\ell') \sin(\varphi_n' - \phi) e^{jk(\overline{x}_n' \cos\phi + \overline{y}_n' \sin\phi)} d\ell'}_{\psi^4(\phi)} \tag{5.32}$$

The bistatic RCS is given by:

$$\alpha = 2\pi r \frac{\left|H_\ell^{sc}\right|^2}{\left|H_\ell^{in}\right|^2} = \frac{4}{k}\left|\psi^4(\phi)\right|^2 \tag{5.33}$$

where

$$\widetilde{\beta}_n(\phi,\varphi_n') = \begin{cases} 1, & \text{n is at the near edge region} \\ \sum_{s=1}^{M} d_s e^{k\beta_s \sin(\varphi_n' - \phi)}, & \text{n is at the non - near edge region} \end{cases} \tag{5.34}$$

5.3.3 Numerical Results

Square and triangle cross-sectional PEC cylinders have been reviewed in both polarisations, and RCS results are presented in the following parts.

5.3.3.1 Square Cross-Sectional PEC Cylinder Geometry

Here, the square shape of a PEC cylinder cross-section is researched with a side width of 25λ. The incidence angle is assumed as $\phi^{in} = 45^o$ for both polarisations. In Figure 5.9, the obtained bistatic RCS results have been plotted for both polarisation cases. The outcomes are remarkable agreement with the MoM, and REs are minimal values such as 0.13% for E-pol case and 0.68% for H-pol case.

The pulse width of the G_{gpof} function is designated as 0.4λ by taking $4W = 0.2\lambda$ for the H-pol case as in parallel of the explanation for the selection of beamwidth parameter b in part 4.2.3. Also, as explained in section 4.2.3, the designation of near-edge regions width can only affect the minor lobes in the RCS result. As in the first hybrid technique, it is not crucial what the distance parameter α is chosen unless it is less than the beam aperture width. Therefore, it can be assigned equal or greater of 0.4λ when $4W = 0.2\lambda$. Different designations in the distance parameter α only aim to present accurately minor lobes in RCS results.

Figure 5.10 represents the obtained bistatic RCS for the incidence angle $\phi^{in} = 90^{o}$ and $L = 25\lambda$ for both polarisations. As explained in the previous chapter, RE has been found a little higher than the incidence angle case $\phi^{in} = 45^{o}$ for E-pol case due to the incident angle.

Like in the previous chapter, the method has been investigated with a facet of square $L = 250\lambda$ and incidence angle $\phi^{in} = 45^{o}$ for both polarizations. As indicated in the previous chapter, since the edge effects are less critical, it is chosen $\alpha = 0.5\lambda$ when the geometry becomes larger. In Figure 5.11, remarkable RCS results have been obtained with REs 0.03% for E-pol and 0.14% H-pol.

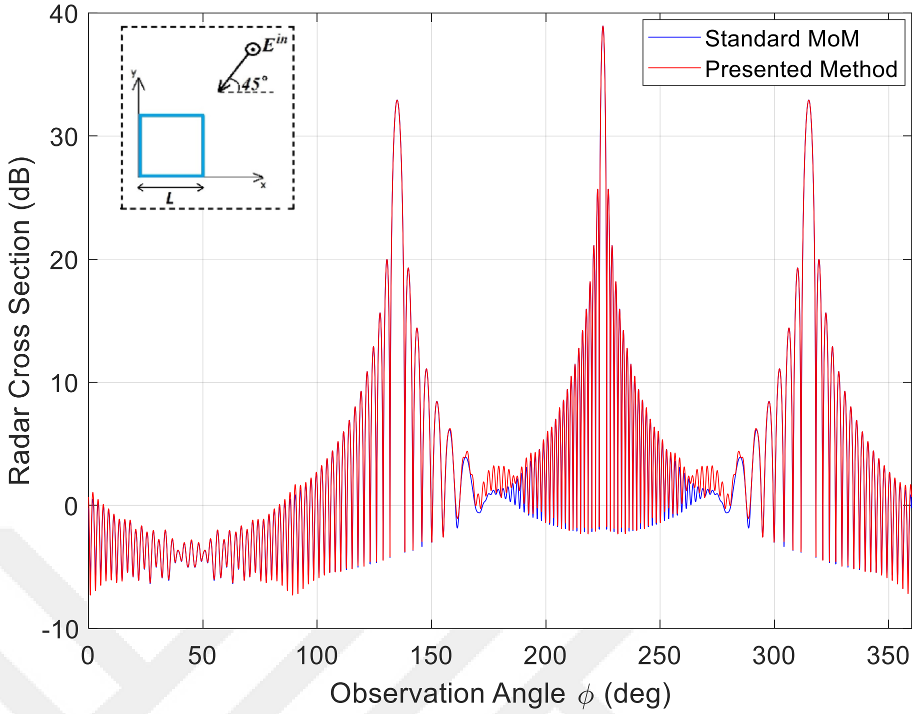

(a) E-pol case, α = 2λ, 4W = 0.1λ, and RE = 0.13%

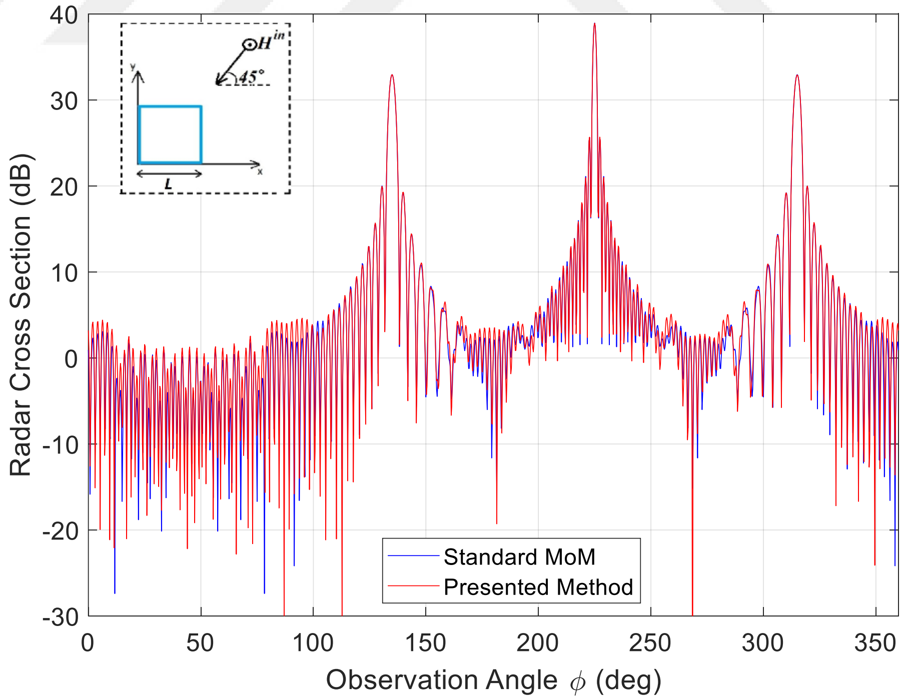

(b) H-pol case, α = 2λ, 4W = 0.2λ, and RE = 0.68%

Figure 5.9 RCS pattern comparison between the standard MoM and the proposed method for L = 25λ, $\phi^{in} = 45^o$

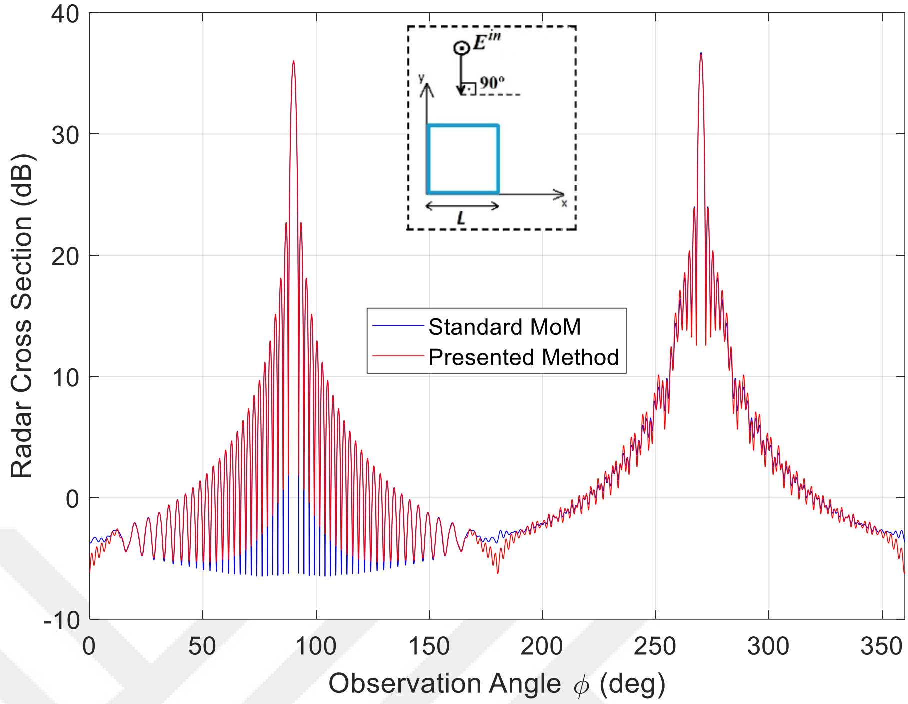

(a) E-pol case, α = 2.5λ, 4W = 0.1λ, and RE = 2.21%

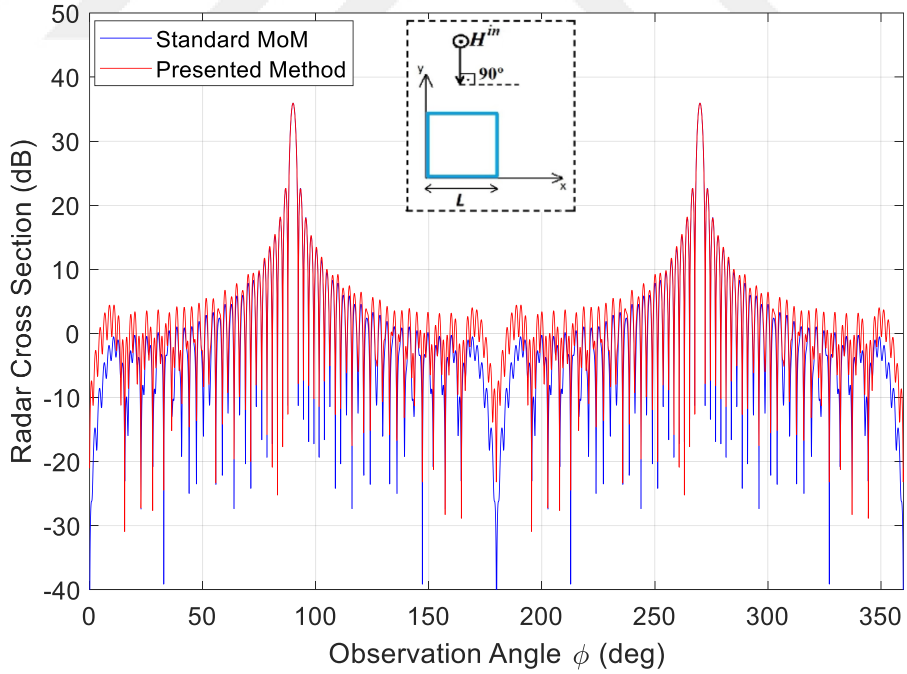

(b) H-pol case, α = 2.5λ, 4W = 0.2λ, and RE = 0.44%

Figure 5.10 RCS pattern comparison between the standard MoM and the proposed method for L = 25λ, $\phi^{in} = 90^o$

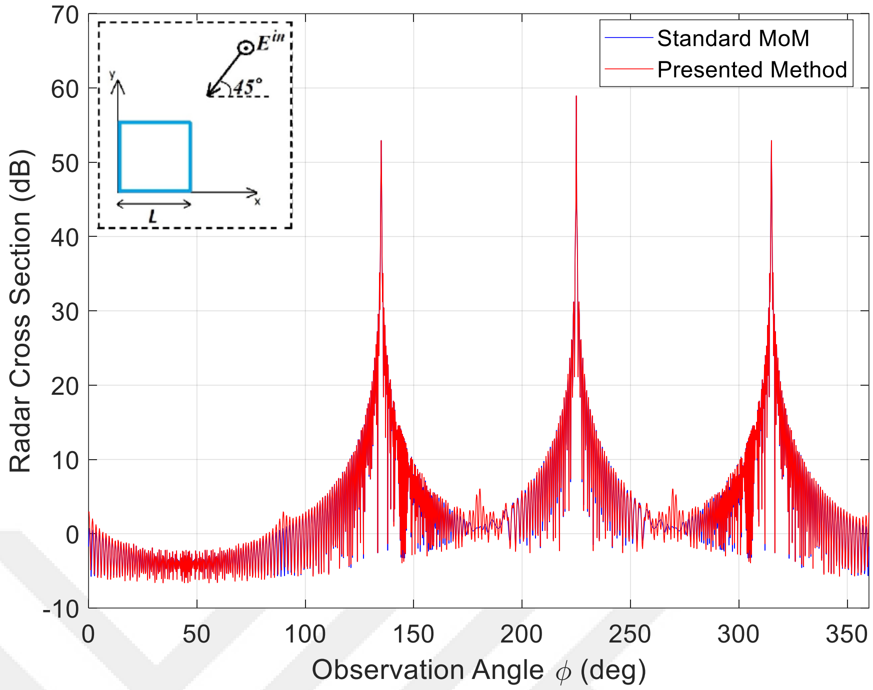

(a) E-pol case, L = 250λ, α = 0.5λ, 4W = 0.1λ, and RE = 0.03%

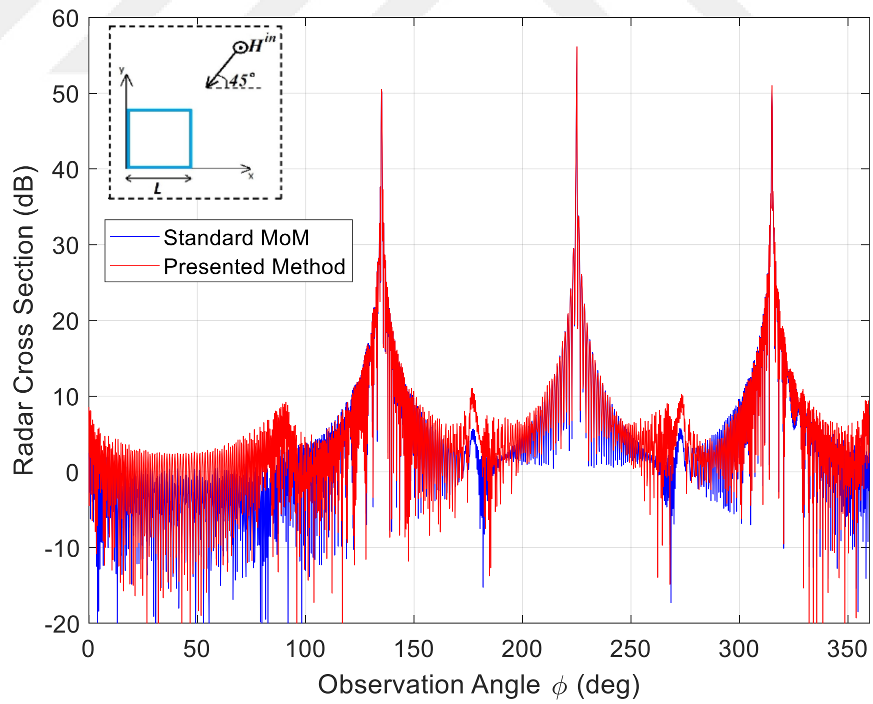

(b) H-pol case, L = 200λ, α = 0.5λ, 4W = 0.2λ, and RE = 0.14%

Figure 5.11 RCS pattern comparison between the standard MoM and the proposed method for $\phi^{in} = 45^o$

Table 5.3 CPU time and memory storage comparison for PEC square cylinder geometry (E-Pol)

Cross-sectional area	Length of the facet (λ)	Incident angle (degree)	4W (λ)	α (λ)	Solution Time (seconds)		Memory Storage			Relative error (%)
					MoM	*Presented method*	*Number of the unknown, N*	*MoM*	*Presented method*	
Square	L=25	45	0.1	2	1572	235	1000	1000·N	164·N	0.13
Square	L=25	90	0.1	2.5	1526	246	1000	1000·N	204·N	2.21
Square	L=250	45	0.1	0.5	153671	1040	10000	10000·N	44·N	0.03

Table 5.4 CPU time and memory storage comparison for PEC square cylinder geometry (H-Pol)

Cross-sectional area	Length of the facet (λ)	Incident angle (degree)	4W (λ)	α (λ)	Solution Time (seconds)		Memory Storage			Relative error (%)
					MoM	*Presented method*	*Number of the unknown, N*	*MoM*	*Presented method*	
Square	L=25	45	0.2	2	8397	1137	1000	1000·N	168·N	0.68
Square	L=25	90	0.2	2.5	8411	1511	1000	1000·N	208·N	0.44
Square	L=200	45	0.2	0.5	473588	2187	8000	8000·N	48·N	0.14

The number of memory storage is exhibited in Table 5.3 and Table 5.4 for the MoM and the proposed method in both polarizations. It can be seen that memory storage is reduced considerably comparing to the first hybrid method. In parallel with this reduction, the overall CPU time to obtain the current density function also decreased for the second hybrid technique. Extraordinary time gains have been realized in the largest sizes for both polarizations, such as over 200 times less than the MoM solution. Moreover, REs values are less than 0.1%, although the geometrical size of the problem is enlarged to 1000λ. Also, the smaller condition number compared to the first method is obtained, and it provides to analyze larger geometries as more steady with excellent solution time. By using this technique, the condition number has been reduced from 10^6 to 10^4.

5.3.3.2 Triangle Cross-Sectional PEC Cylinder Geometry

In Figure 5.12, the triangle shape of a PEC cylinder cross-section is analyzed with a side width of 25λ. The incidence angle is assumed as $\phi^{in} = 90^{o}$ for both polarisations.

Considerably suitable results have also been obtained with very small REs, which are less than 0.1%.

In Figure 5.13, RCS pattern comparisons are shown for L = 25λ and ϕ^{in} = 45^o for both polarizations. Like in the square cross-sectional PEC cylinder geometry, it is seen that the second hybrid technique is undeveloped compared to the first hybrid technique when the incidence angle is inclined case. RE values are at higher levels, and minor lobes are less accurate comparing to the first hybrid technique.

The method has also been tested for the problem with very large facets of the triangle. The incidence angle is ϕ^{in} = 90^o for both polarizations. In Figure 5.14, RCS plots have been demonstrated for E-pol case with a facet of triangle L = 250λ and H-pol case with a facet of triangle L = 200λ. Noteworthy, REs have been obtained in this structure with 1.59% and 0.08% for E-pol and H-pol, respectively.

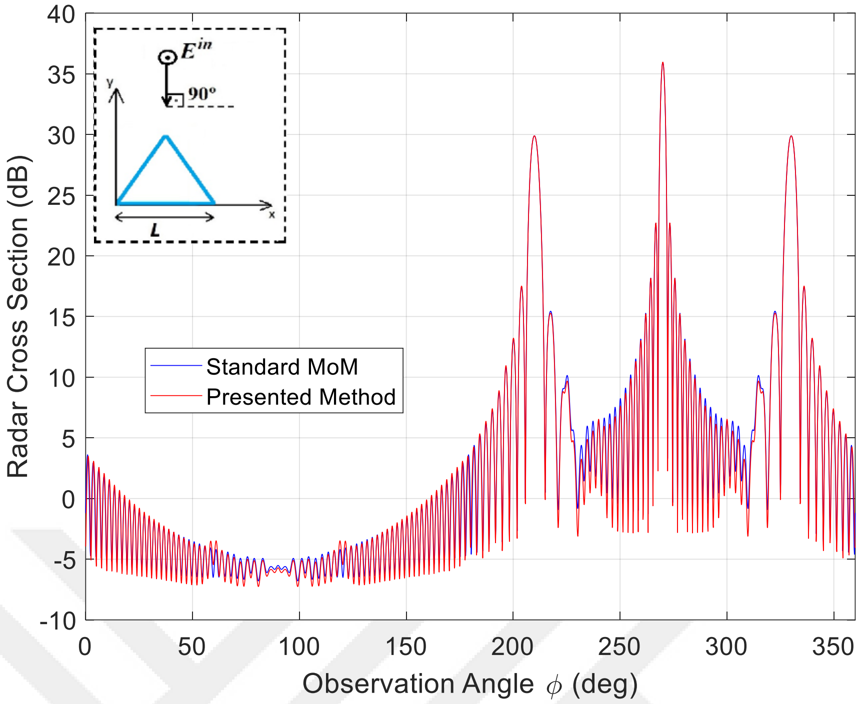

(a) E-pol case, α = 0.7λ, 4W = 0.1λ, and RE = 0.57%

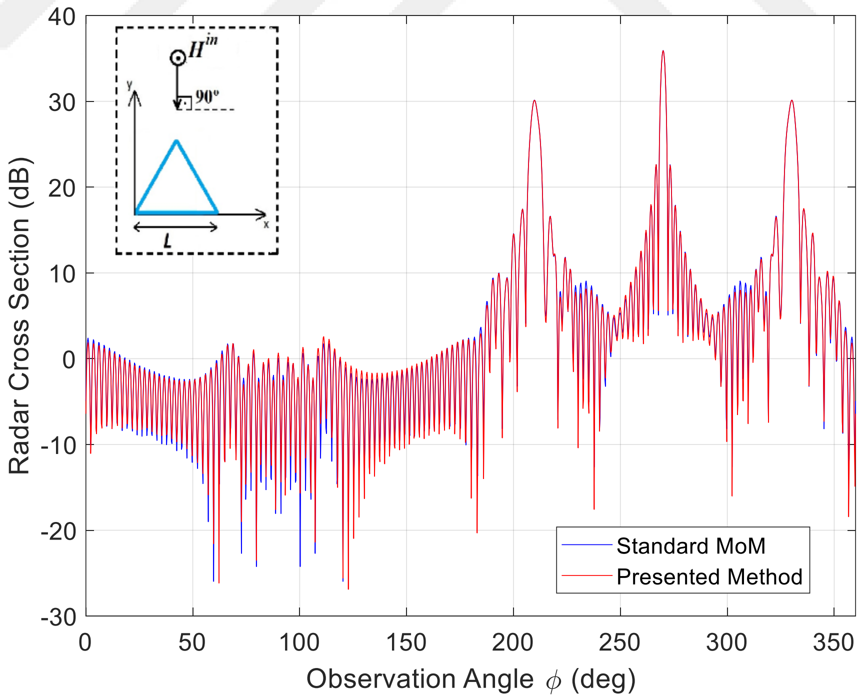

(b) H-pol case, α = 1.5λ, 4W = 0.2λ, and RE = 0.47%

Figure 5.12 RCS pattern comparison between the standard MoM and the proposed method for L = 25λ, $\phi^{in} = 90^o$

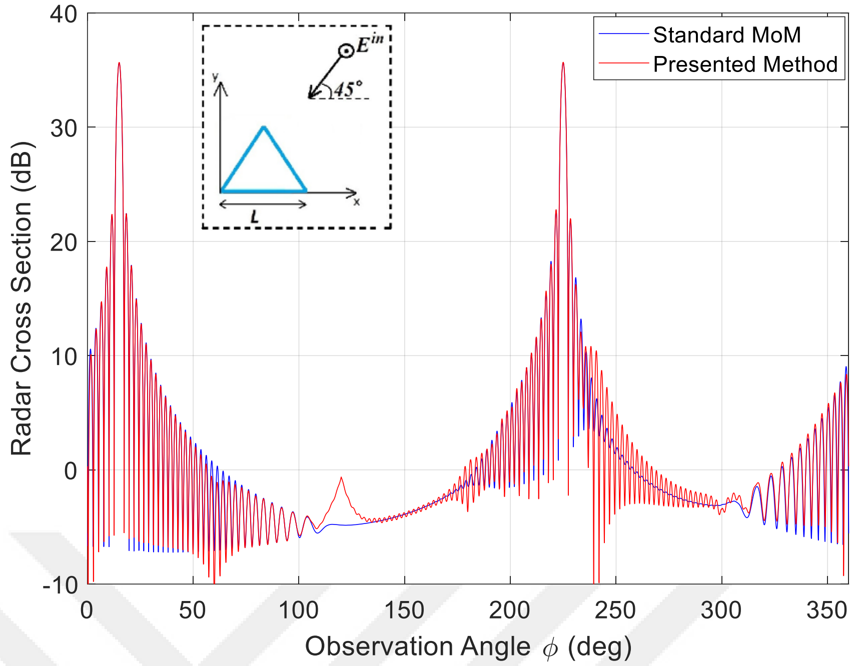

(a) E-pol case, α = 2.5λ, 4W = 0.1λ, and RE = 0.94%

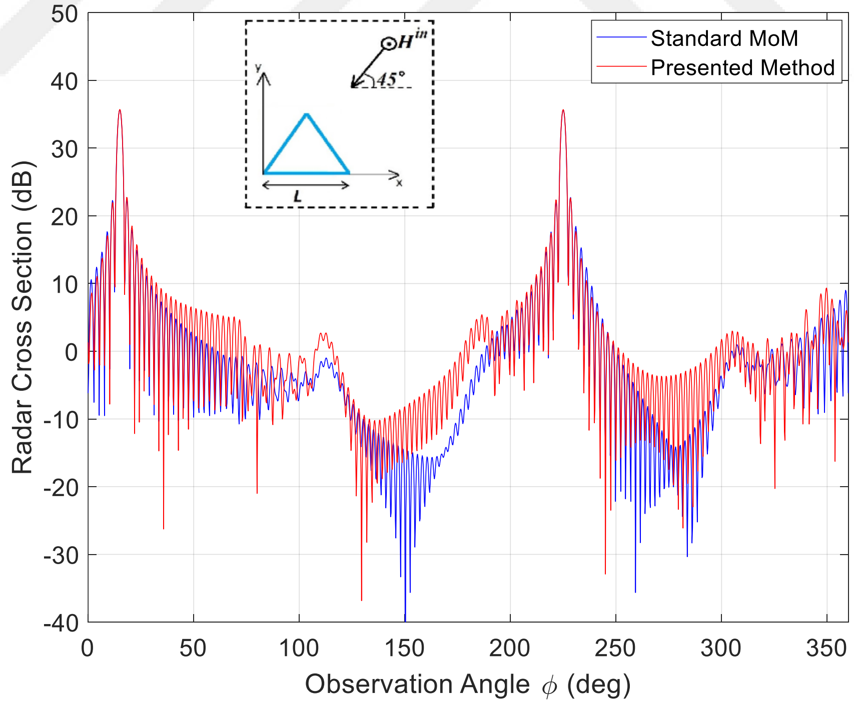

(b) H-pol case, α = 2.5λ, 4W = 0.2λ, and RE = 1.81%

Figure 5.13 RCS pattern comparison between the standard MoM and the proposed method for L = 25λ, $\phi^{in} = 45^o$

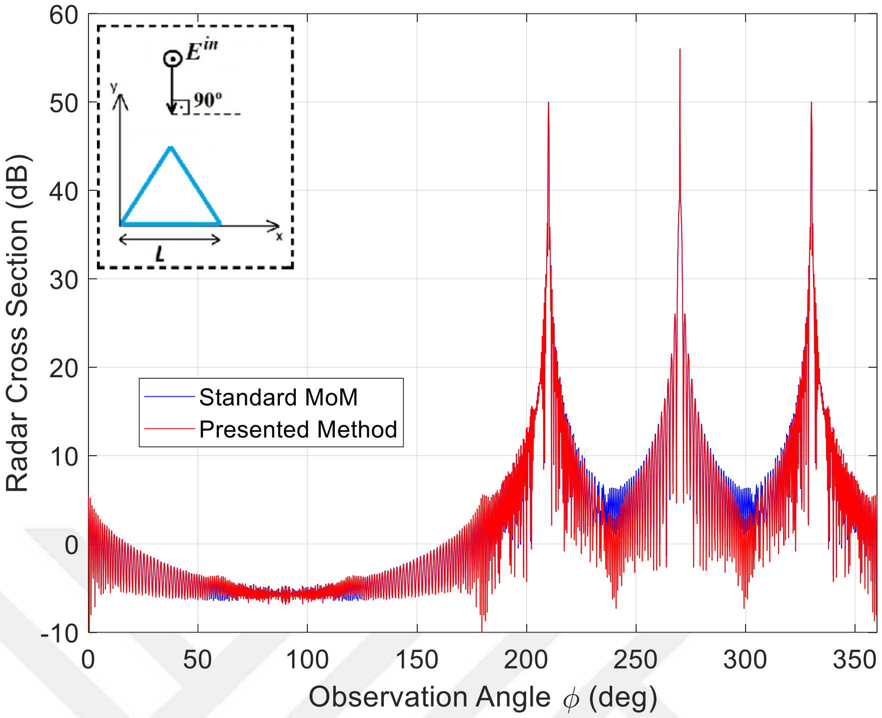

(a) E-pol case, $L = 250\lambda$, $\alpha = 0.5\lambda$, $4W = 0.1\lambda$, and RE = 1.59%

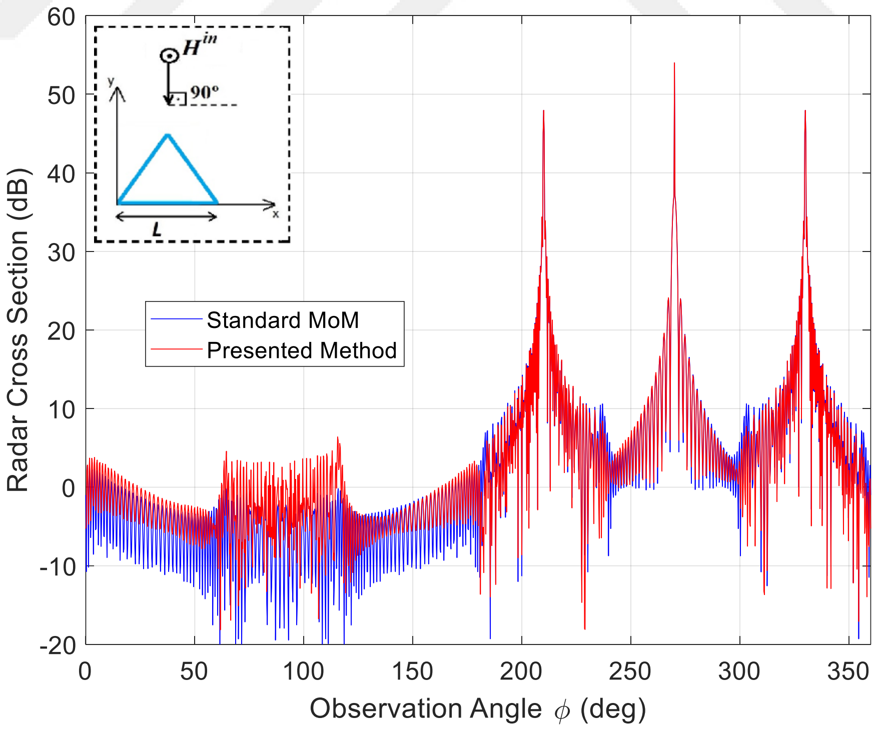

(b) H-pol case, $L = 200\lambda$, $\alpha = 1\lambda$, $4W = 0.2\lambda$, and RE = 0.08%

Figure 5.14 RCS pattern comparison between the standard MoM and the proposed method for $\phi^{in} = 90^{o}$

The overall CPU time and memory storage comparisons are listed in Table 5.5 and Table 5.6 for the MoM and the proposed method in this geometry. Respectable time gains have been achieved in the largest sizes for both polarizations. Comparing to the MoM solution, the time gains are over 250 times in E-pol and 200 times in H-pol.

Table 5.5 CPU time and memory storage comparison for PEC triangle cylinder geometry (E-Pol)

Cross-sectional area	**Length of the facet (λ)**	**Incident angle (degree)**	**4W (λ)**	**α (λ)**	**Solution Time (seconds)**		**Memory Storage**			**Relative error (%)**
					MoM	***Presented method***	***Number of the unknown, N***	***MoM***	***Presented method***	
Triangle	L=25	90	0.1	0.7	1572	58	1000	1000·N	46·N	0.57
Triangle	L=25	45	0.1	2.5	1526	227	1000	1000·N	154·N	0.94
Triangle	L=250	90	0.1	0.5	153671	571	10000	10000·N	34·N	1.59

Table 5.6 CPU time and memory storage comparison for PEC triangle cylinder geometry (H-Pol)

Cross-sectional area	**Length of the facet (λ)**	**Incident angle (degree)**	**4W (λ)**	**α (λ)**	**Solution Time (seconds)**		**Memory Storage**			**Relative error (%)**
					MoM	***Presented method***	***Number of the unknown, N***	***MoM***	***Presented method***	
Triangle	L=25	90	0.2	1.5	8397	504	1000	1000·N	98·N	0.47
Triangle	L=25	45	0.2	2.5	8411	856	1000	1000·N	158·N	1.81
Triangle	L=200	90	0.2	1	473588	2277	8000	8000·N	68·N	0.08

CHAPTER SIX
CONCLUSION AND FUTURE PLANS

In this thesis, it has been presented an alternative approach to the numerical solution of 2D EM scattering problems by two hybrid numerical techniques based on beam pattern functions combining with the MoM. In the first proposed technique, which is named as *the MoM procedure with CSP type Green's function*, the real source position vector has been replaced using a complex quantity to generate a complex line source type Green's function. Then the proposed method has been applied to 2D plane wave scattering problems for PEC strip geometry and the more complex structures, PEC cylindrical objects with closed polygonal cross-sections and PEC corner reflector geometry. The main impedance matrix is strongly localized for the problems, and the full-dense matrix is reduced to a sparse form. Since the far zone interactions are limited only to radiation from the small regions near the edges of the structure, the memory storage is reduced drastically. Accordingly, the non-zero elements of the main impedance matrix have been decreased, providing a solution for larger geometries.

The conditions of EM uniqueness theorem have been considered to verify the method. Comparison of the far-field RCS patterns (also near field for the strip geometry) between the proposed method and the standard MoM has been introduced. Numerical results are presented in both polarisations for a PEC strip and 2D PEC objects with closed polygonal cross-sections such as square and triangle shape. When compared the proposed method to the MoM, significant time gain has been realized, such as over 100 times less compared to the MoM solution for the strip size 3000λ. While maximum strip size is limited to 3000λ to solve the problem by the standard MoM, the proposed method can solve in about 100 seconds for the strip size 50000λ. Also, the proposed method has been checked with the UTD solution for the strip size 5000λ. Good results in the RCS pattern have been presented with RE 0.03% for E-pol and RE 0.97% for H-pol.

For PEC objects with closed polygonal cross-sections, the RCS patterns have also been demonstrated, and the RE plots have been discussed by comparing them with the standard MoM solutions. Comparisons have been made for square or triangle facet, such as 250λ in E-pol and 200λ in H-pol, and RE values are less than 0.1%. Remarkable time gains have been succeeded for both polarizations, such as over 30 times less compared to the MoM solution. The proposed method is in agreement with the MoM, with very small REs of less than one percent in both normal and inclined incidence.

Also, 2D PEC open body structure like a corner reflector geometry has been investigated for different reflector's angles. It has been observed that the outcomes go to inaccuracy when the angle is smaller than 90^o. This conclusion has been discussed regarding the beam nature and explained in the interactions of beams with each other. Therefore, RCS results have been plotted for large structures with 120^o reflector's angles and different incident angles in both polarisations.

As the size of the geometry becomes larger, the computational time increases severely for the standard MoM, but it is feasible with the proposed method. It needs to be pointed out the condition number of the main matrix, and it is around 10^6 for all geometries. Nevertheless, results have been remained steady when the geometrical size of scatterers is extended to significant cases such as 1000λ. Although the condition number is relatively large, accurate results have been acquired by using iterative preconditional sparse solvers to perform optimal options in MATLAB. Consequently, we succeeded in achieving a considerable time gain in the solution for very large flat strip geometry and a remarkable gain for corner reflector and polygon cylinder geometries. Furthermore, the presented method is an efficient solution, especially in the case of large configurations. Owing to the IML, memory storage is linearly proportional to the number of unknown N, for 2D PEC polygon cross-section cylinder geometries and PEC corner reflector geometry. In the largest configurations, it is about O(150xN) in corner reflector and O(300xN) in cylinder geometries for both polarizations that enable us to study for larger scatterers, which is not possible to solve by using the MoM.

The second proposed technique, *the MoM Procedure with Modified Green's Function by using GPOF Method*, it has been introduced a new Green's function by using the GPOF method for 2D EM scattering. It has been proved that the localization is not related only to the variation in the Hankel function, and demonstrated that it could be different localization types as a beam-pattern function. As a difference from the first method, this new Green's function has a beam aperture that allows more localization on the surface. Its beam width is a narrower form, so it interacts only for a few basis function levels. In the same manner, the main matrix is localized even more, and this localization of the modified Green's function gives rise to the higher level sparsity in the main matrix compared to the first method. It has again been considered the EM scattering conditions of the uniqueness theorem if the proposed method is valid.

Then, the proposed method has been applied to 2D plane wave scattering problems for PEC strip geometry and PEC polygon cross-section cylinder geometries. The far-field RCS patterns have been compared between standard MoM and the proposed method for the same structures and incident angles in the first hybrid technique. It has been observed that they were in harmony with each other with very small REs, and the majority of them were less than one percent. However, REs are a little higher in grazing incidence angles relating to structure shape when it is compared to the first method. Due to the more localization procedure, the proposed hybrid technique provides an essential advantage in computer storage and calculation time, even when compared to the first hybrid technique. As the size of the geometry becomes more extensive, the computational time remains excellent with the proposed method. Extraordinary time gains have been realized in the largest sizes of 2D PEC polygon cross-section cylinder geometries for both polarizations, such as over 200 times less compared to the MoM solution.

Moreover, the condition number of the main matrix is reasonable levels, such as 10^4 for all geometries. So the proposed method has the potential for implementation to be applied to more complex large structures. Memory storage is linearly proportional to the number of unknown N, for 2D PEC polygon cross-section cylinder geometries.

In the largest contours, it is about O(50xN) in cylinder geometries for both polarizations that enable us to analyze for very large scatterers with extremely short solution times. In the RCS results, it is evident that the harmony compared to the MoM solution for minor lobs is behind the first hybrid technique. Minor lobes in RCS results are more accurate in the first hybrid technique. However, the second method has an advantage against the first method in terms of the time gain and memory storage.

Consequently, a substantial time gain and memory storage have been performed in the solution of the two hybrid methods for 2D EM scattering problems. These two hybrid techniques also offer to analyze larger geometries and to be applied to 3D geometries. Since the implementation is applied to the Hankel function apart from the geometry, the CSP type Green's function and the modified Green's function have the potential to realize 3D EM scattering problems. Since EM modeling is the research of the interaction of EM fields with physical objects and the environment, these methods can be employed for analyzing scattering objects to find out EM simulations. In the further step, their extension models for 3D objects can be used to detect EM compatibility.

Although these methods are utilized when the scatterer size is very large comparing to the wavelength of the incident wave, they are not well-suited for sub-wavelength structures due to the edge dominant nature of their scattering.

For the future plans, 2D scattering for open structures can be studied further with the field interactions by using some iterative techniques. Considering the scattering fields from the structure as a source field for the next iteration, by applying these hybrid techniques, more accurate results can be obtained after a few iterations.

By using these two new hybrid techniques, the inner frequency trouble encountered in the problems of closed body structures can be handled easily. Besides that, these two hybrid methods can be combined with other ones and improved to a more convenient form for analyzing of various structures.

REFERENCES

Ando, M., Kohama, T., Shijo, T., Hirano, T., & Hirokawa, J. (2011). High frequency locality embodied in terms of Fresnel zone number for matrix size reduction in method of moments. *2011 International Conference on Electromagnetics in Advanced Applications*, 1432-1435, Italy: IEEE.

Belenguer, A., Esteban, H., Boria, V.E., & Bachiller, C. (2005). Computation of the scattering of electrically large 2D objects using FMM with TE^z incidence. *IEEE Antennas and Propagation Society International Symposium*, 455-458, Washington DC, USA: IEEE.

Boag, A., Michielssen, E., & Mittra, R. (1994). Hybrid multipole-beam approach to electromagnetic scattering problems. *Applied Computational Electromagnetics Society Journal*, *9*, 7-17.

Boag, A., & Mittra, R. (1994a). Complex multipole beam approach to electromagnetic scattering problems. *IEEE Transactions on Antennas and Propagation*, *42*, 366-372.

Boag, A., & Mittra, R. (1994b). Complex multipole-beam approach to three-dimensional electromagnetic scattering problems. *Optical Society of America*, *11*, 1505-1512.

Boriskin, A.V., & Nosich, A.I. (2002). Whispering-gallery and Luneburg lens effects in a beam-fed circularly-layered dielectric cylinder. *IEEE Transactions on Antennas and Propagation*, *50*, 1245-1249.

Boriskin, A.V., Sauleau, R., & Nosich, A.I. (2009). Performance of hemielliptic dielectric lens antennas with optimal edge illumination. *IEEE Transactions on Antennas and Propagation*, *57* (7), 2193-2198.

Brennan, C., Cullen, P., & Condon M. (2004). A novel iterative solution of the three dimensional electric field integral equation. *IEEE Transactions on Antennas and Propagation, 52,* 2781-2784.

Bulygin, V.S., Gandel, Y.V., Benson, T.M., & Nosich, A.I. (2013). Full-wave analysis and optimization of a TARA-like shield-assisted paraboloidal reflector antenna using a Nystrom-type method. *IEEE Transactions on Antennas and Propagation, 61,* 4981-4989.

Canning, F. (1990). The impedance matrix localization (IML) method for moment method calculations. *IEEE Antennas and Propagation Magazine, 32* (5), 18-30.

Chabory, A., & Bolioli, S. (2006). Novel Gabor-based Gaussian beam expansion for curved aperture radiation in dimension two. *Progress In Electromagnetics Research, 58,* 171–185.

Chow, Y. L., Yang, J. J., Fang, D. G., & Howard, G. E. (1991). A closed-form spatial Green's function for the thick microstrip substrate. *IEEE Transactions On Microwave Theory And Techniques, 39,* 588 - 592.

Coifman, R., Rokhlin, V., & Wandzura, S. (1993). The fast multipole method for the wave equation: A pedestrian prescription. *IEEE Antennas and Propagation Magazine, 35* (3), 7-12.

Dural, G., & Aksun, M. I. (1995). Closed-form Green' s functions for general sources and stratified media. *IEEE Transactions On Microwave Theory And Techniques, 43,* 1545-1552.

Erez, E., & Leviatan, Y. (1994). Electromagnetic scattering analysis using a model of dipoles located in complex space. *IEEE Transactions on Antennas and Propagation, 42,* 1620-1624.

Felsen, L. B. (1976). Complex source point solution of the field equations and their relation to the propagation and scattering of Gaussian beams. *Symposia Mathematica*, *18*, 39-56.

Gürel, L., & Ergül, Ö. (2005). Singularity of the magnetic-field integral equation and its extraction. *IEEE Antennas and Wireless Propagation Letters*, *4*, 229-232.

Han, S.K., Michielssen, E., Shanker, B., & Chew, W.C. (1998). Impedance matrix localization based fast multipole acceleration. *Radio Science*, *33*, 1475-1488.

Harrington, R.F. (1968). *Field computation by moment methods*, New York: Macmillan Co.

Hayashi Y. (1996). Electromagnetic theory based on integral representation of fields and analysis of scattering by open boundary. *Progress In Electromagnetics Research*, *13*, 1-86.

Hodges, R. E., & Rahmat-Samii, Y. (1997). The evaluation of MFIE integrals with the use of vector triangle basis functions. *Microwave and Optical Technology Letters, 14* (1), 9-14.

Hua, Y., & Sarkar, T. K. (1989). The generalized pencil-of-function method for extracting poles from transient responses. *IEEE Transactions on Antennas and Propagation*, *37*, 229-234.

Ilic, M. M., & Notaros, B. M. (2009). Higher order FEM-MOM domain decomposition for 3-D electromagnetic analysis. *IEEE Antennas and Wireless Propagation Letters*, *8,* 970-973.

Jakobus, U., & Landstorfer, F. M. (1995). Improved PO-MM hybrid formulation for scattering from three-dimensional perfectly conducting bodies of arbitrary shape. *IEEE Transactions on Antennas and Propagation*, *43* (2), 162-169.

Jakobus, U., & Meyer, F.J.C. (1996). A hybrid physical optics/method of moments numerical technıque: Theory, investigation and application. *Proceedings of IEEE* (*AFRICON 96)*, 282-287, Stellenbosch: IEEE.

Kutluay, D., & Oğuzer, T. (2017). The fast computation of the electromagnetic scattering by using the complex line source type Green's function in the method of moments. *IEEE Proceedings, Microwaves, Radar and Remote Sensing Symposium*, 224-228, Kyiv: IEEE.

Kutluay, D., & Oğuzer, T. (2019). Fast modeling of electromagnetic scattering from 2D electrically large PEC objects using the complex line source type Green's function. *International Journal of Microwave and Wireless Technologies*, *11*, 276-286.

Lee, J.H., & Kim, H.T. (1999). Selection of sampling interval for the GPOF method. *Journal of Electromagnetic Waves and Applications*, *13* (9), 1269-1281.

Liu, Z.L., & Wang, C.F. (2012). Efficient iterative method of moments physical optics hybrid technique for electrically large objects. *IEEE Transactions on Antennas and Propagation*, *60* (7), 3520-3525.

Lucente, E., Monorchio, A., & Mittra, R. (2008). An iteration-free MoM approach based on excitation independent characteristic basis functions for solving large multiscale electromagnetic scattering problems. *IEEE Transactions on Antennas and Propagation*, *56*, 999-1007.

Melamed, T. (2009). Exact Gaussian beam expansion of time harmonic electromagnetic waves. *Journal of Electromagnetic Waves and Applications*, *23*, 975–986.

Menzel, W., Pilz, D., & Al-Tikriti, M. (2002). Millimeter-wave folded reflector antennas with high gain, low loss, and low profile. *IEEE Antennas and Propagation Magazine*, *44* (3), 24-29.

Mohammadi-Ghazi, R., & Büyüköztürk, O. (2016). Sparse generalized pencil of function and its application to system identification and structural health monitoring. In *Health Monitoring of Structural and Biological Systems, 9805,* 98050B.

Oğuzer, T., Altintas, A., & Nosich, A. I. (1995). Accurate simulation of reflector antennas by the complex source-dual series approach. *IEEE Transactions on Antennas and Propagation*, *43*, 793-801.

Oğuzer, T., & Kutluay, D. (2019). A novel impedance matrix localization for the fast modeling of 2D electromagnetic scattering using the localized Green's function. *International Symposium on Electromagnetic Fields in Mechatronics, Electrical and Electronic Engineering*, Nancy: IEEE.

Rahmat-Samii, Y., & Haupt, R. (2015). Reflector antenna developments: A perspective on the past, present and future. *IEEE Antennas and Propagation Magazine*, *57*, 85-95.

Rao, S. M., Wilton, D. R., & Glisson, A. W. (1982). Electromagnetic scattering by surfaces of arbitrary shape. *IEEE Transactions on Antennas and Propagation*, *30*, 409-418.

Rudge, A.W., & Adatia, N.A. (1978). Offset-parabolic-reflector antennas: A review. *Proceedings of the IEEE*, *66*, 1592-1618.

Rui, P. L., Chen, R. S., Liu, Z. W., & Gan Y. N. (2008). Schwarz-Krylov Subspace Method for MLFMM Analysis of Electromagnetic Wave Scattering Problems. *Progress in Electromagnetics Research*, *82*, 51-63.

Shijo, T., Hirano, T., & Ando, M. (2005). Large-size local-domain basis functions with phase detour and Fresnel zone threshold for sparse reaction matrix in the method of moments. *IEICE Transactions on Electronics, 88* (12), 2208-2215.

Suedan, G. A., & Jull, E.V. (1991). Beam diffraction by planar and parabolic reflectors. *IEEE Transactions on Antennas and Propagation, 39*, 521-527.

Tasic, M. S., & Kolundzija, B. M. (2011). Efficient analysis of large scatterers by physical optics driven method of moments. *IEEE Transactions on Antennas and Propagation*, *59*, 2905–2915.

Tasic, M. S., & Kolundzija, B. M. (2018). Method of moment weighted domain decomposition method for scattering from large platforms. *IEEE Transactions on Antennas and Propagation*, *66*, 3577-3589.

Tap, K. (2007). *Complex source point beam expansions for some electromagnetic radiation and scattering problems.* Ph.D. Thesis, Ohio State University, USA.

Tap, K., Pathak, P.H., & Burkholder, R.J. (2011). Exact complex source point beam expansions for electromagnetic fields. *IEEE Transactions on Antennas and Propagation*, *59*, 3379-3390.

Tap, K., Pathak, P.H., & Burkholder, R.J. (2014). Complex source beam-moment method procedure for accelerating numerical ıntegral equation solutions of radiation and scattering problems. *IEEE Transactions on Antennas and Propagation*, *62*, 2052-2062.

Thiele, G. A., & Newhouse, T. H. (1975). A hybrid technique for combining moment methods with the geometrical theory of diffraction. *IEEE Transactions on Antennas and Propagation, 23*, 62-69.

Thiele, G. A., & Mittra, R. (1992). Overview of selected hybrid methods in radiating system analysis. *Proceedings of the IEEE*, *80*, 66-78.

Tsitsas, N.L., Valagiannopoulos, C.A., & Nosich, A.I. (2014). Scattering and absorption of a complex source point beam by a grounded lossy dielectric slab with a superstrate. *Journal of Optics*, *16*, 1-10.

Zhu, X., Geng, Y., & Wu, X. (2000). Application of MOM-CGM-FFT to 3D dielectric scatterers. *IEEE International Symposium on Antennas, Propagation, and EM Theory*, 293-296, Beijing: IEEE.